



3 1293 01055 9718

This is to certify that the
dissertation entitled
**THE EFFECT OF SPACE CHARGE FORCE ON BEAMS
EXTRACTED FROM ECR ION SOURCES**

presented by

Zu Qi Xie

has been accepted towards fulfillment
of the requirements for

Ph. D. degree in Physics


Major professor

Date Aug 31, 1989

LIBRARY
Michigan State
University

PLACE IN RETURN BOX to remove this checkout from your record.
TO AVOID FINES return on or before date due.

DATE DUE	DATE DUE	DATE DUE
_____	_____	_____
_____	_____	_____
_____	_____	_____
_____	_____	_____
_____	_____	_____
_____	_____	_____
_____	_____	_____

**THE EFFECT OF SPACE CHARGE FORCE ON BEAMS
EXTRACTED FROM ECR ION SOURCES**

**by
Zu Qi Xie**

A DISSERTATION

**Submitted to
Michigan State University
in partial fulfillment of the requirements
for the degree of**

DOCTOR OF PHILOSOPHY

Department of Physics and Astronomy

1989

6050579

ABSTRACT

THE EFFECT OF SPACE CHARGE FORCE ON BEAMS EXTRACTED FROM ECR ION SOURCES

by

Zu Qi Xie

A new 3 dimensional ray tracing code BEAM_3D, with a simple model to calculate the space charge force of multiple ion species, is under development and serves as a theoretical tool to study the ECRIS beam formation. Excellent agreement between the BEAM_3D calculations and beam profile and emittance measurements of the total extracted helium 1+ beam from the RTECR ion source was obtained when a low degree of beam neutralization was assumed in the calculations. The experimental evidence indicates that the positive space charge effects dominate the early RTECR ion source beam formation and beamline optics matching process. A review of important beam characteristics is made, including a conceptual model for the space charge beam blow up. Better beam transport through the RTECR beamline analysis magnet has resulted after an extraction geometry modification in which the space charge force was more correctly matched. This work involved the development of an online beam characteristic measuring apparatus which will also be described.

ACKNOWLEDGMENTS

I wish to thank the staff and faculty of the National Superconducting Cyclotron Laboratory for their support of my education and the completion of this dissertation. First and foremost, I owe my deepest gratitude to my thesis advisor Dr. Timothy Antaya for his guidance, supervision and friendship during the four years that I have worked with him, without his help, this thesis would be all blank pages. Second, I would like to specially thank Professor Jerry Nolen, for his guidance in my early graduate career and the freedom he gave me to work on ECR Ion Source to pursue my academic interests. In addition, I wish to thank Dr. Thomas Kuo for his encouragement and the friendship we shared over the past years, and Dr. G. Mank for performing the GIOS calculations used in Chapter 5 of this thesis.

Finally I am greatly indebted to my wife Li Su, for her love, patience and encouragement to make it through.

I am also very grateful to Michigan State University and the National Science Foundation for the financial support during my graduate study.

TABLE OF CONTENTS

LIST OF TABLES.....	v
LIST OF FIGURES.....	vi
Chapter 1 - Introduction.....	1
1.1 Motivation.....	1
1.2 RTECR Source and Its Beam Analysis System.....	4
1.3 He Beam Technique.....	10
Chapter 2 - The BEAM_3D Code.....	13
2.1 Motivation.....	13
2.2 General Organization.....	14
2.3 Special Features.....	22
Chapter 3 - Emittance Measuring Apparatus.....	28
3.1 Theoretical Review of Emittance Measurements.....	28
3.2 Online Slit-Wire Scanner.....	40
3.3 Kapton Camera.....	42
Chapter 4 - Extraction Geometry Study.....	46
4.1 Motivation.....	46
4.2 Theoretical Review.....	50
4.2.1 Equations of Motion.....	50
4.2.2 Effects of Ion Temperature, Magnetic Field and Q/M Ratio on Beam Emittance.....	58
4.2.3 Extraction Electrode Design.....	64
4.3 BEAM_3D Predictions on the Extraction Electrode Design..	69
4.4 Results.....	73
Chapter 5 - Space Charge Force and Pre-analysis Beam Transport...	77
5.1 Space Charge Force.....	77
5.2 Beam Transit of the Solenoid Magnet.....	85

5.3 Transit of the Analysis Magnet.....	94
5.4 Matching the 90° Analysis Dipole under the Effect of Space Charge.....	98
Chapter 6 - Summary and Conclusions.....	102
6.1 Extrapolation to Multiply-Charged Ion Beams.....	102
6.2 Summary and Conclusions.....	103
Appendix - Introduction to ECRIS.....	107
A.1 'Unit' ECR Cell.....	107
A.2 ECR Operating Characteristics.....	114
LIST OF REFERENCES.....	125

LIST OF TABLES

TABLE	PAGE
1.1 RTECR source DC performance for gaseous feed materials....	6
1.2 RTECR source DC performance for solid feed materials.....	7
5.1 Beam envelope at the 90° dipole entrance.....	100

LIST OF FIGURES

FIGURE	PAGE
1.1 A schematic diagram showing the main features of the RTECR ion source.....	5
1.2 A schematic view of the RTECR analysis system and the beam analysis systems built for the studies presented in this thesis.....	9
1.3 A helium spectrum is shown here. 300 eμA helium 1+ was produced by the RTECR source at Vex = 10 kV, Vp = 0 and 80 watts of RF power, while less than 5% helium 2+ was produced.....	12
2.1 Flow diagram of the BEAM_3D code.....	15
2.2 This figure shows the grid points involved in the interpolation of field components of an intermediate point P(r,z).....	18
2.3 The geometry used in the calculation of the space charge force.....	20
2.4 A schematic view of the extraction geometry and the initial beam transport line of the RTECR source for BEAM_3D calculation.....	23
2.5 The axial and transverse ion orbits of He ¹⁺ and He ²⁺ calculated by the BEAM_3D code.....	24
2.6 The initial and final ion position distributions.....	25
2.7 The initial and final charge state distributions (CSD).....	26
2.8 The emittance fittings. A. At the beam defining slit. B. At the entrance of the 90° dipole.....	27
3.1 Schematic cross section of a beam.....	29
3.2 The phase area of a beam with rotational symmetry is described by an ellipse.....	31
3.3 The particles which lie in the shaded area of the shown ellipse (z = 0) will evolve to either of the cases in B (z = 1) or C (z = L) after a drift distance.....	33

3.4	A comparison, for the case Figure 3.3B with drift distance 100 mm, of the line current density and the calculated current profile if measured with a wire of 0.3 mm wide. The particles are in the area determine by $x_1 = 9$ mm and $x_2 = 11$ mm for an ellipse with a 45° orientation, $a = 5$ mm and $b = 20$ mrad, at $z = 0$	37
3.5	A comparison, for the case Figure 3.3C with a drift distance 500 mm, of the line current density and the calculated current profile if measured with a wire of 0.3 mm wide. The rest conditions are the same with the case in Figure 3.4.....	38
3.6	The assembly of the wire scanner.....	41
3.7	A 3 eμA Ar ¹⁰⁺ beam profile after the analysis magnet is shown. The large tail is believed due to the high divergence beam component. An ellipse fit at 90% intensity gives emittance $\epsilon = 245$ mm mrad.....	43
3.8	The assembly of the 'Kapton camera'.....	45
4.1	A. A schematic view of a three electrode extraction system. B. Accel-decel voltage distribution. C. Accel-only voltage distribution. D. Accel-accel voltage distribution.....	47
4.2	A schematic view of the two extraction electrode systems utilized in the RTECR. A. The puller has a face angle at 45°. B. The puller has a Pierce spherical face shape [Pi54].....	49
4.3	The extraction region of an ECRIS with an axial magnetic field. Ions are extracted from the source at radius r_1	53
4.4	Schematic view of a group of identical ions on a circle travelling along the optical axis.....	53
4.5	The correlation in phase space. Point i in the XX' plane corresponds with point i in the YY' plane.....	55
4.6	The effects of ion temperature on the ideal argon beam emittance as a function of charge-to-mass ratio. Ions are assumed extracted at 10 kV, extraction aperture $r_a = 4$ mm and with $B_z = 0.25$ T (approximately the same conditions as for the RTECR extraction).....	61

4.7	Argon beam emittances with the ion temperature taken as $T_1 = t_c \text{ eV} \times q$. Other conditions are the same as in Figure 4.7.....	62
4.8	Emittances of cold argon beams with different extraction voltages and various extraction magnetic fields. The extraction aperture is $r_a = 4 \text{ mm}$	63
4.9	Plot of the electrode shapes (heavy lines) and the equipotential lines external to a planar space-charge-limited electron beam as determined from Eq. (4.29) [Pi54].	66
4.10	Electrodes for obtaining axially symmetrical electron flow of uniform diameter [Pi54].....	68
4.11	A comparison the axial and electric field strengths of 45° (denoted by "M2a") and a Pierce spherical pullers. In both cases the extraction gap is 3.3 cm and the first electrodes are the same.....	70
4.12	BEAM_3D calculated beam profiles at a space charge limited current for the extraction system with a 45° angle on the puller electrode face and a Pierce spherical puller. A drum shape in the first gap, and a focus in the puller electrode are seen for the 45° puller of Figure 4.2A.....	71
4.13	A comparison of the effective emittance after extraction for the 45° and a Pierce spherical pullers in the RTECR, for a space charge limited He^{1+} beam of 1.3 emA at $D = 3.3 \text{ cm}$, with $V_{ex} = 10 \text{ kV}$. BEAM_3D predicts the effective emittance of the 45° puller is about three times that of the Pierce spherical puller.....	72
4.14	Using the He^{1+} technique, the total extracted current of the RTECR was measured directly at FC#1 as a function of extraction voltage, for 3 operating pressures. At low voltages, the extracted current is space charge limited, following the Child-Langmuir law (marked Theory). At higher voltages the extracted current is seen to saturate.....	74
4.15	A transmission study on the analysis magnet for different extraction gaps and helium $1+$ currents ≤ 0.5	

	emA. A beam extracted at the space charge limit gives the best transmission, with decreasing transmission as the beam intensity falls increasingly below the space charge limit.....	76
5.1	He ¹⁺ beam maximum divergence versus the beam edge radius, for different beam intensities, after a waist. The maximum divergence is a constant if the space charge is zero. But as can be seen, if the space charge force is taken into account, then the beam maximum divergence will increase rapidly with the level of the space charge force.....	81
5.2	A comparison of the beam edge radius with axial drift distance for various levels of the space charge. The starting conditions are the same as in Figure 5.1. For high uncompensated space charge, the beam envelope rapidly increases with axial drift.....	82
5.3	A schematic view of the evolution of the emittance envelope after a waist with and without space charge force. The emittance is the same for both cases, but with space charge the maximum divergence and beam size significantly increase.....	84
5.4	A comparison of the divergence versus beam intensity for space charge limited extraction using the BEAM_3D code. Even though a parallel beam profile at the first gap is ensured, the effect of space charge, which increases the divergence, is clearly seen.....	86
5.5	The effective emittance of He ¹⁺ after crossing the focussing solenoid for various beam intensities . In each case the extraction is space charge limited, the beam energy is of 10 keV, and the emittance after extraction is 69 mm mrad. The 1.0 emA case shows very large emittance growth due to its large beam profile in the solenoid, thus the aberrations have become very severe.....	89
5.6	A and B are Kapton foil burns at the divergence box with He ¹⁺ beams of 65 and 550 eμA respectively. The beam	

	passes through a defining slit plate 8 cm upstream of the foil, giving horizontal marks on the foil. BEAM_3D predicts for 65 eμA He ¹⁺ with a space charge limited extraction (vex = 10 kV, Vp = 8.5 kV), beam profile at the divergence box will be 1.6" and that is experimentally seen. A 550 eμA He ¹⁺ extracted at space charge limit fills the Kapton foil at the divergence box, also agreeing fairly well with a BEAM_3D calculated profile of 3".....	90
5.7	The measured emittance for the 65 eμA He ¹⁺ beam in Figure 5.6A is ε = 69 mm mrad, which agrees very well with the BEAM_3D calculation (see Figure 5.5), in which the ion thermal energy was taken to be zero.....	91
5.8	A 65 eμA He ¹⁺ beam extracted (Vex = 10 kV, Vp = 0) well below the space charge limited (Vex = 10 kV, Vp = 8.5 kV) current results in high divergence and large beam profile. For this case, BEAM_3D predicts a diameter of 5.5" at the divergence box.....	92
5.9	BEAM_3D predicts that a 200 eμA He ¹⁺ extracted at 7, 10, 15 and 20 kV with an extraction gap of 3.3 cm will have very high divergence and large beam profile at the divergence box, because the extraction is far below the space charge limit. Measurements, limited by the measuring apparatus to a maximum divergence 65 mrad, show that the actual divergence is higher, in fair agreement with the calculations.....	93
5.10	A triangular beam mark is seen on the face of the collimator of FC#2 assembly for the CPECR. The cause of this triangle shape is believed to be the space charge effect on the beam divergence before the magnet entrance, resulting in filling the magnet aperture and causing 2nd order aberrations.....	96
5.11	A GIOS beam transport calculation for the case in Figure 5.10. The transit of the analysis magnet with an unneutralized 1.0 emA helium 1+ beam of starting emittance 200 mm mrad will result in a triangular shaped	

	beam after analysis.....	97
5.12	A schematic illustration of better matching of the 90° dipole for beams with space charge compared to the case of no space charge.....	99
5.13	A 330 eμA He ¹⁺ is extracted with space charge limit and transported through the 90° dipole, this beam has a waist at the dipole object when the focussing solenoid is excited with 81 A. However the optimized transmission occurs at I(solenoid) = 78 A, for which the beam waist is about 10 cm closer to the dipole.....	101
6.1	BEAM_3D code predicts that after crossing the focussing solenoid the effective emittance of Ar ⁸⁺ (S shaped, due to the solenoid spherical aberrations) is doubled compared to its effective emittance before the solenoid. The CSD and focussing solenoid excitation are based on actual operating values.....	104
A.1	A 'Unit' ECR Cell consists of a vacuum vessel, microwave generator, a minimum-B field and an extraction system.....	108
A.2	A typical axial magnetic field profile produced by a set of solenoid coils for a single stage ECRIS.....	109
A.3	This figure shows the strength of a hexapole as a function of radius along one of the poles and in a gap.....	111
A.4	A "minimum-B field" topology as a result of the superposition of a hexapole and a set of solenoid fields...	112
A.5	Single ionization potentials of some atoms and ions.....	115
A.6	Performance comparison between 2-stage and second stage only RTECR operation for the production of nitrogen ions. Helium is used as a support gas. Each next higher charge state shows a large percentage increase in current with the first stage on.....	116
A.7	Ionization rate coefficients S for single ionization of argon atoms and ions from the ground state by electron-impact in plasma (Maxwellian distribution, no collision limit).....	119
A.8	A high temperature oven for producing metal vapor is equipped with the CPECR Ion Source at NSCL/MSU.....	122

A.9	The direct dependence of gas mixing effects on mass is seen in the mixing of lighter gases with argon.....	123
-----	---	-----

Chapter 1

Introduction

1.1 Motivation

The ECRIS (Electron Cyclotron Resonance Ion Source, an introduction to the ECRIS is presented in the Appendix), is now the most frequently used new ion source for producing high charge state positive ions for accelerators and for atomic physics research. ECRIS originated from plasma fusion developments in the late 1960's and early 1970's. Observations were made as early as 1969 in during the use of ECRH (Electron Cyclotron Resonance Heating) in plasma devices to produce high charge state ions [Ge70,Po70], and the early extracted beams from these devices were reported in 1972 [Bl72,Wo72]. Following the pioneering work of R. Geller and his coworkers at Centre D'etudes Nucleaires de Grenoble, France, where the ECRIS originated, there are now about 40 ECRIS in operation or under construction around the world. The coupling of ECRIS to cyclotrons has resulted in significant performance gains in energy, intensity, reliability and in the variety of ion species available. At least five ECRIS have been dedicated for atomic physics research, and at many facilities atomic physics programs share ECRIS with nuclear science programs. Although ECRIS have wide application, it is still a relatively young technology. The dynamical processes are still not understood in detail. Important unknowns include the detailed mechanism of microwave coupling for electron heating, the nature of ion heating in the plasma and the effect on ion confinement, the systematics of the

gas mixing effect [Dr85, Ma86a, An88], and the relationships between the emittance of the beams extracted from the ECRIS and the magnetic field, charge state, ion mass, ion thermal energy, space charge force and electron neutralization and so on. Further development of ECRIS will require greater understanding of these and other important issues. For ECRIS coupled to accelerators, the last area mentioned above, the beam formation process, is critical to the design and operation of the accelerator coupling line.

Most ECRIS have been built for multiply-charged positive ion injection into accelerators. The sources and injection lines generally must operate over a broad range of charges and intensities; the injection rigidity is generally set by accelerator characteristics. The pressure in the coupling line between ECRIS and accelerator is low because the ECRIS main stage pressure is low, in the range of 10^{-7} T, and it is desirable to avoid the beamline constitute a source of gas for the main stage operation. The specifications for the beam transport elements are generally obtained by assuming (or extrapolating from existing data) a starting emittance at the source extraction aperture, and tracking that emittance with transport optics codes up to a match condition near the accelerator.

Generally beams are extracted DC from ECRIS. If the charge within an ion beam is not neutralized, then the charge density in space is not zero. The consequence of this nonzero charge density is that it creates an electric field within the extracted beam. For a DC ion beam with rotational symmetry, this force is predominantly outward and it will cause the beam to expand in diameter and continuously change the beam divergence due to the repulsion effects. Such space

charge effect can severely alter the beam optics if the space charge force is very strong. Due to the lack of detailed knowledge of ECRIS beam formation, the space charge effects have heretofore never been seriously addressed. Thus the space charge effects on the ECR beam transport optics have been either ignored or assumed to be non-important, though space charge effects are often studied during the design of the ion source extraction electrodes themselves.

A systematic investigation of the characteristics of the ion beams extracted from ECRIS is a complex study involving many parameters, most of which are without detailed knowledge as mentioned previously. Though the importance of studying the ECR ion beam formation has been realized by many ECR workers, up to now, only a limited number of emittance measurements of ECR ion beams with very little systematics [Ba86, Cl87, Dr83, Dr85, Ge79, Ma83a, Ma83b, Ma86b, Kr86, Tu80, Wo86, An88] have been reported since the first high charge state ion beams were extracted from ECRIS in 1972. None of these measurements has clearly revealed the characteristics of the ECR beams, partly because of the lack of systematics, and partly because good emittance measurements are difficult to make.

In an effort to understand better the requirements for matching ECRIS beams to the superconducting cyclotrons at NSCL, we have undertaken an analysis of the beam formation process on the RTECR [An86a], including the interaction of the initial beams with the first element of the beam transport system. We have found excellent agreement between BEAM_3D calculations (presented in Chapter 2) and helium beam profile and emittance measurements as a function of the total extracted beam from the RTECR, when a low degree of beam

neutralization is assumed in the calculations, as will be presented in Chapter 5. Space charge effects dominate the early beam formation and beamline optics matching process.

Initial emittance measurements on analyzed helium and multiply charged argon beams indicated rather large divergences [An88], and often triangular shaped beams in real space. To understand these measurements, we shifted to measurements on the total extracted beam before analysis, where we could make direct comparisons with the BEAM_3D code under development at NSCL.

1.2 RTECR Source and Its Beam Analysis System

The RTECR source, shown in Figure 1.1, is built for multiply-charged ion production and injection into the superconducting cyclotrons at NSCL. The solenoid coils provide the plasma axial confinement while the hexapole magnet provides the transverse plasma confinement. Microwaves can be simultaneously launched into both stages or the main stage (second stage) only. A high density lowly ionized plasma, produced in the first stage, diffuses to the main stage where highly charged ions are produced at lower pressure. The plasma chamber is positively biased with 5 - 17 kV (depending on the beam requirements), and ions leaking out of the bottom magnetic mirror are formed into a beam by the extraction electrodes located at the bottom of the source. The performance of RTECR is summarized in Table 1.1 and Table 1.2.

The beam analysis system for the RTECR is shown in Figure 1.2. The first acceleration gap was designed to be adjustable over the

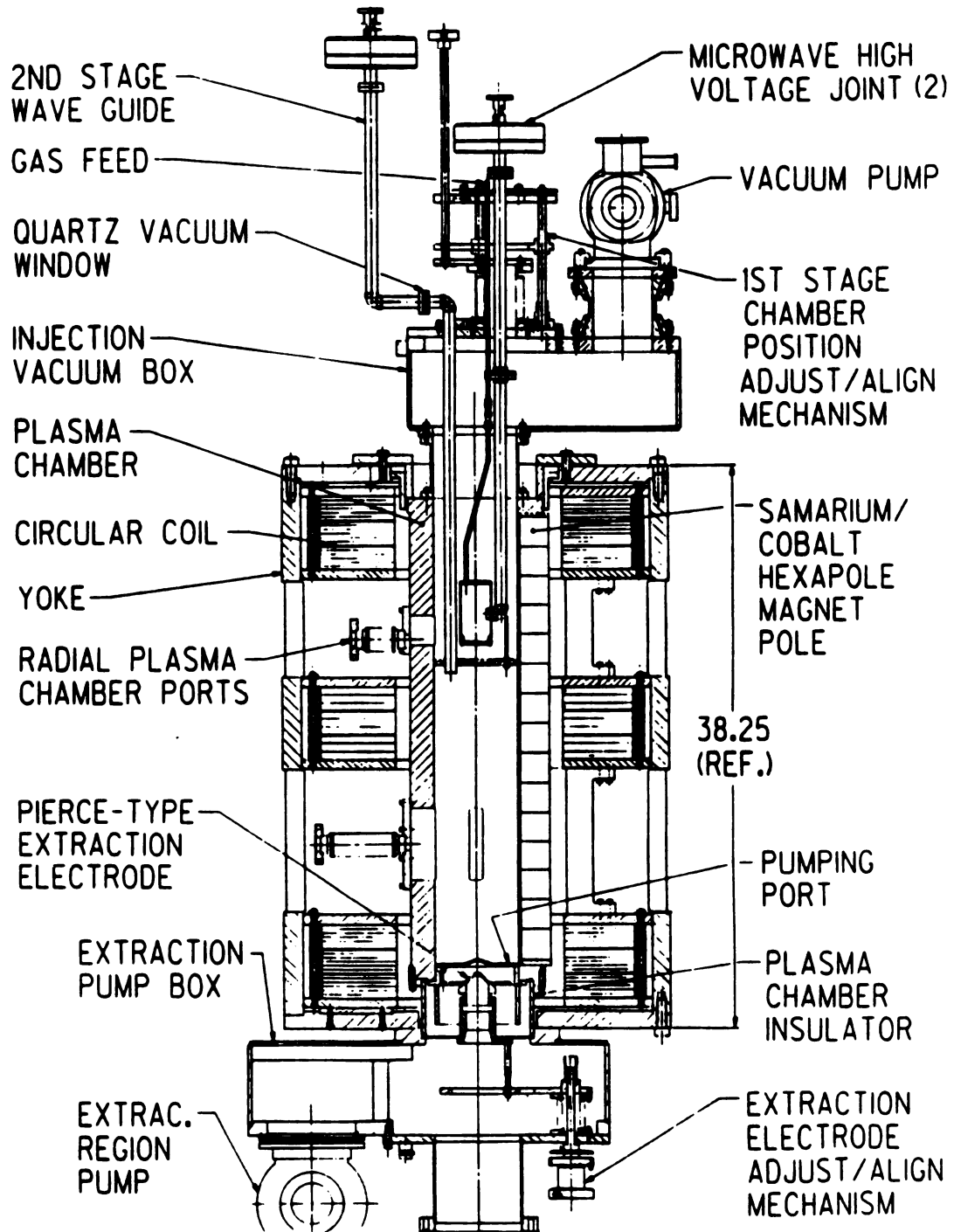


Figure 1.1. A schematic diagram showing the main features of the RTECR ion source.

Table 1.1

RTECR source DC performance for gaseous feed materials

	¹² C	¹⁴ N	¹⁶ O	²⁰ Ne	⁴⁰ Ar	⁸⁶ Kr	¹²⁹ Xe	¹²⁷ I
q								
4	25.5	100.	87.	67.	19.			
5	5.6	68.	61.	50.5	*			
6	*	25.5	52.	41.1	42.			
7		*	12.2	16.5	55.			
8			*	5.0	94.			
9				1.0	44.			
10				*	*	23.		
11					7.6	*		
12					2.0	23.3	2.3	
13					.33	29.0	2.5	1.7
14					.15	29.0	2.7	2.3
15						23.2	2.9	3.0
16						*	3.1	*
17						6.8	3.0	2.7
18						3.2	2.7	*
19						1.4	2.3	2.5
20						0.4	1.4	2.3
21							0.8	2.1
22							.45	1.8
23							.20	1.0
24							.11	*
25								.035

Conditions: 10 kV extraction voltage; 8 mm extraction aperture;

All currents in unit eμA.

* Mixed Q/M.

Table 1.2

RTECR source DC performance for solid feed materials

q	^7Li	^{19}F	^{24}Mg	^{28}Si	^{51}V	^{181}Ta
1	14.5	5.0	4.5	2.5		
2	14.5	5.0	8.4	1.0	6.1	
3	1.5	8.0	11.3	0.6	7.8	
4		14.0	13.5	1.7	8.7	
5		12.0	16.	2.1	11.7	
6		7.0	*	3.0	12.6	
7		2.0	0.7	*	15.2	
8		0.1		0.6	13.5	
9				0.2	6.5	0.4
10					4.0	*
11					1.7	0.5
12						1.0
13						*
14						1.6
15						*
16						3.1
17						3.6
18						3.6
19						3.1
20						2.7
21						2.0
24						0.6
27						0.11
29						0.08

Conditions: 10 kV extraction voltage; 8 mm extraction aperture;

All currents in unit eμA.

* Mixed Q/M.

range of 0 - 3.3 cm. The source extraction aperture is placed at the object of a solenoid focussing lens which focuses it, with unit magnification, to the object of the 90° dipole magnet at Faraday Cup #1. The solenoid focal length was chosen to put the ion source on the main floor level and to allow Ar^{1+} ions to be focussed at a source bias of 10 kV. The double focussing dipole images the beam with unit magnification at Faraday Cup #2. The beam pipe and solenoid I.D.'s are 15 cm, while the dipole aperture is 10 cm. An emittance of $\pm 5 \text{ mm} \times \pm 40 \text{ mm mrad}$ at the source extraction aperture was assumed in the design of the analysis system. Space charge effects were ignored in these design calculations. The acceptance of the dipole can be limited by changing adjustable object, divergence and image defining slits. Emittance measurements are possible on both the object and image sides of the 90° dipole. In a vacuum box at a position of large beam size before the 90° entrance, emittance measurements are made by imaging a defining slit pattern on Kapton film, which darkens on exposure to the beam, making an image with well defined edges. In the FC#2 box, we can make emittance measurements in either transverse plane with an on-line wire scanner, or with Kapton film exposures or both. These measurement techniques are discussed in Chapter 3. The two methods are complementary. The wire scanner method allows quick determination of the emittance for a variety of tuning conditions but obscures the coherent emittance, while the Kapton film method shows coherent effects such as relative beam motions and multiple beams.

The initial performance of this analysis system, as described above, is as follows. With a total extracted current of 0.5 - 1.5 emA at 10 kV (with various source geometries and tuning conditions), the

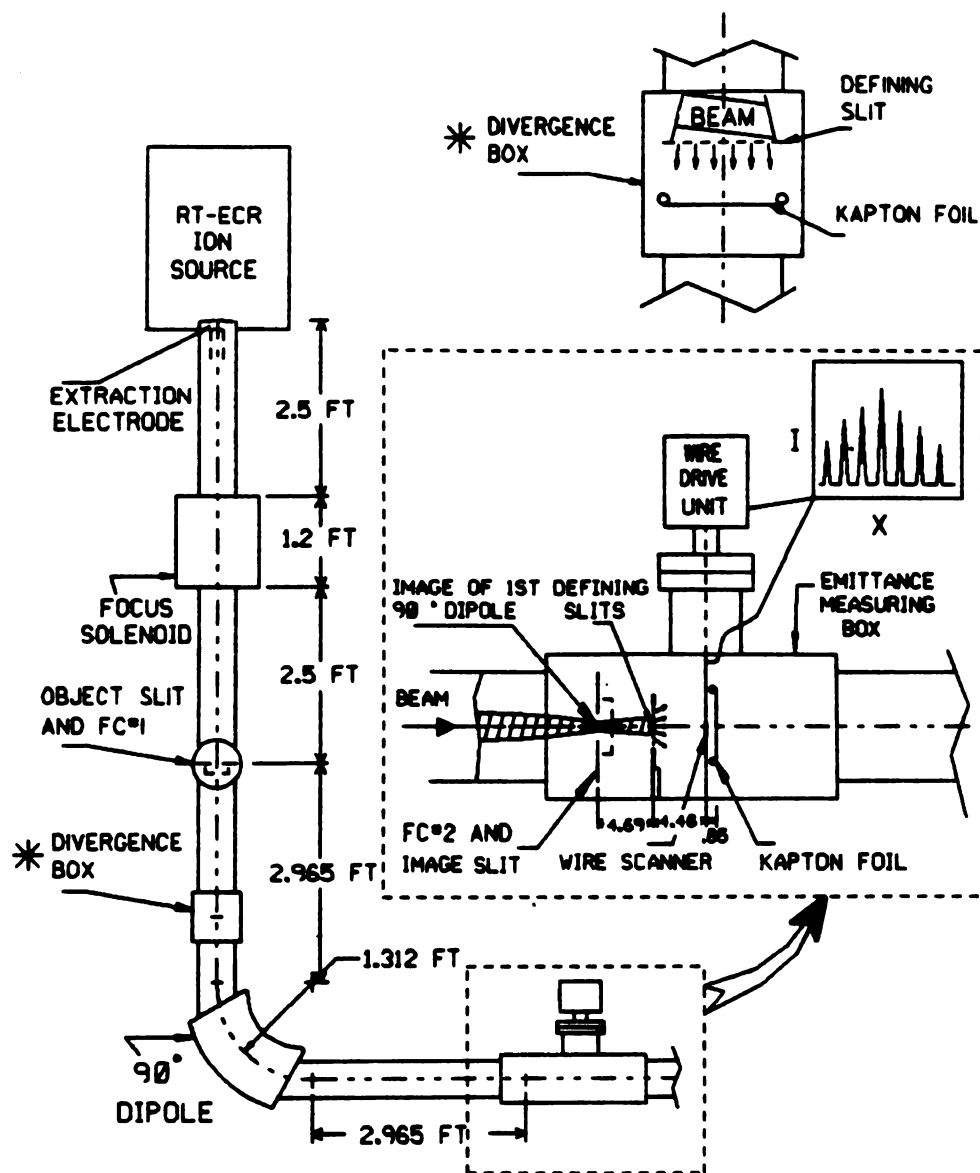


Figure 1.2. A schematic view of the RTECR analysis system and the beam analysis systems built for the studies presented in this thesis.

first acceleration gap optimized at the maximum possible value of 3.3 cm with zero voltage on the decel electrode. The hard edge emittance [De83, Ha87] of a helium 1+ beam after extraction should be expected to be 70 - 100 mm mrad at 10 kV for an 8 mm extraction aperture and $B = 2.5$ kG, but all early measurements of the emittance after the solenoid were much higher [An88]. With an analysis acceptance of about 300 mm mrad, the dipole image was always about twice the object size, suggesting aberrations, and the overall transmission, measured as the ratio of FC#2 peak currents to the net extracted current (source bias current minus the drain current for no plasma or puller current), or as $I_{FC\#2}/I_{FC\#1}$, was about 40 - 45%. The cause of this overall low transmission, typical for many ECR sources [An89], was not understood.

1.3 He Beam Technique

We have found that helium plasmas, tuned to maximize the helium 1+, provide good beams for studying the beam formation process in the RTECR. There is a large enough difference in source conditions for helium 2+, such that the total extracted current is at least 90-95% helium 1+, as shown in the spectrum in Figure 1.3. In this regard hydrogen does not work as well - H_2^+ and H^+ production are more closely coupled in ECRIS, and of course any heavier mass species will have a distribution of extracted charges. The RTECR has a wide dynamic range of helium 1+ production - from a few microamps to milliamps, even at fixed low microwave power and essentially constant magnetic field. The required microwave power is ≤ 100 watts, while we typically use 1.2 kW for high charge argon ion production. We expect low thermal

energies at such low input powers [Jo84], further simplifying the beam formation process, but the main value of using these helium 1+ plasma is that the extraction gaps and voltages are uniquely specified as a function of space charge for a single charged species as will be shown. With this simple He¹⁺ beam extraction over a broad range of intensities, the effect of space charge on the beam formation and matching is much clearer than when multiple ion species are extracted, aids with the analysis, while the results should still be applicable to the more general case encountered.

He Spectrum, $V_{ex} = 10$ KV, $V_p = 0$, RF = 80 Watts

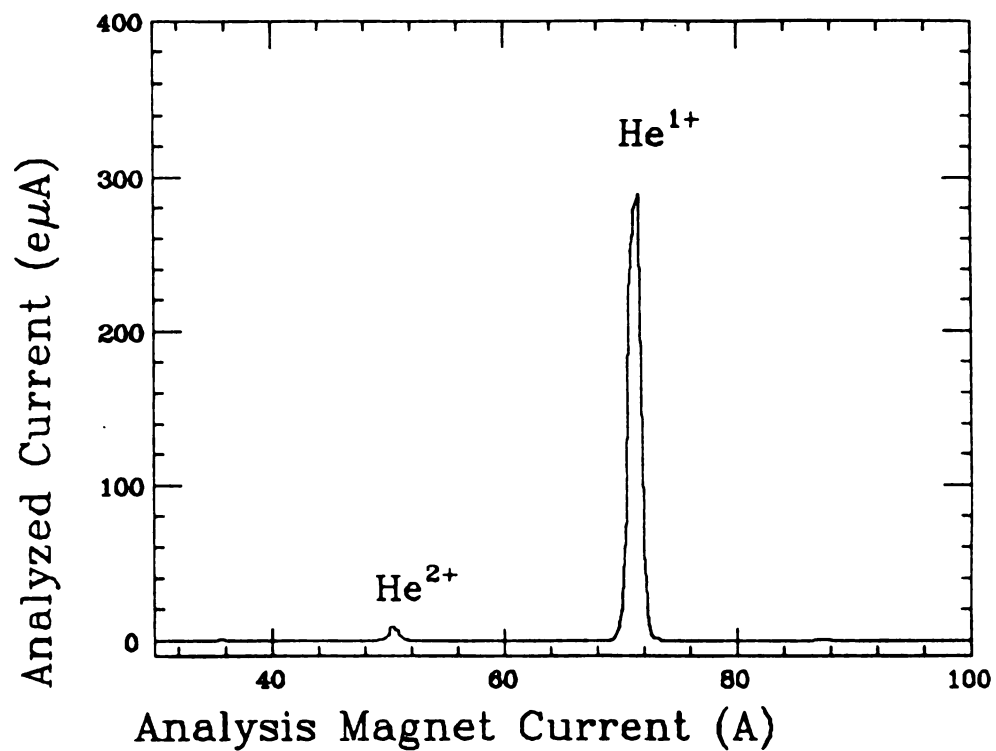


Figure 1.3. A helium spectrum is shown here. 300 e μ A helium 1+ was produced by the RTECR source at $V_{ex} = 10$ kV, $V_p = 0$ and 80 watts of RF power, while less than 5% helium 2+ was produced.

Chapter 2

The BEAM_3D Code

2.1 Motivation

As mentioned previously, ECRIS for multiply-charged ions can produce multiple ion species simultaneously. The beam formation process involves the electric fields produced by the extraction electrodes, magnetic fields from source solenoid coils, iron yoke and multipole magnets, the charge state distribution (CSD), space charge force, the plasma boundary, the ion thermal energy and beam neutralization. One would like to know what parameters are the most important for beam quality and accelerator transport matching. To answer this question, one generally makes simplifying assumptions. The typical assumptions made are to study only a single ion species and azimuthal field symmetry, in order to reduce the calculations or apply an existing code, such as the SLAC Electron Trajectory Code [He79]. One exception would be KOBRA3, developed at GSI, in which some calculations were done in 3D for ECRIS extraction [Sp85], but only with extraction of the single species O^{3+} . However, the existing codes do not include the total magnetic field in an ECRIS extraction region in a 3D calculation of the ion trajectories, while also taking the other parameters mentioned above into consideration at the same time. In order to support theoretically the ECRIS beam extraction experimental measurements of this dissertation, a new code, BEAM_3D has been developed.

2.2 General Organization

Shown in Figure 2.1 is a flow chart of the present BEAM_3D code. First, primary data input, such as the field data files (which will be explained in later section), CSD, ion thermal energy, extraction voltages and the focussing solenoid specifications. Second, ion ray tracing in the combined fields is performed with an axial step size of a few tenths mm to 1 mm, and a sequential output data file is generated. Third, a routine evaluates the emittances at requested locations and prepares a plot data output file. Fourth, graphic output, including ion trajectories in actual dimensions, is generated on a line printer.

Details involved in these calculations are presented below.

1. Assumptions

The present operating code is based on the following assumptions: (1) the space charge force has only a radial component; (2) the volume charge density in the region of a very short cylinder beam of radius r is constant.

2. Starting conditions

The code can handle up to 300 rays (or more if the computer memory space is available) with different Q/M ion species, each ray is partitioned, by input, with a portion of the total starting current. The plasma boundary is not taken into consideration yet due to lack of detailed knowledge. The ions are emitted from a plane at the chamber side of the extraction aperture perpendicular to the optical axis. The initial particle positions can be input or uniformly generated by

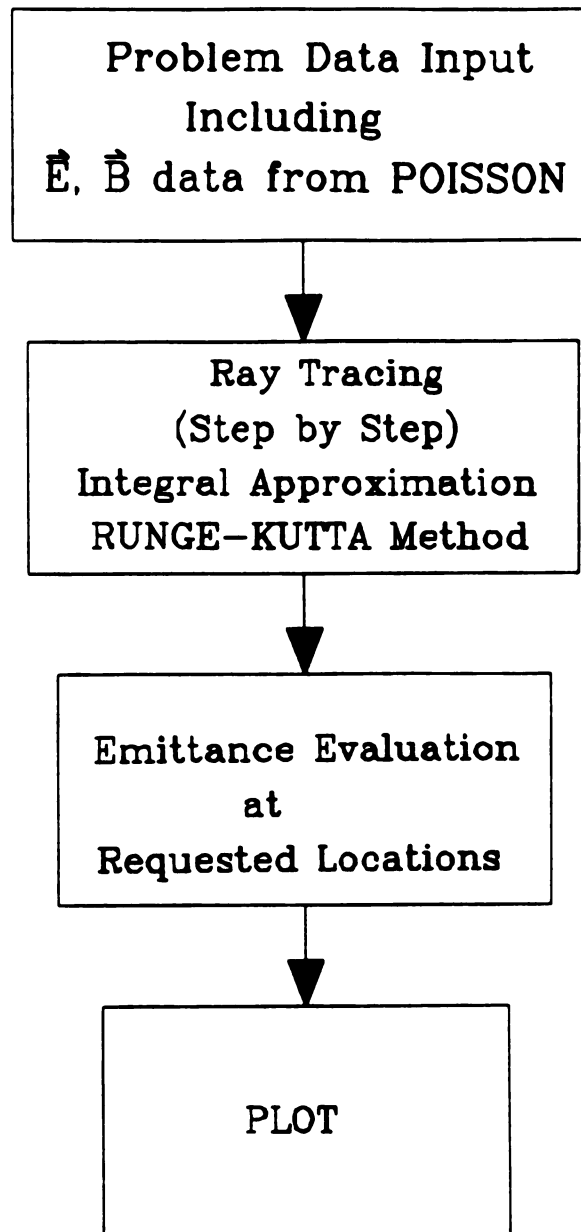


Figure 2.1. Flow diagram of the BEAM_3D code.

the code itself over the extraction aperture. Initial ion thermal energy can be input or by giving a maximum thermal energy in the unit of eV x q, then a uniform distribution to this given maximum is assumed by the code.

3. Integration of the Equation of Motion

The equation of motion of a charged particle in a magnetic and electric field is described by the Lorentz equation

$$\frac{d\vec{P}}{dt} = Q(\vec{E} + \vec{v} \times \vec{B}) \quad (2.1)$$

where Q is the charge that the particle in question carries. We change the independent variable from t to z through the relation

$$\frac{d}{dt} = v_z \frac{d}{dz} \quad (2.2)$$

to obtain the following equation

$$\frac{d\vec{P}}{dz} = \frac{Q}{v_z} (\vec{E} + \vec{v} \times \vec{B}) \quad (2.3)$$

The general analytic solution of Eq. (2.3) is not possible, because of the coupling terms in the component equations, but a numerical solution is possible but is sensitive to the calculation step size. The Runge-Kutta integration technique [Ro66] is used in BEAM_3D to solve the integral equations for \vec{v} and \vec{r} .

4. Interpolation of the External Fields

The electric fields of the extraction electrodes and magnetic fields due to the solenoid coils and iron yoke, which have azimuthal symmetry, are calculated by the POISSON code [Ho79] with a small mesh spacing in the r and z directions. The fields at a point $P(r,z)$ between grid points, as shown in Figure 2.2, are linearly interpolated using the following two dimensional formulae [Xi87]

$$F_z(r,z) = \frac{(r-r_1)}{(r_2-r_1)(z_3-z_1)} [(F_{z_4}+F_{z_1}-F_{z_3}-F_{z_2})(z-z_1)+(F_{z_2}-F_{z_1})(z_3-z_1)] + \frac{(F_{z_3}-F_{z_1})}{(z_3-z_1)} (z-z_1)+F_{z_1} \quad (2.4)$$

$$F_r(r,z) = \frac{(z-z_1)}{(r_2-r_1)(z_3-z_1)} [(F_{r_4}+F_{r_1}-F_{r_3}-F_{r_2})(r-r_1)+(F_{r_3}-F_{r_1})(r_2-r_1)] + \frac{(F_{r_2}-F_{r_1})}{(r_2-r_1)} (r-r_1)+F_{r_1} \quad (2.5)$$

where \vec{F} stands for \vec{E} or \vec{B} field.

By using POISSON for the magnetic field generation, BEAM_3D automatically takes into consideration any iron included in the problem. The hexapole field is incorporated into the total magnetic field by calling a subroutine "HEX" [Xi86]. Our BEAM_3D calculations have shown, however that the effect of the hexapole field on the beam formation is on the order of 1%, because the hexapole strength up to the typical extraction aperture radius is much less than the solenoid coil strength. So BEAM_3D calculations are usually done without the hexapole field to speed up the calculation.

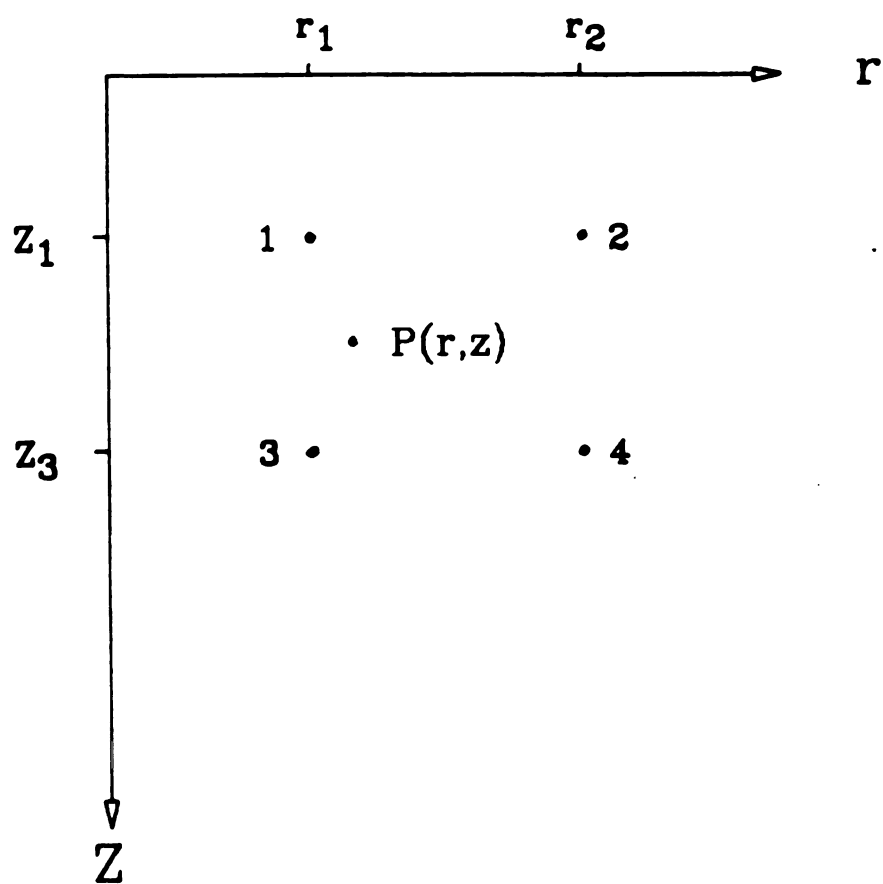


Figure 2.2. This figure shows the grid points involved in the interpolation of field components of an intermediate point $P(r, z)$.

5. Estimation of Space Charge Force

The space charge force for multiple ion species is handled, based on the assumptions (1) and (2), in the following way, similar to the model established for the beam of a single ion species [Br67]. The space charge force due to the charge inside the volume of a cylinder of radius r , shown in Figure 2.3, is evaluated by Gauss's law

$$\epsilon_0 \oint \vec{E} \cdot d\vec{s} = \int \rho dv = Q_t = \sum Q_i \quad (2.6)$$

where $Q_t = \sum Q_i$ is the total charge, and Q_i is the charge of the i -th ion enclosed by the volume of $\pi r^2 l$. Integration of the left side of Eq. (2.6) after some rearrangement gives

$$E_r = \frac{1}{2\pi\epsilon_0 r} \sum \frac{Q_i}{l} \quad (2.7)$$

or

$$E_r = \frac{1}{2\pi\epsilon_0 r} \sum \lambda_i = \frac{1}{2\pi\epsilon_0 r} \sum \frac{I_i}{v_{zi}} \quad (2.8)$$

where $\lambda_i = \frac{Q_i}{l} = \frac{I_i}{v_{zi}}$ is the uniform line charge density of the i -th species, I_i being the corresponding contribution to the total current, and v_{zi} is the velocity in the z direction of the i -th ion species. In the initial extracted beam before a dipole magnet, all of the ion species contribute to the space charge force. Since the charge state distribution varies rapidly with the charge state q , the trajectories of individual ion species will be quite different. To properly

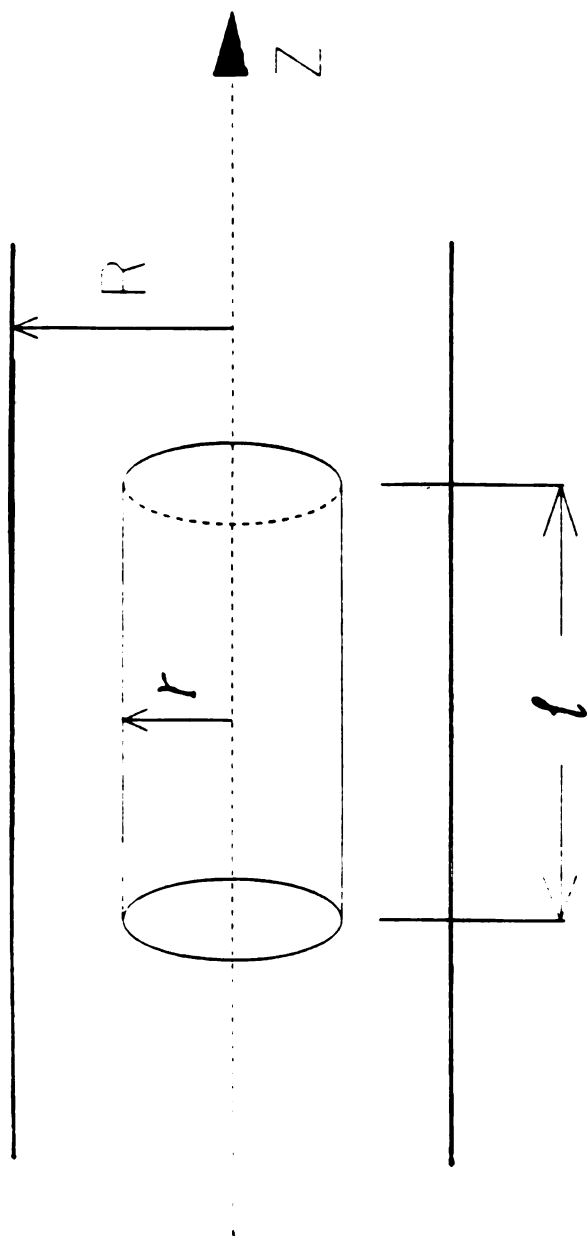


Figure 2.3. The geometry used in the calculation of the space charge force.

estimate the space charge force on each ray, BEAM_3D recomputes the space charge force on each ray by counting only the current enclosed by its orbit.

6. Geometry of Calculation

BEAM_3D will track the beam from the source extraction region through the first focussing solenoid and a beam collimating slit down to the entrance of the 1st 90° analysis magnet as shown in Figure 2.4. The z-axis is taken as the beamline optical axis. In the initial beamline, after the source extraction electrodes, is an X-Y steering magnet (which is not taken into consideration in this code, and was generally set to zero for beam studies), followed by the focussing solenoid. A beam defining slit is located at the image of the focussing solenoid and this image is the object of the 1st 90° analysis magnet. Computing the beam trajectories through the focussing solenoid to the entrance of the 90° magnet is very essential, as will be seen, for a proper matching of the ion source extraction to the beam transport system.

7. Output Form

Figures 2.5 - 2.8 show the graphic outputs of a helium beam calculation. The orbits of the ions are plotted in the r-z plane, with the extraction electrodes, shown in Figure 2.5, the focussing solenoid and the beam defining slit indicated at the proper locations as well as the ion orbits in the transverse X-Y plane. In this calculation of both He^{1+} and He^{2+} ions, He^{2+} is over-focused because the solenoid is set for He^{1+} transport and hits the beam pipe and the

beam defining slit. The initial and final ion position distributions are shown in Figure 2.6, while Figure 2.7 shows the initial and final CSD and the emittance fittings are shown in Figure 2.8.

2.3 Special Features

The special features of the BEAM_3D code are summarized as follows:

1. The CSD can be artificially specified or based on source measurements. The focussing solenoid current is set for the focussing requirements of a selected ion species. In order to have a better simulation of the beam extraction and transport, the space charge force is determined by the distribution of multiple ion species. For a specific solenoid focussing power, some ion species will be over-focused, possibly hitting the beam pipe at some locations, while other species will be under-focused, which, depending upon exact conditions, will go through or hit the beam defining slit. Ions that are stopped by these mechanical structures are removed from consideration, the CSD is adjusted, and the subsequent space charge calculation is based only on the remaining ions.

2. The degree of neutralization of space charge can be studied by using only a percentage of the full space charge force.

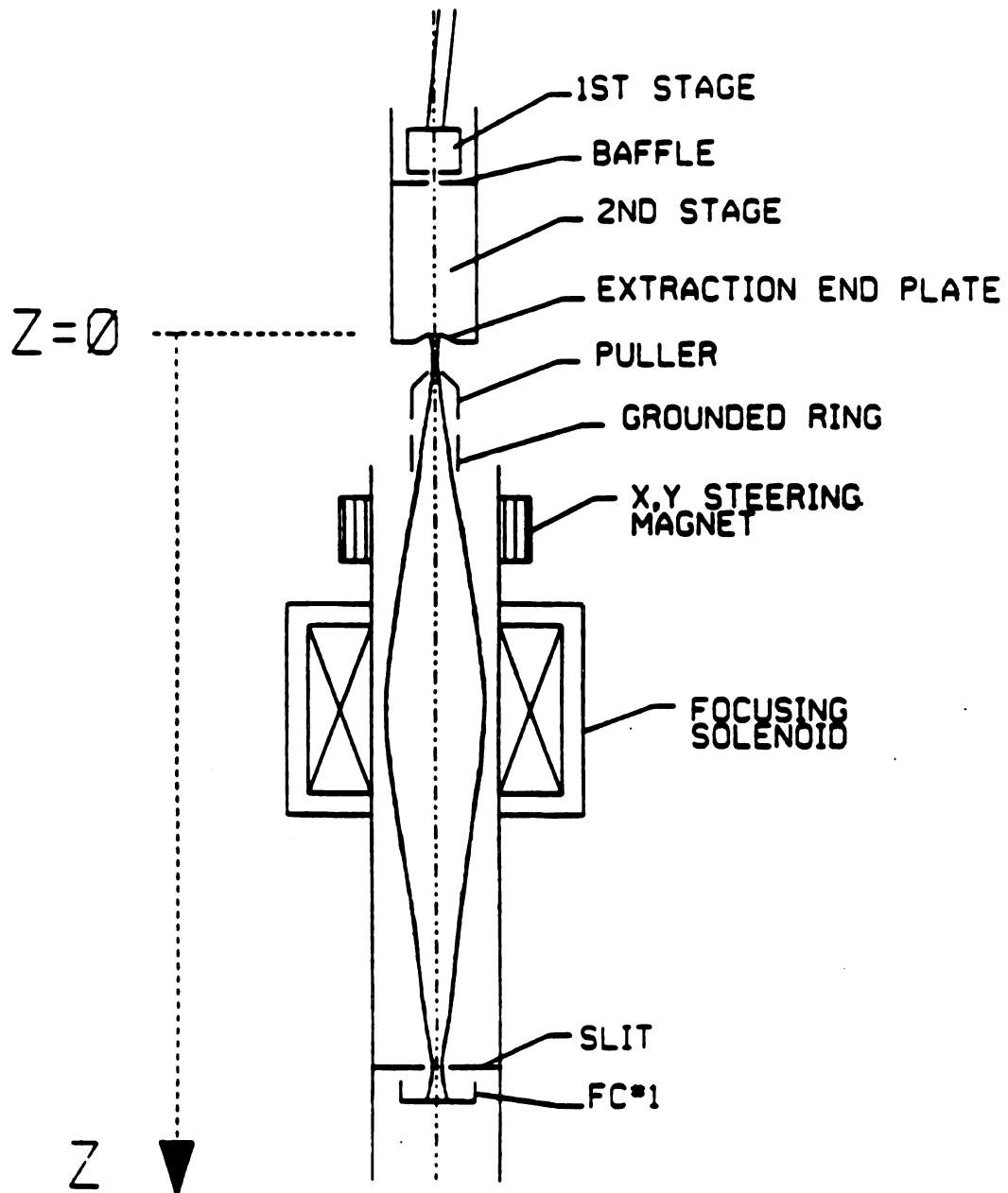


Figure 2.4. A schematic view of the extraction geometry and the initial beam transport line of the RTECR source for BEAM_3D calculation.

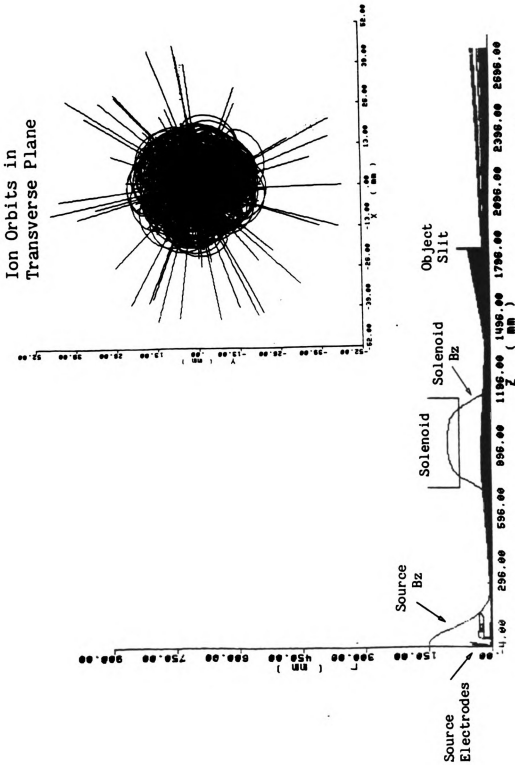


Figure 2.5. The axial and transverse ion orbits of He^{1+} and He^{2+} calculated by the BEAM_3D code.

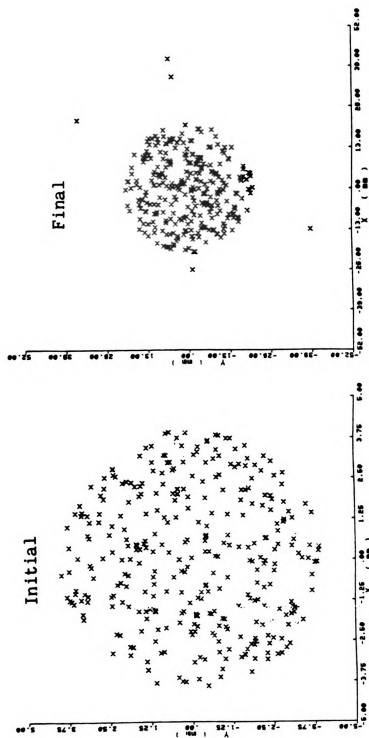


Figure 2.6. The initial and final ion position distributions.

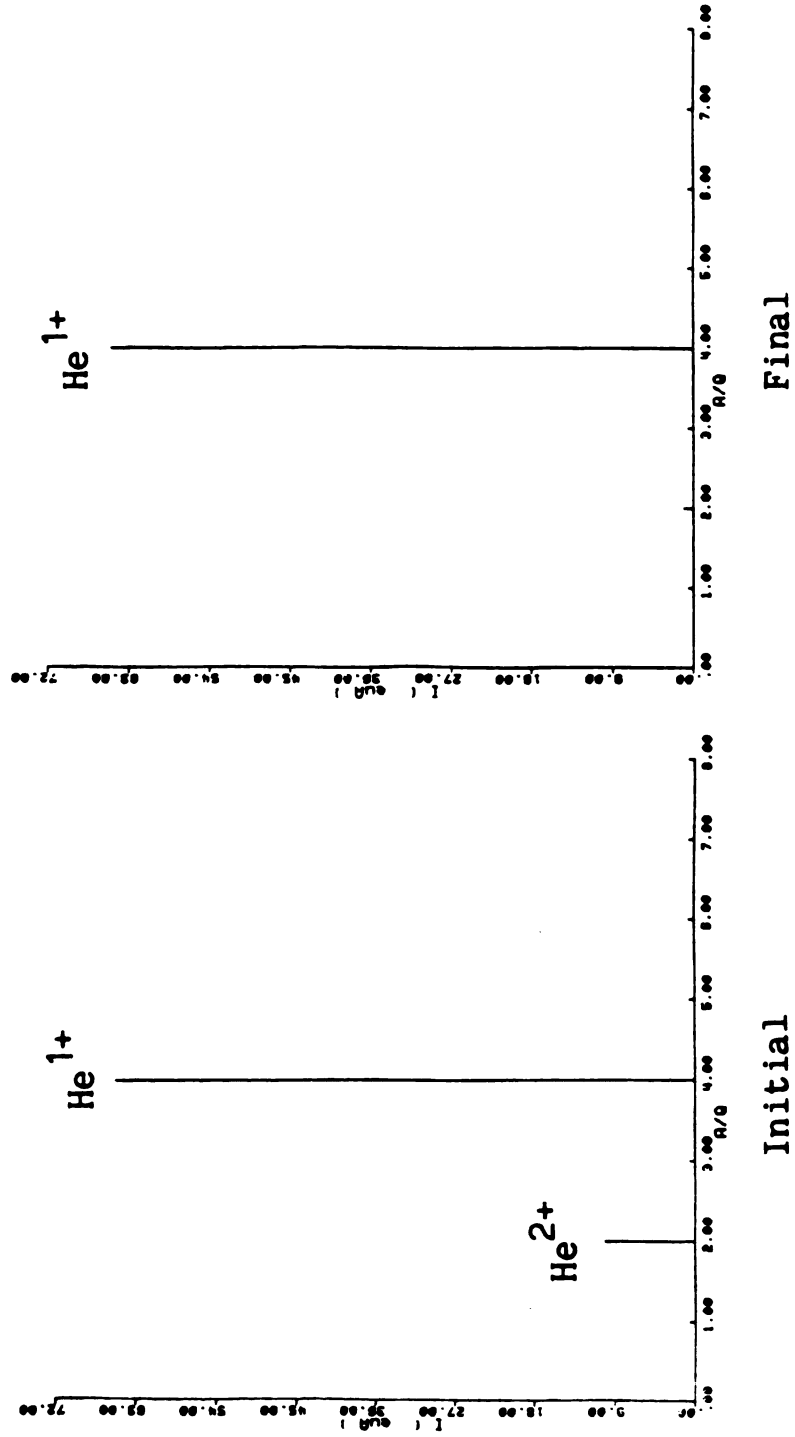


Figure 2.7. The initial and final charge state distributions (CSD).

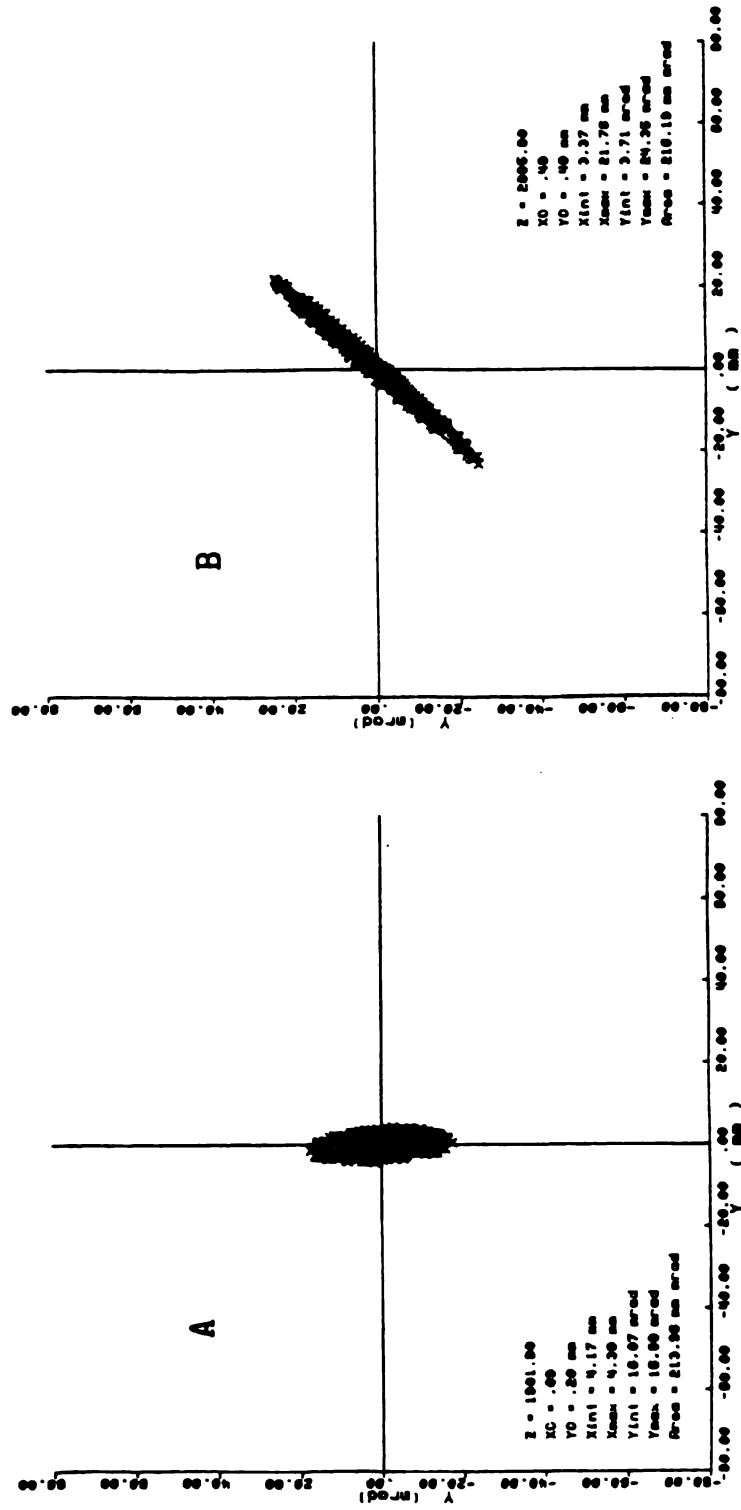


Figure 2.8. The emittance fittings. A. At the beam defining slit.
B. At the entrance of the 90° dipole.

Chapter 3

Emittance Measuring Apparatus

3.1 Theoretical Review of Emittance Measurements

At each point of any transverse section of the beam, in a region free of accelerating fields, we have an ensemble of rectilinear trajectories that form a cone of angular aperture $2d\alpha$, as shown in Figure 3.1. The slope of each ray can be simply expressed as a function of the transverse momentum p_x and of the longitudinal momentum p_z of the particle by the relation

$$x' = p_x/p_z \quad (3.1)$$

The x - x' phase-diagram of the beam is a plot of the range of values of x' as a function of x , at constant z and integrate over all y values. The area of this diagram $A(x, x')$, gives us a measure of the transverse emittance ϵ ,

$$\epsilon = A(x, x')/\pi \quad (3.2)$$

where we have followed the definition of Septier [Se67]. For a beam with no losses in a drift space without an external accelerating field, say $V(z) = \text{constant}$, this emittance is an invariant of motion (Liouville's theorem [Be67]).

As mentioned in the previous chapter, ECRIS produce multiple ion species and these ion species are extracted out of the source

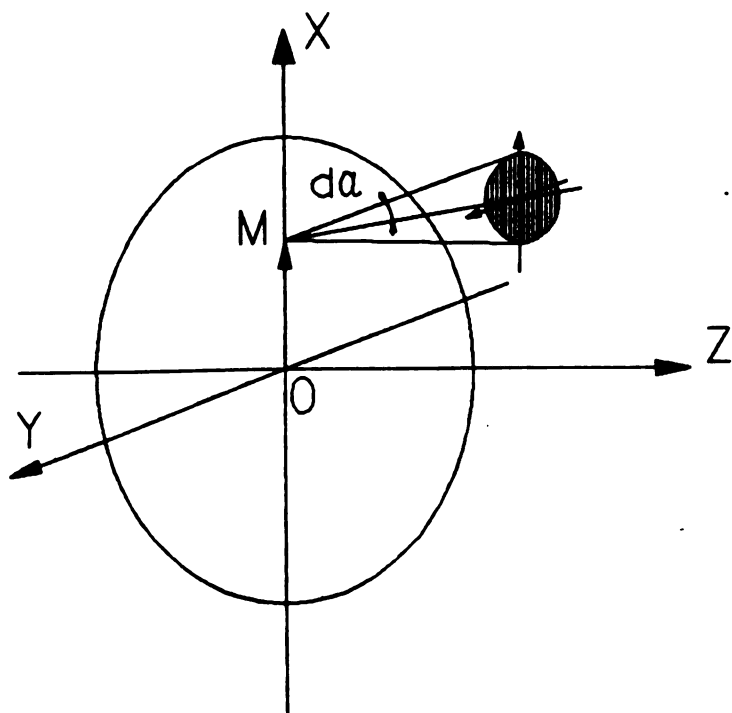


Figure 3.1. Schematic cross section of a beam.

simultaneously. However, we generally are interested in the emittance of an ion beam of single species within this ensemble. We will use the term "beam" to refer to a beam of a single ion species unless otherwise specified in the text.

The emittance of a beam with rotational symmetry in the phase plane is described by an ellipse, as shown in Figure 3.2, and this ellipse is described by the following equation, in generalized x - x' transverse coordinates

$$\left(\frac{Ax' - Bx}{a}\right)^2 + \left(\frac{Ax + Bx'}{b}\right)^2 = 1 \quad (3.3)$$

where $A = \cos\theta$, $B = \sin\theta$ and a and b are the minor and major axes of the ellipse as shown in Figure 3.2. Let $D(x)$ denote the distance between two points (1,2) on the ellipse with the same x coordinate

$$D(x) = x'(1) - x'(2) \quad (3.4)$$

Solving Eq. (3.3) yields

$$x'(1) = \frac{1}{A^2b^2 + B^2a^2} [AB(b^2 - a^2)x + ab(A^2b^2 + B^2a^2 - x^2)^{1/2}] \quad (3.5)$$

$$x'(2) = \frac{1}{A^2b^2 + B^2a^2} [AB(b^2 - a^2)x - ab(A^2b^2 + B^2a^2 - x^2)^{1/2}] \quad (3.6)$$

thus $D(x)$ is given by

$$D(x) = \frac{2ab}{A^2b^2 + B^2a^2} (A^2b^2 + B^2a^2 - x^2)^{1/2} \quad (3.7)$$

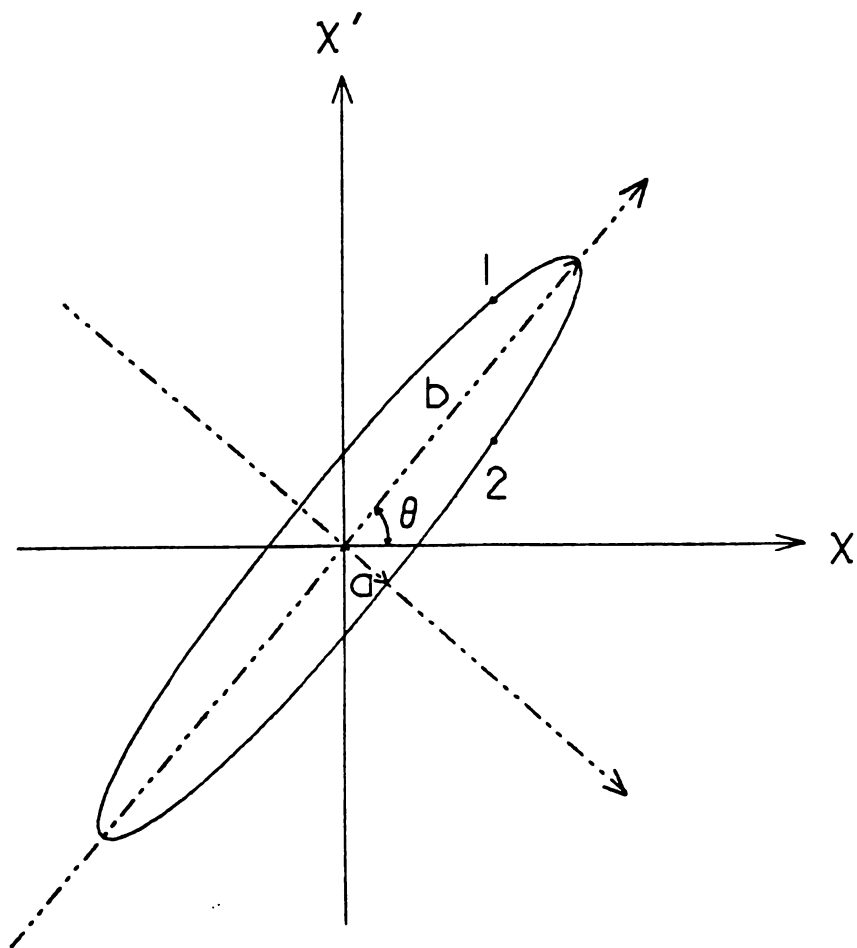


Figure 3.2. The phase area of a beam with rotational symmetry is described by an ellipse.

Eq. (3.7) indicates that $D(x)$ is an even function of x and reaches its maximum at $x = 0$.

The importance of $D(x)$ is that it can be related directly to measurable parameters. In order to measure the emittance, one generally intercepts a beam with narrow slits (to set x_i , $i = 1, 2, \dots$), followed by a scanning system, to measure the beam divergences (to measure $x'(i)$). Therefore we first consider what happens when a beam is intercepted by a slit. For a beam with uniform density σ in the phase ellipse as shown in Figure 3.3A (assume at $z = 0$), and the beam divergences are constants of the motion, then if one traces the particles that go through a slit (shaded area determined by 4 points (1,2,3,4) as shown in the ellipse), to a distance of l or L , one will find these particles evolve to an area still determined by those 4 points (1,2,3,4) as shown in Figures 3.3B and 3.3C. And the particle's coordinates in $X-X'$ have the relationships to the coordinates $x-x'$ at $z = 0$

$$\begin{aligned} X_i &= x_i + lx'(i) \\ X'(i) &= x'(i) \end{aligned} \quad (3.8)$$

The detailed expression of $D(X)$ for the two cases of Figure 3.3B and 3.3C will be derived below.

For Figure 3.3B, the 4 points (1,2,3,4) in the $X-X'$ coordinates are given by

$$\begin{aligned} X_1 &= x_1 + lx'(1) & X'(1) &= x'(1) \\ X_2 &= x_1 + lx'(2) & X'(2) &= x'(2) \end{aligned}$$

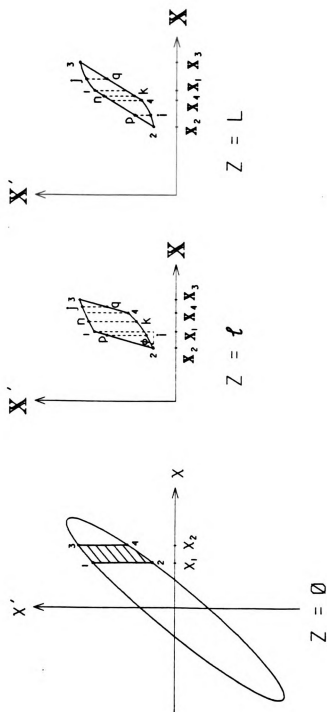


Figure 3.3. The particles which lie in the shaded area of the shown ellipse ($z = 0$) will evolve to either of the cases in B ($z = l$) or C ($z = L$) after a drift distance.

$$\begin{aligned}
 X_3 &= x_2 + 1x'(3) & X'(3) &= x'(3) \\
 X_4 &= x_2 + 1x'(4) & X'(4) &= x'(4)
 \end{aligned} \tag{3.9}$$

Graphically one can see that

$$\text{Tan}\phi = \frac{X'(1) - X'(2)}{X_1 - X_2} = \frac{X'(1) - X'(2)}{1[X'(1) - X'(2)]} = \frac{1}{1} \tag{3.10}$$

then the divergence of particle p on the line 1-2 would be

$$X'(p) = x'(2) + (X_i - X_2)\text{Tan}\phi_1 = x'(i) + \frac{x_i - x_1}{1} \tag{3.11}$$

Thus the vertical distance between point p and point i is given by

$$D(X)_{p-i} = X'(p) - X'(i) = \frac{x_i - x_1}{1} \quad X_2 \leq X_i \leq X_1 \tag{3.12}$$

likewise, the distance between $X'(j)$ and $X'(q)$ is

$$D(X)_{j-q} = \frac{x_2 - x_j}{1} \quad X_4 \leq X_j \leq X_3 \tag{3.13}$$

In the interval between X_4 and X_1 , the vertical distance between points n and k is determined by

$$D(X)_{n-k} = \frac{x_k - x_n}{1} \quad X_1 \leq X_k \leq X_4 \tag{3.14}$$

Although x_1 and x_2 are known, the other x_i between region $[x_1, x_2]$ are not. In order to have a distribution of $D(X)$ in the $X-X'$ coordinates,

$D(X)$ should be expressed as the function of X . Let $a = A^2 b^2 + B^2 a^2$, $B = ABl(b^2 - a^2)$ and $\gamma = abl$, we use the relation

$$x'l + x = X \quad (3.15)$$

to obtain the following equations,

$$D(X)_{p-i} = \frac{1}{l} \left\{ \frac{1}{\gamma^2 + (a + B)^2} [a(a + B)X + \gamma(a(\gamma^2 + (a + B)^2) - a^2 X^2)^{1/2}] - x_1 \right\} \quad x_2 \leq X \leq x_1 \quad (3.16)$$

$$D(X)_{n-k} = \frac{1}{l[\gamma^2 + (a + B)^2]} [(a(\gamma^2 + (a + B)^2) - a^2 X^2)^{1/2}] \quad x_1 \leq X \leq x_2 \quad (3.17)$$

$$D(X)_{j-q} = \frac{1}{l} \left\{ \frac{-1}{\gamma^2 + (a + B)^2} [a(a + B)X - \gamma(a(\gamma^2 + (a + B)^2) - a^2 X^2)^{1/2}] + x_2 \right\} \quad x_2 \leq X \leq x_1 \quad (3.18)$$

Similar analysis gives the $D(X)$ distribution for the case of Figure 3.3C

$$D(X)_{p-i} = \frac{1}{L} \left\{ \frac{1}{\gamma^2 + (a + B)^2} [a(a + B)X + \gamma(a(\gamma^2 + (a + B)^2) - a^2 X^2)^{1/2}] - x_1 \right\} \quad x_2 \leq X \leq x_1 \quad (3.19)$$

$$D(X)_{n-k} = \frac{x_2 - x_1}{L} = \frac{s}{L} \quad x_2 \leq X \leq x_1 \quad (3.20)$$

$$D(X)_{j-q} = \frac{1}{L} \left\{ \frac{-1}{\gamma^2 + (a + B)^2} [a(a + B)X - \gamma(a(\gamma^2 + (a + B)^2) - a^2 X^2)^{1/2}] + x_2 \right\}$$

$$\left\{ (a + B)^2 - a^2 X^2 \right\}^{1/2} + x_2 \} \quad X_1 \leq X \leq X_3 \quad (3.21)$$

where $a = A^2 b^2 + B^2 a^2$, $B = ABL(b^2 - a^2)$, $\gamma = abL$, and s is the slit width.

Based on the assumption that the particle density σ is a constant, then the product of $D(X)$ and σ gives the line current density along the X direction by

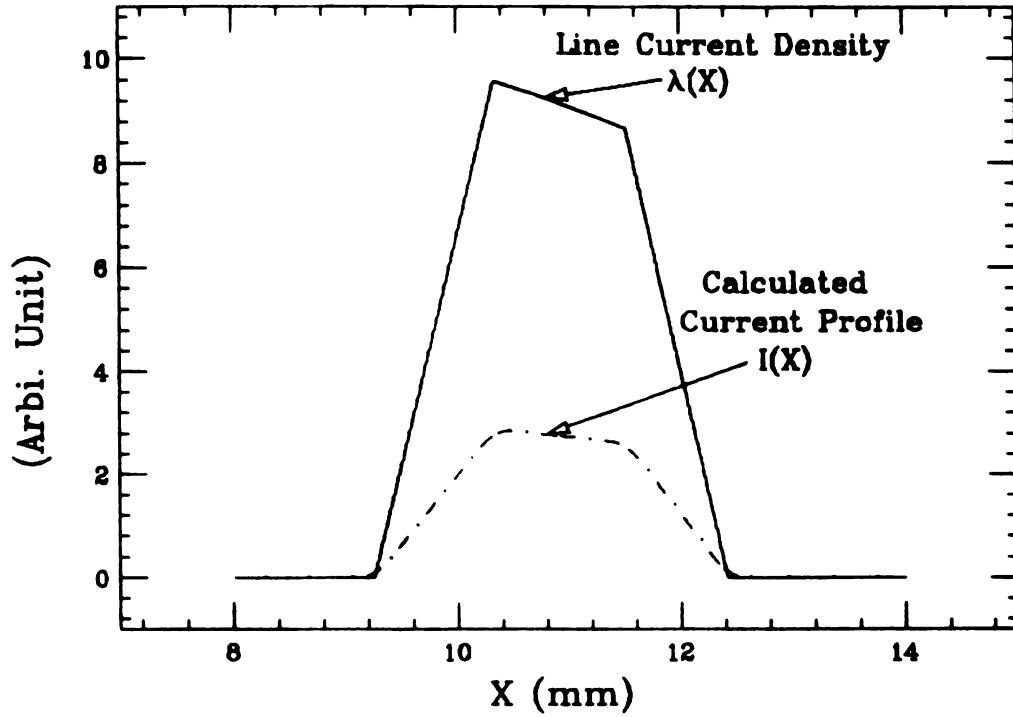
$$\lambda(X) = D(X)\sigma \quad (3.22)$$

and in arbitrary units

$$\lambda'(X) = \lambda(X)/\sigma = D(X) \quad (3.23)$$

Hence $D(X)$ is simply a line current density function. If one uses a finite width wire to scan the current after a slit and put the current intensity on the center position of the wire, one would however see a different current profile than the profile given by this line current density function $D(X)$, because of the wire width effect. Comparison of the $D(X)$ and a wire scanner current profile, if continuously measured by a finite wire of diameter $\phi = 0.3$ mm, are given in Figure 3.4 for the case of Figure 3.3B, and in Figure 3.5 for the case of Figure 3.3C. One can see that due to the finite size of the wire, the locations of X_1 , X_2 , X_3 , and X_4 are wiped out by small curvatures. But X_2 and X_3 can be determined from the locations where the beam current goes to zero.

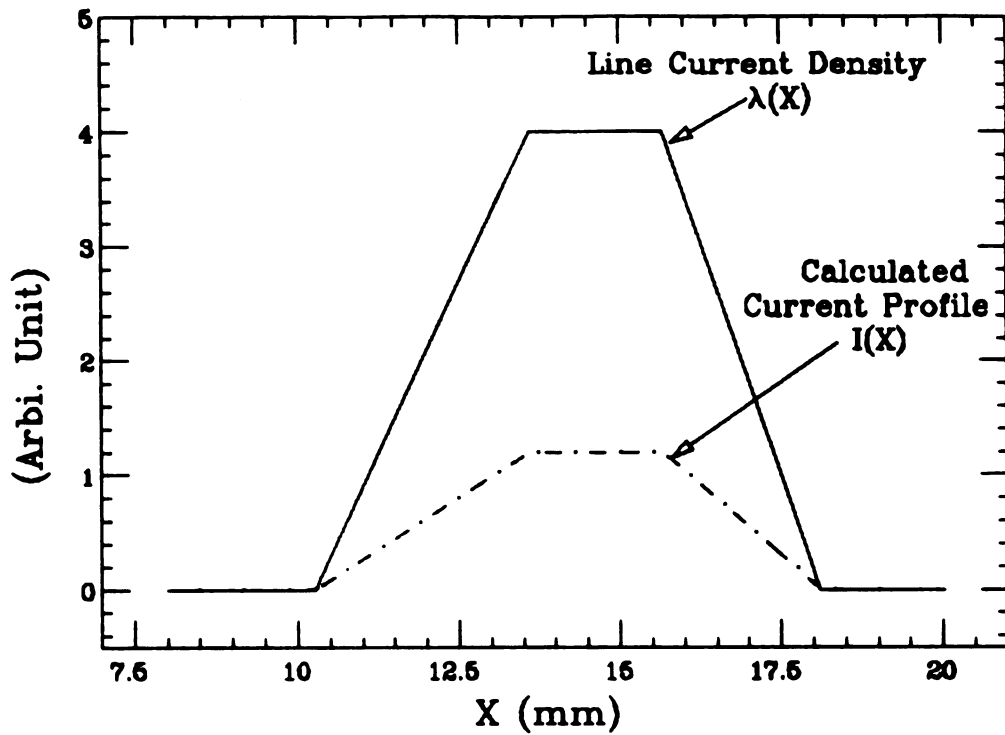
Distribution, $\theta=45^\circ$, $l=100$ mm, $\phi(\text{wire})=.3$ mm



$a = 5$ mm, $b = 20$ mrad, $x_1 = 9$ mm, $x_2 = 11$ mm

Figure 3.4. A comparison, for the case Figure 3.3B, with drift distance 100 mm, of the line current density and the calculated current profile as measured with a wire of 0.3 mm wide. The particles were initially in the area determine by $x_1 = 9$ mm and $x_2 = 11$ mm for an ellipse with a 45° orientation, $a = 5$ mm and $b = 20$ mrad, at $z = 0$.

Distribution, $\theta=45^\circ$, $L=500$ mm, $\phi(\text{wire})=.3$ mm



$a = 5$ mm, $b = 20$ mrad, $x_1 = 9$ mm, $x_2 = 11$ mm

Figure 3.5. A comparison, for the case Figure 3.3C with a drift distance 500 mm, of the line current density and the calculated current profile as measured with a wire of 0.3 mm wide. Other conditions are the same with the case in Figure 3.4.

As can be seen above, the line current density function $D(X)$ is linear in X and the square root of $(c_1 - c_2 X^2)$, where c_1 and c_2 are constants. In general, the interval ΔX between X_1 and X_2 or between X_3 and X_4 is very small, thus $\lambda(X)$ is essentially linear in ΔX in each of the three regions except for the region (X_4, X_1) of the case Figure 3.3C where $D(X)$ is a constant. Thus in each of these regions the distribution of $D(X)$ is approximately a line with a varying slope. Note that the slopes in the first and the third regions are not the same. Experimentally, when the current is continuously scanned by a finite wire, the current collected will be a function of $\lambda(X)\phi$, where ϕ is the width of the finite wire, except at the line vertices, where the edge is smeared by the change of slope. Away from the vertices, the slope of the measured current profile is simply equal to $\frac{dI(X)}{dX}$, or ϕ times the line current density slope $\frac{d\lambda(X)}{dX}$. Hence one can use the measured current values away from the vertices to determine $\frac{dI(X)}{dX}$, which divided by ϕ gives the corresponding slope $\frac{d\lambda(X)}{dX}$. Thereafter with the help of $\frac{d\lambda(X)}{dX}$, one extrapolates the positions of X_2 and X_3 . For each beamlet it will generally be easier to determine X_2 and X_3 , since the density σ may not be a constant inside the ellipse, making the identifications of X_1 and X_4 in cases 3.3B or 3.3C very difficult. That is, the current profile may not have a 'flat top' when the density is not uniform.

Once this line current distribution is correctly determined, the X_2 and X_3 will be obtained and so are $x'(2)$ and $x'(3)$ by

$$x'(2) = \frac{X_2 - X_1}{(1 \text{ or } L)}, \quad x'(3) = \frac{X_3 - X_2}{(1 \text{ or } L)} \quad (3.24)$$

Determining all such points (x, x') in the phase plane then can yield the phase area by an ellipse fitting.

3.2 Online Slit-Wire Scanner

We have built an online slit-wire scanner, which is located about 10" after the image of the analysis magnet as shown in Figure 1.2. This online slit-wire scanner allows quick determination of the emittance after the analysis magnet for a variety of tuning conditions, which is very helpful for better matching the beam transport to the cyclotrons.

This slit-wire scanner consists of a slit plate of many parallel 0.01" x 2.8" slots, 4.9" upstream of the scanning wire. The slit plate is flipped up and down by a rotatory vacuum feedthrough. One can intercept a beam to make measurements without breaking the vacuum. The scan wire is a copper wire of diameter $\phi = 0.3$ mm. Figure 3.6 shows this scanning wire and its support structure assembly. The scan wire is controlled by a servo motor via a vacuum feedthrough; it takes about 34 seconds to do one scan. We want to make such slow scans to have sufficient data for good statistics in the determination of the beamlet size after the slit plate, but the beam must be very stable. Of course, if one desires to increase the scanning rate, it is necessary only to adjust the servo motor drive. The output current signal from the scanning wire is converted into a voltage signal by a group of resistors right after the wire feedthrough on the vacuum box to avoid picking up the AC current noise through the common grounding.

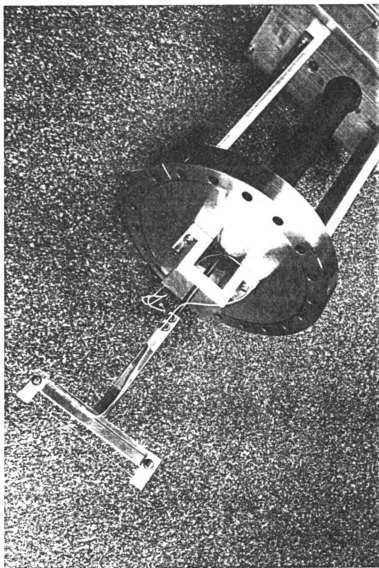


Figure 3.6. The assembly of the wire scanner.

The wire output signal and the wire position information are recorded by computer and can be analyzed on line to give the beam profile and the emittance in one transverse phase plane. In this analysis program, the beamlet edge determinations are based on the arguments outlined in Section 3.1. The divergences $x'(i)$ versus the positions x_i are determined, and the emittance is then estimated by an ellipse fitting routine. One can measure the beam profile and emittance in the other transverse phase plane by rotating the whole setup 90°. Figure 3.7 shows an Ar¹⁰⁺ beam emittance measurement made with this slit-wire scanner.

3.3 Kapton Camera

As mentioned in Chapter 1, we have also made Kapton foil burns, with a beam defining slit plate (of slot size .010" x 2.8", 3~4" upstream of the foil), to measure the helium beam profiles and emittances. This method of course can also be used to measure other beam profiles and emittances after the analysis magnet where a beam of single ion species is selected. The advantage of using this technique is that the device required is simple and gives two dimensional information (both transverse directions) at the same time, while the wire scanner moves only in one direction. It also shows coherent effects such as relative beam motion and multiple beams, which is very useful for interpreting other beam profile measurements. The disadvantage of such method is that frequent venting of the beamline vacuum may be required to remove foils. In order to reduce the beamline vacuum venting, we have designed a Kapton camera which can do 10 to 12 foil burns.

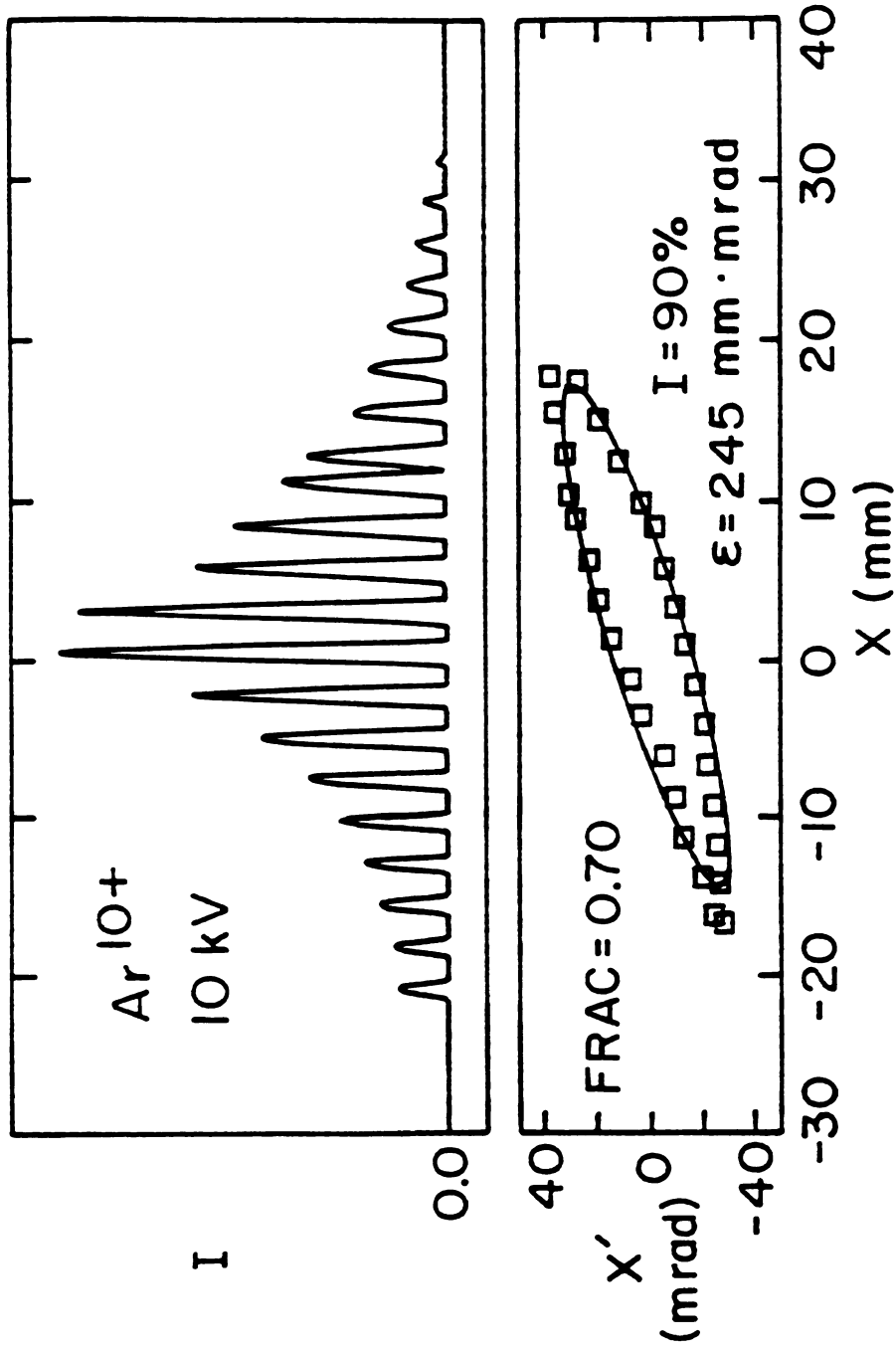


Figure 3.7. A $3 \text{ e}\mu\text{A Ar}^{10+}$ beam profile after the analysis magnet is shown. The large tail is believed due to the high divergence beam component. An ellipse fit at 90% intensity gives emittance $\epsilon = 245 \text{ mm mrad}$.

This Kapton camera is mounted on an 8" del-seal blank flange as shown in Figure 3.8. An aluminum frame centered on the beamline axis holds the two Kapton spools. Two indexing vacuum feedthroughs control the revolution of the spool, with two revolutions to advance one foil exposure. The burning time depends empirically on the beam intensity. For example, for a $10 \text{ e}\mu\text{A}/\text{cm}^2$ beam intensity, the burning time is approximately about 10 minutes. A well defined beam image on the foil can be obtained. At beam intensities in the range of $100 \text{ e}\mu\text{A}/\text{cm}^2$ or higher, ion charging effects on the Kapton foil start to blur the image. At these current densities, we image the beam onto the metallic side of aluminized Kapton foil and obtain well defined images on the Kapton side.

The emittance of the beam can be obtained by using a 5 to 10X magnifying lens to read out the beamlet edges, giving $x'(2)$ and $x'(3)$ sets for each (x_1, x_2) pair which can be used to build the phase space diagram. Results of such measurements are presented in Chapter 5.

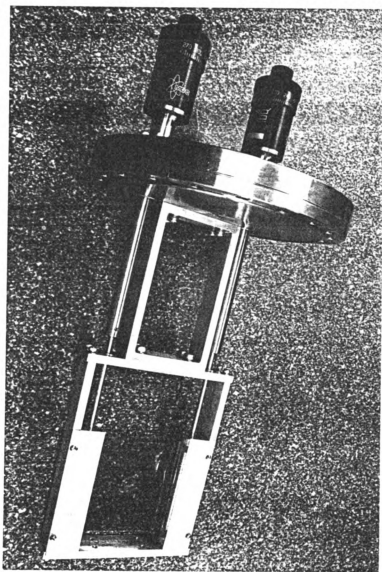


Figure 3.8. The assembly of the 'Kapton camera'.

Chapter 4

Extraction Geometry Study

4.1 Motivation

The ion beam extraction system is usually located near the peak field of the end mirror. The most common extraction system that has been used to form beams of ions from ECRIS is shown schematically in Figure 4.1A. It is a three electrode system with applied voltages V_a , V_b and V_c on the relevant electrodes respectively. Positive ions are expelled from the source and the beam transport line is at ground potential, which results in the requirements that $V_c = 0$ and $V_a > 0$. The intermediate electrode with voltage V_b is used to obtain adequate ion focussing. The beam energy is determined by $V_a - V_c = V_a$, which is set by the application, while the voltage difference $V_a - V_b$ and the spacing D between these two electrodes determine the maximum current that can be extracted from the source for a given plasma. The variation of the voltage V_b from negative to positive will enable the extraction system to be one of the 3 cases: 1. accel-decel ($V_b < 0$), as illustrated in Figure 4.1B, the region between V_a and V_b is accelerating and radially focussing while the region between V_b and V_c is with decelerating and defocussing, though the net effect of the extraction system is focussing if the focussing strength in the acceleration gap is stronger than the defocussing strength, 2. accel-only ($V_b = V_c = 0$, electrode b and c can be combined as one), as shown in Figure 4.1C, which produces only a focussing effect in the region between V_a and V_b , 3. accel-accel ($V_a > V_b > 0$), as shown in Figure 4.1D,

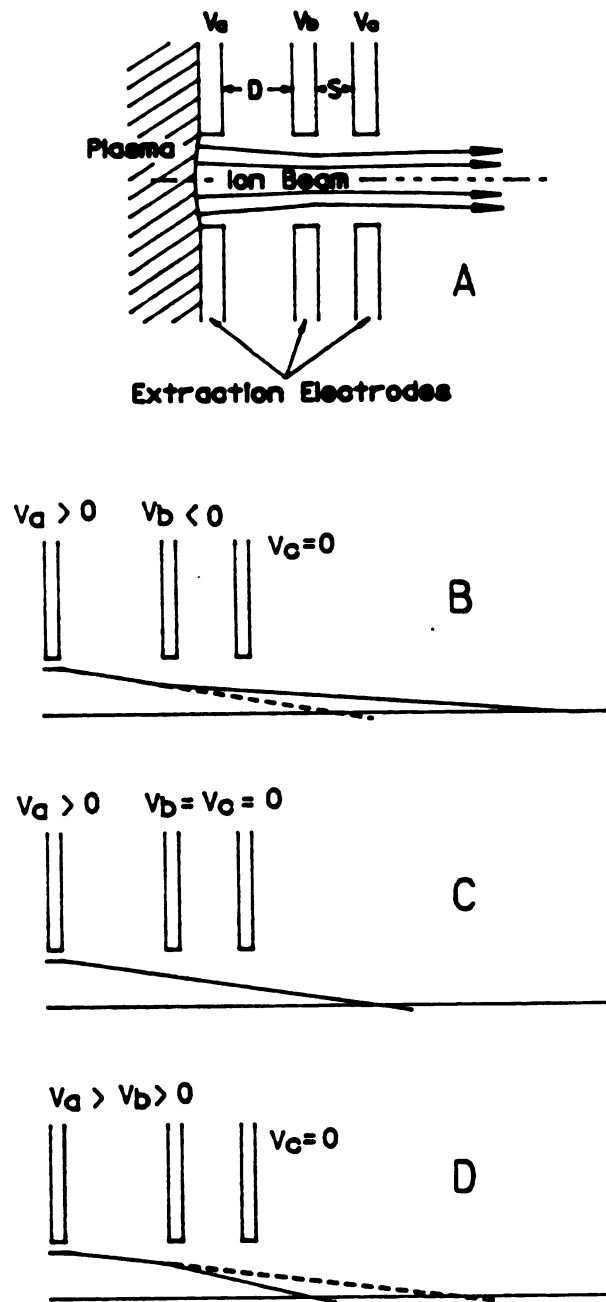


Figure 4.1. A. A schematic view of a three electrode extraction system. B. Accel-decel voltage distribution. C. Accel-only voltage distribution. D. Accel-accel voltage distribution.

with focussing strength in both gaps. For historical reasons, only cases 1. and 2. have been used in ECRIS [Jo83, Cl83, Ge79, An86, Pa87]. Such accel-decel systems used in ECRIS generally have a Pierce-type [Pi54] first electrode and various second electrode shapes (puller electrode), while the third electrode is simply a large bore ground ring. Figure 4.2A shows a schematic view of the original RTECR extraction electrode system which has a puller of a face angle 45° to the optics axis, and the first gap was adjustable from 0 to 3.3 cm by moving the puller (the second gap is fixed and moves with the puller). Shown in Figure 4.2B is the current extraction system, which has a Pierce spherical puller, and the first gap can be adjusted from 3 to 6 cm. A negative high voltage power supply feeds the puller electrode, thus the source has the ability to extract ion beams under the conditions of accel-decel or accel-only.

Although ECRIS have been under development for about 12 years, the best extraction geometry for all ECRIS or whether the best extraction geometry has a source dependence is still an open question. During the first operation of the RTECR, we have found the transmission from FC#1 to FC#2 to be low, as mentioned in Chapter 1 -- only about 40% to 45%, implying a large mismatch between the source and beam transport system. Thus an extraction geometry study on the RTECR source has been undertaken in order to ascertain the nature of this poor transmission.

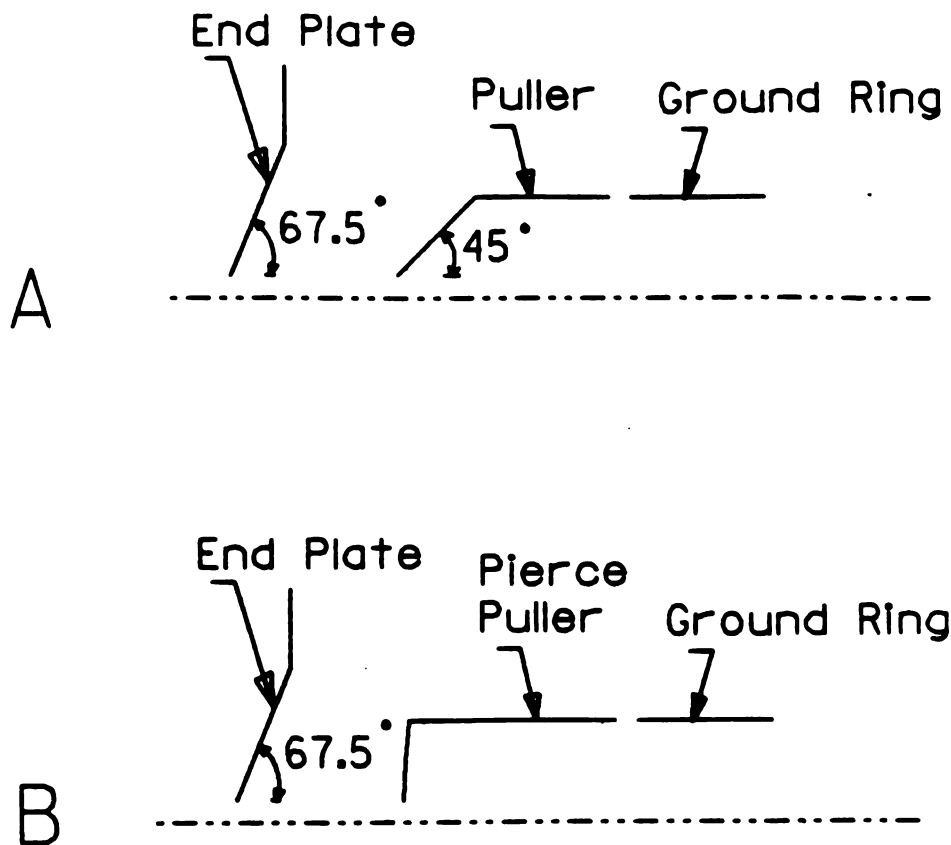


Figure 4.2. A schematic view of the two extraction electrode systems utilized in the RTECR. A. The puller has a face angle at 45° . B. The puller has a Pierce spherical face shape [P154].

4.2 Theoretical Review

4.2.1 Equations of Motion

For a magnetic field produced by solenoid coils, $A_\theta(r, z)$ is the only nonzero component of the vector potential \vec{A} . Then a charged particle of charge Q and mass M moving non-relativistically in a combination of an azimuthally symmetric electric field and a solenoidal magnetic field, the Hamiltonian (in cylindrical coordinates) is of the form

$$H = \frac{1}{2M} \left(P_r^2 + \frac{P_\theta^2}{r^2} + P_z^2 + Q^2 A_\theta^2 - \frac{2QP_\theta}{r} A_\theta \right) + QV(r, z) \quad (4.1)$$

where $P_r = p_r = Mv_r$, $P_\theta = p_\theta + QrA_\theta = Mv_\theta r + QrA_\theta$ and $P_z = p_z = Mv_z$ are the generalized momenta in which p_r , p_θ and p_z stand for the mechanical momenta, and v_r , v_θ and v_z are the linear velocities in the r , θ and z directions. $V(r, z)$ is the electric potential. Lacking the exact knowledge of space charge, for simplicity, it is assumed that the space charge has only the radial component for DC beams, then $V(r, z) = V_{\text{ex}}(r, z) + V_{\text{sp}}(r)$, where $V_{\text{ex}}(r, z)$ is due to the applied extraction potential and $V_{\text{sp}}(r)$ is the potential due to the space charge based on the above assumption. Therefore the Hamiltonian becomes

$$H = \frac{1}{2M} \left(P_r^2 + \frac{P_\theta^2}{r^2} + P_z^2 + Q^2 A_\theta^2 - \frac{2QP_\theta}{r} A_\theta \right) + Q(V_{\text{ex}}(r, z) + V_{\text{sp}}(r)) \quad (4.2)$$

The equations of motion are then obtained by differentiating Eq. (4.2) with respect to the corresponding coordinates

$$\dot{P}_r = - \frac{\partial H}{\partial r} = - \frac{1}{M} \left[- \frac{P_\theta^2}{r^3} + Q^2 A_\theta \frac{\partial A_\theta}{\partial r} - Q P_\theta \left(- \frac{A_\theta}{r^2} + \frac{1}{r} \frac{\partial A_\theta}{\partial r} \right) \right] + Q(E_{\text{exr}} + E_{\text{spr}}) \quad \text{where } E_r = - \frac{\partial V}{\partial r} . \quad (4.3)$$

$$\dot{P}_\theta = - \frac{\partial H}{\partial \theta} = 0, \quad \text{that is } P_\theta = p_\theta + Q r A_\theta = \text{constant}. \quad (4.4)$$

$$\begin{aligned} \dot{P}_z = - \frac{\partial H}{\partial z} &= - \frac{1}{M} \left(Q^2 A_\theta \frac{\partial A_\theta}{\partial z} - \frac{Q P_\theta}{r} \frac{\partial A_\theta}{\partial z} \right) + Q E_{\text{exz}} \\ &= \frac{Q p_\theta}{M r} \frac{\partial A_\theta}{\partial z} + Q E_{\text{exz}} \end{aligned} \quad (4.5)$$

Eq. (4.4) shows that P_θ is a constant of motion. An important consequence of this result is that if an ion moves from a region with the above mentioned magnetic field to a magnetic field free region, the magnetic angular momentum $Q r A_\theta$ will be converted into the mechanical angular momentum

$$P_{\theta i} = p_{\theta i} + Q r_i A_{\theta i} = P_{\theta f} = p_{\theta f} \quad (A_{\theta f} = 0) \quad (4.6)$$

where the subscripts i and f stand for the initial and final regions.

In ECRIS the extraction apertures have azimuthal symmetry, with an ion being extracted at a radius r_i with respect to the optical axis, as shown in Figure 4.3. Such an ion has the generalized angular momentum

$$P_{\theta i} = p_{\theta i} + Q r_i A_{\theta i} \quad (4.7)$$

The other important consequence of Eq. (4.4) is that since the magnetic field contributes to the final transverse momentum, it also then contributes to the emittance, as we will now demonstrate. Imagine that we have a group of ions with the same mass M and charge Q , being extracted at the same initial radius $r_i \neq 0$ and having the same initial generalized angular and radial momenta $P_{\theta i}$ and P_{ri} , distributed on a circle of radius r_i , and that there are no collisions among ions during transit. If we trace all these ions from the extraction aperture to a region of zero magnetic field, as is schematically shown in Figure 4.4, we will see all these ions distributed over a circle of radius r_f and having the same mechanical angular and radial momenta. The phase diagrams enclosed by these ions can be given by projecting the radial and the angular velocities and positions of these ions in the cylindrical coordinates into the $X-X'$ and the $Y-Y'$ Cartesian phase planes. For a convenient derivation, v_{rf} and $v_{\theta f}$ are assumed to be positive, and from the following analysis one will see the directions of v_{rf} and $v_{\theta f}$ do not then contribute to the phase space area. The relations between v_{rf} , $v_{\theta f}$ and v_x , v_y are given below

$$v_x = v_{rf} \cos \phi - v_{\theta f} \sin \phi \quad (4.8)$$

$$v_y = v_{rf} \sin \phi + v_{\theta f} \cos \phi \quad (4.9)$$

$$v_x^2 + v_y^2 = v_{rf}^2 + v_{\theta f}^2 \quad (4.10)$$

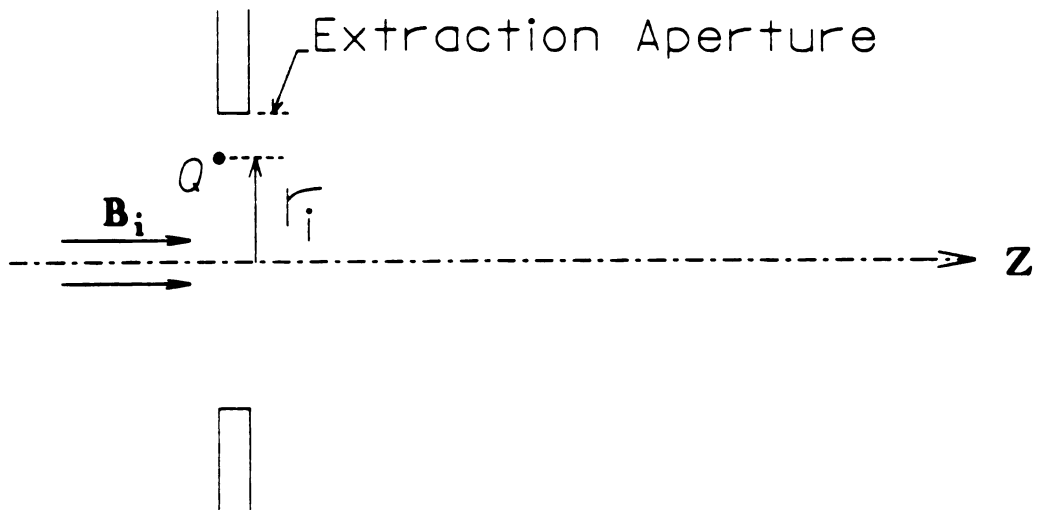


Figure 4.3. The extraction region of an ECRIS with an axial magnetic field. Ions are extracted from the source at radius r_i .

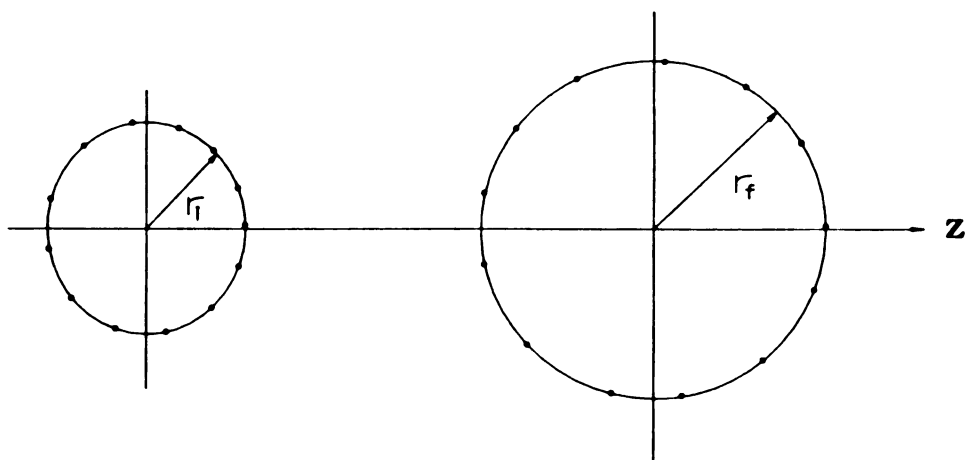


Figure 4.4. Schematic view of a group of identical ions on a circle traveling along the optics axis.

It is obvious that $v_y = 0$ when $v_{x\max} = (v_{rf}^2 + v_{\theta f}^2)^{1/2}$ at a position $X = r_f \cos \phi_x$, while ϕ_x is determined by

$$\phi_x = -\tan^{-1}\left(\frac{v_{\theta f}}{v_{rf}}\right) \quad (4.11)$$

Similarly $v_x = 0$ when $v_{y\max} = (v_{rf}^2 + v_{\theta f}^2)^{1/2}$ at $Y = r_f \sin \phi_y$, and ϕ_y is given by

$$\phi_y = \tan^{-1}\left(\frac{v_{rf}}{v_{\theta f}}\right) \quad (4.12)$$

As Figure 4.5 shows, ion 1 (coincident with X-axis) gives $X_{\max} = r_f$ in the X-X' plane and $Y'_{\text{int}}(Y=0) = \frac{v_{\theta f}}{v_z}$ in the Y-Y' plane. Ion 2 (coincident with Y-axis) gives $Y_{\max} = r_f$ in the Y-Y' plane and $X'_{\text{int}}(X=0) = -\frac{v_{\theta f}}{v_z}$ in the X-X' plane. Ion 3, at a point where the contributions of v_{rf} and $v_{\theta f}$ to v_y cancel each other, that is, where v_x (or $x' = x'_{\max}$) is maximum at this point. Similarly ion 4 gives $v_{y\max}$ ($Y' = Y'_{\max}$). The total projection of all $v_{r\ell}$ and $v_{\theta\ell}$ ($\ell = 1, 2, \dots$) to the X-X' and Y-Y' planes constructs an ellipse in the respective phase planes. Noting that X'_{int} and Y'_{int} are dual value functions of X or Y, namely $X'_{\text{int}} = \pm C1$ and $Y'_{\text{int}} = \pm C2$ ($C1 \geq 0$ and $C2 \geq 0$), $X'_{\text{int}} = C1$ and $Y'_{\text{int}} = C2$ are used to determine the areas enclosed by these ellipses. The areas due to such ellipses in these two planes are then determined as

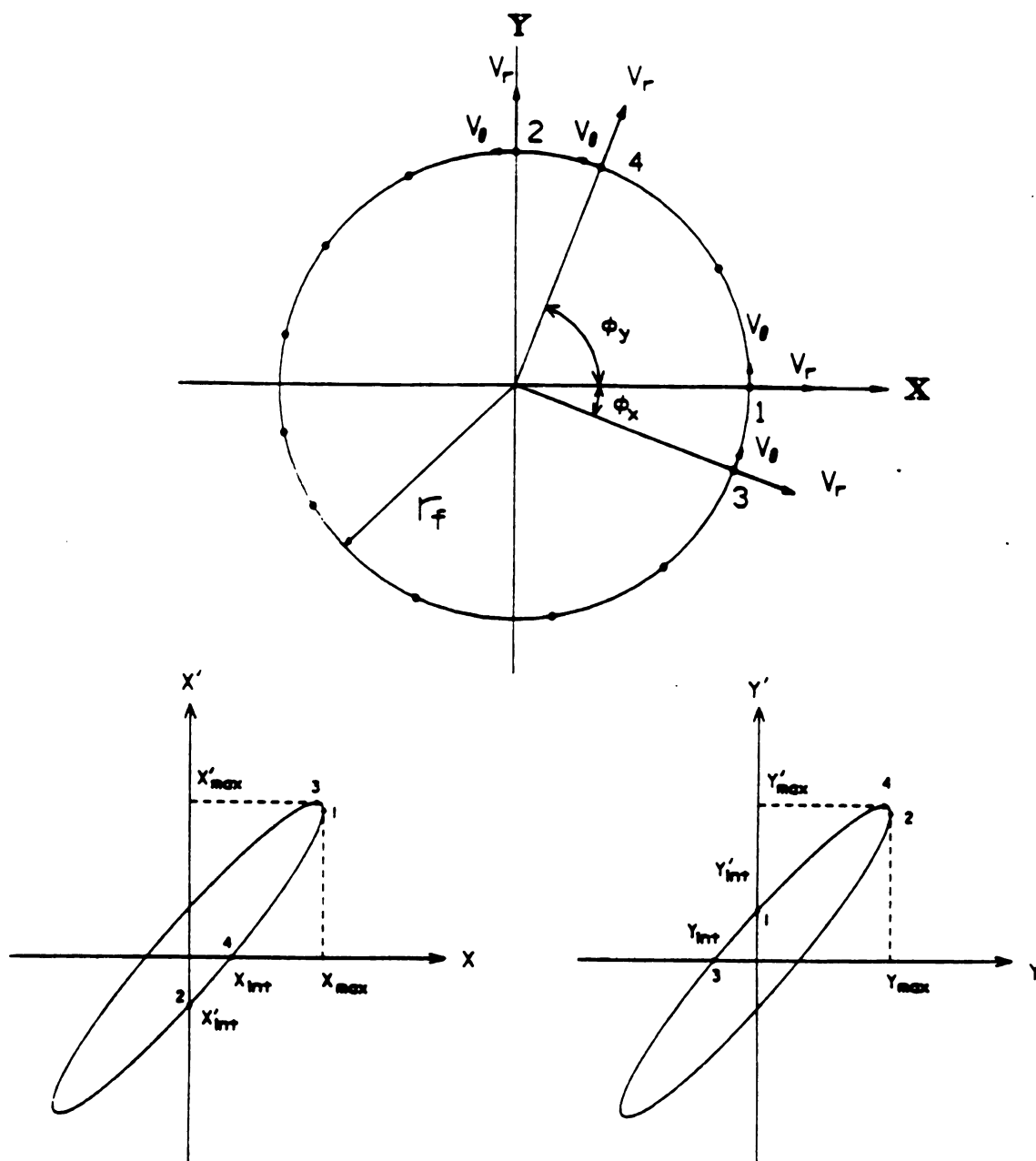


Figure 4.5. The correlation in phase space. Point i in the XX' plane corresponds with point i in the YY' plane.

$$A_{XX'} = \pi X_{\max} X'_{\text{int}} = \pi r_f \left| \frac{Mv_{\theta f}}{Mv_z} \right| = \pi \left| \frac{p_{\theta f}}{p_z} \right| \quad (4.13)$$

$$A_{YY'} = \pi Y_{\max} Y'_{\text{int}} = \pi r_f \left| \frac{Mv_{\theta f}}{Mv_z} \right| = \pi \left| \frac{p_{\theta f}}{p_z} \right| \quad (4.14)$$

We then have the following expressions for the beam emittance due to such group of ions on a circle

$$\epsilon_{XX'} = \epsilon_{YY'} = \left| \frac{p_{\theta f}}{p_z} \right| \quad (4.15)$$

Here we see that the sign of $\frac{p_{\theta f}}{p_z}$ does not affect the phase space areas. $\epsilon_{XX'} = \epsilon_{YY'}$ is the natural result of such azimuthal symmetry of the extraction system.

From the above analysis one can further imagine that a beam consists of many such circular layers; ions have the same momentum within a layer and various momentum among layers. Each layer of ions defines an ellipse with a common center in the X-X' and Y-Y' planes. The total phase area in the X-X' or Y-Y' plane is then normally equal to the area enclosed by the largest ellipse. In some cases the emittance could be larger than this when aberrations distort the ellipse orientations. Thus the beam emittance can be expressed as

$$\epsilon_{\text{beam}} = \{A_i\} / \pi \quad (4.16)$$

where $\{A_i\}$ stands for the total phase area due to all the individual ellipses. If all the remaining ellipses are enclosed by the largest ellipse of $A_{i \max}$, then ϵ reaches its minimum

$$\epsilon_{\min} = A_{i \max} / \pi \quad (4.17)$$

And if the largest ellipse of $A_{i \max}$ is defined by the edge-extracted group of ions, then

$$\epsilon_{\min} = A_{\text{edge}} / \pi \quad (4.18)$$

From the above analysis a conclusion could be drawn here; for any charged particle source with azimuthal symmetry in the extraction system (fields, electrodes), if the edge-extracted particles have the largest initial generalized angular momentum, the minimum emittance is given by

$$\epsilon_{\min} = \left| \frac{P_{\theta \text{ edge}}}{p_z} \right| \quad (4.19)$$

In ECRIS, the edge-extracted ions of the same charge do have the largest generalized momentum, because of the rA_θ term, so that if there is no lens aberration during the extraction, the beam emittance should be no smaller than that described by Eq. (4.19). Comparison of cold ion BEAM_3D calculations with RTECR emittance measurements do closely follow the emittance given in Eq. (4.19), as will be shown.

4.2.2 Effects of Ion Temperature, Magnetic Field and Q/M Ratio on Beam Emittance

Ion-ion collisions are the fastest process in the plasma and should result in thermalization [We82]. Since the thermalization should not have any direction preference, the ion velocities should be isotropic before extraction, and thus the ion thermal velocity will contribute to the beam emittance by increasing the mechanical angular and radial momentum. As indicated by Eq. (4.7), in a field free region, the maximum mechanical angular momentum of the edge-extracted ion is of the form

$$p_{\theta f} = r_a (Mv_{\theta i} + QA_{\theta a}) \quad (4.20)$$

where r_a is the radius of the extraction aperture and $A_{\theta a}$ is the azimuthal vector component at that location. The linear angular velocity $v_{\theta i}$ is the signature of the ion temperature inside the ECRIS. Then the emittance is

$$\epsilon_{\min} = \left| \frac{p_{\theta f}}{p_z} \right| = r_a \left| \frac{Mv_{\theta i} + QA_{\theta a}}{p_z} \right| \quad (4.21)$$

The magnitude of the angular velocity is related to the ion temperature T_i by $v_{\theta i} = (T_i/M)^{1/2}$ and $p_z = (2MQV_{ex})^{1/2}$, hence

$$\epsilon_{\min} = r_a \left[\left(\frac{T_i}{2QV_{ex}} \right)^{1/2} + A_{\theta a} \left(\frac{Q}{2MV_{ex}} \right)^{1/2} \right] \quad (4.22)$$

Eq. (4.22) shows the contribution of the ion temperature to the beam emittance. If the extraction voltage V_{ex} is constant, one can clearly see that:

1. if $(\frac{T_i}{Q})^{1/2} \gg A_{\theta a} (\frac{Q}{M})^{1/2}$, the emittance is dominated by the ion temperature T_i and has the value of

$$\epsilon_{min} \approx r_a \left(\frac{T_i}{2QV_{ex}} \right)^{1/2} \quad (4.23)$$

Thus the higher the ion temperature, the larger beam emittance. The emittance is independent of ion mass M but varies with $Q^{-1/2}$. If $T_i = t_c \text{ eV} \times q$, here t_c is constant, then all ion beams will have the same emittance

$$\epsilon_{min} \approx r_a \left(\frac{t_c}{2V_{ex}} \right)^{1/2} = \text{constant} \quad (4.24)$$

2. if $(\frac{T_i}{Q})^{1/2} \ll A_{\theta a} (\frac{Q}{M})^{1/2}$, the emittance is dominated by the magnetic field and the Q/M ratio, and is given by

$$\epsilon_{min} = r_a A_{\theta a} \left(\frac{Q}{2MV_{ex}} \right)^{1/2} \quad (4.25)$$

Then the higher magnetic field in the source extraction, the larger the emittance. Also an ion beam with a higher Q/M will have a larger emittance.

Otherwise, if $(\frac{T_i}{Q})^{1/2}$ is comparable to $A_{\theta a}(\frac{Q}{M})^{1/2}$, then the ion temperature, magnetic field and Q/M ratio all play important roles in the ECR ion beam emittance, with the emittance is given by Eq. (4.22). The conclusions that increasing magnetic field or increasing ion temperature results in larger emittance still holds, but if the ion temperature and the magnetic field are kept constant, at the case where $(MT_i)^{1/2}/A_{\theta a} = Q$, the emittance will reach a minimum of ϵ_{\min}

$$\epsilon_{\min} = r_a (2A_{\theta a}/V_{ex})^{1/2} (T_i/M)^{1/4} \quad (4.26)$$

Finally if the thermal energy scales with charge ($T_i = t_c \text{ eV} \times q$), one would see that

$$\epsilon_{\min} = r_a \left[\left(\frac{t_c}{2V_{ex}} \right)^{1/2} + A_{\theta a} \left(\frac{Q}{2MV_{ex}} \right)^{1/2} \right] \quad (4.27)$$

Again a stronger magnetic field or the higher Q/M ratio would result in a larger emittance if the other parameters are constant.

The dependence of ion temperature, magnetic field and Q/M on the theoretical emittance for ideal argon beams, assuming the emittance is determined by the edge extracted ions and no extraction aberrations, is numerically calculated and shown in Figures 4.6, 4.7 and 4.8. Figure 4.6 shows, if all the argon ion species have the same temperature, one would obtain a minimum emittance for a particular Q/M if all other parameters are held constant. Figure 4.7 shows this effect for argon ions with an ion temperature expressed as a constant

Ar Beam Emittance of Ideal Beam

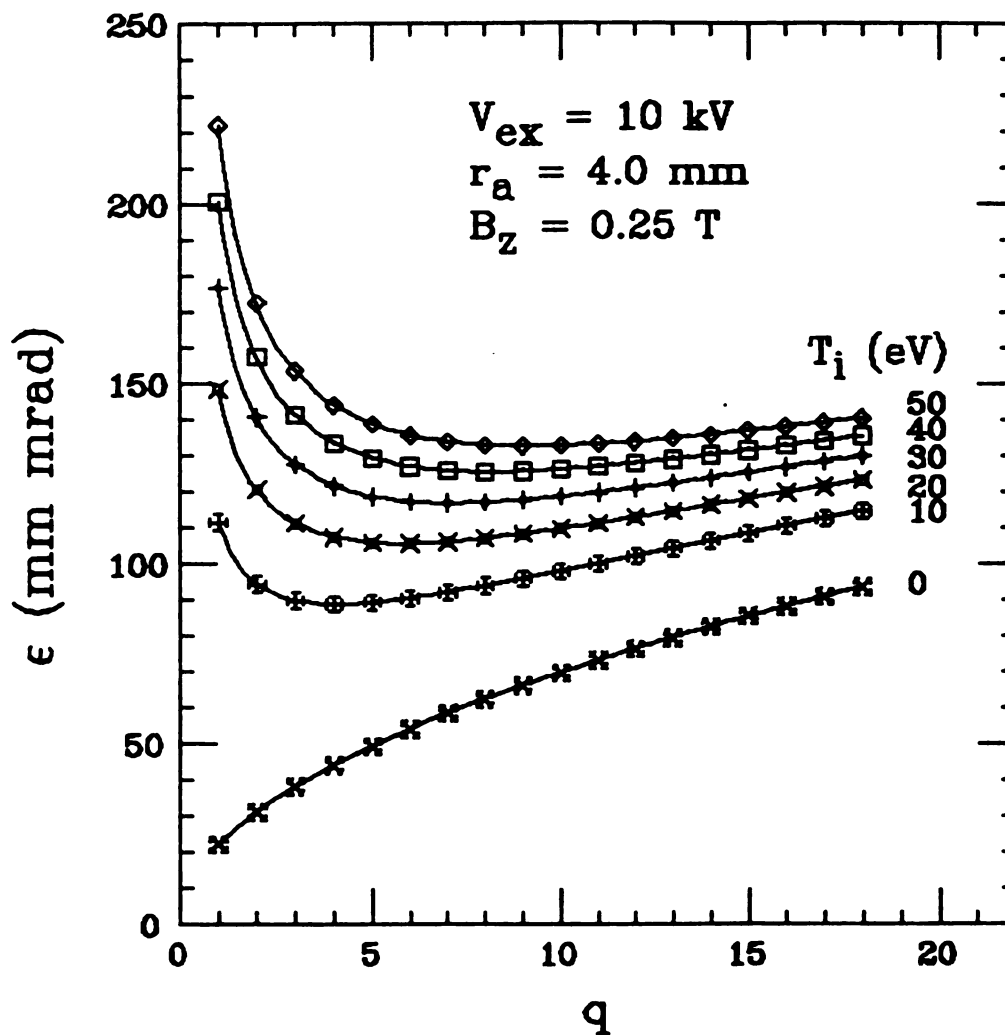


Figure 4.6. The effects of ion temperature on the ideal argon beam emittance as a function of charge-to-mass ratio. Ions are assumed extracted at 10 kV, extraction aperture $r_a = 4$ mm and with $B_z = 0.25$ T (approximately the same conditions as for the RTECR extraction).

Ar Beam Emittance of Ideal Beam

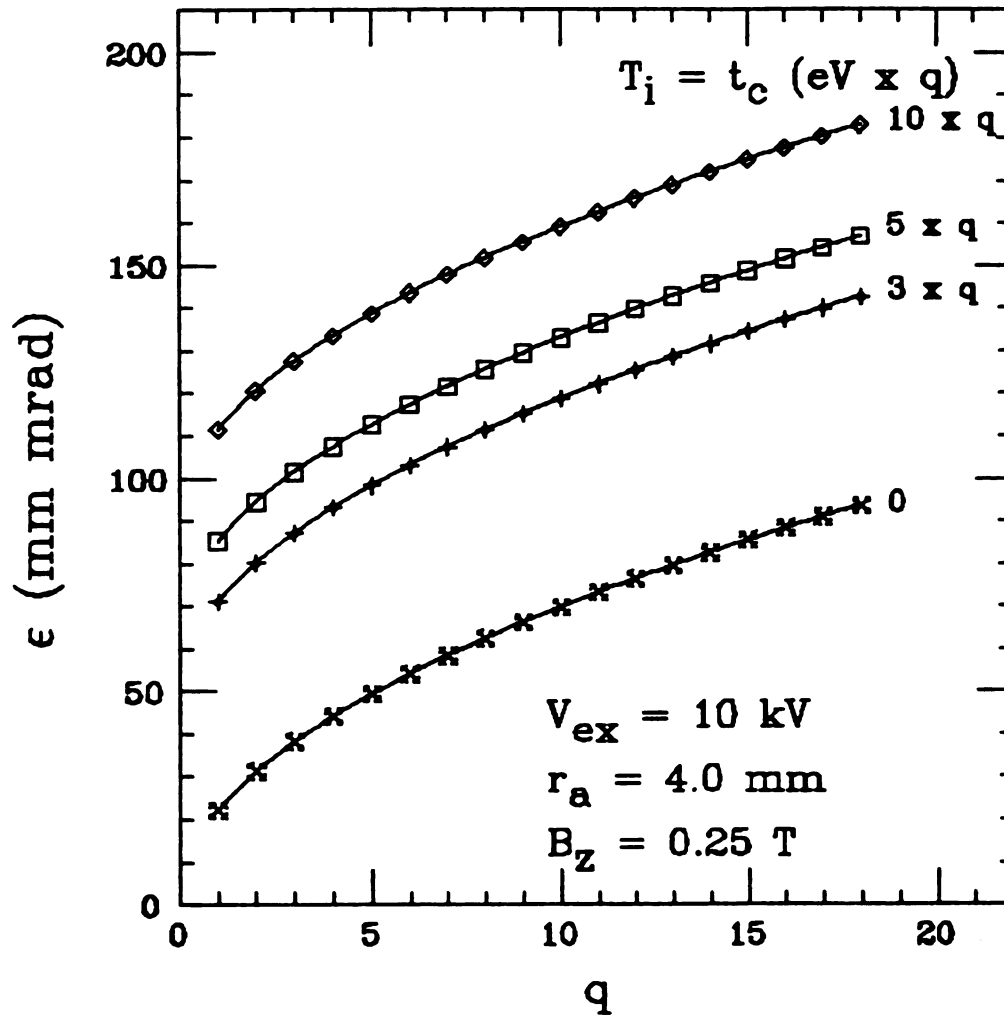


Figure 4.7. Argon beam emittances with the ion temperature taken as $T_i = t_c$ eV x q . Other conditions are the same as in Figure 4.6.

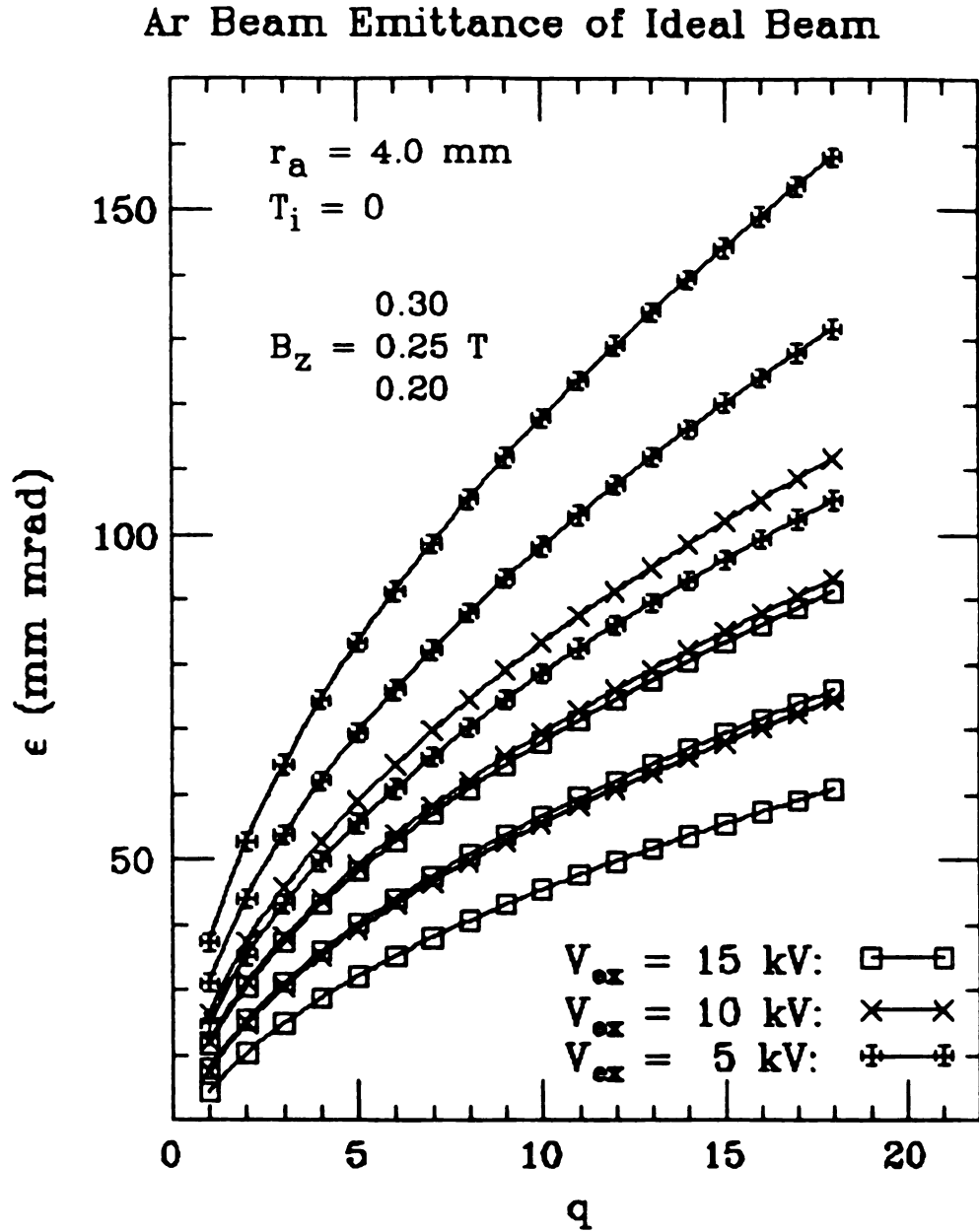


Figure 4.8. Emittances of cold argon beams with different extraction voltages and various extraction magnetic fields. The extraction aperture is $r_a = 4$ mm.

times $\text{eV} \times q$. A maximum emittance of about 200 mm mrad occurs for argon 18+ for an ion temperature equal to $T_i = 10 \text{ eV} \times q$. Figure 4.8 shows the case of zero ion temperature, equivalent to the hard edge model [De83, Ha87]. In this case the magnetic field determines the emittances, and further the ions with higher Q/M will have larger emittances. Argon 18+ has the maximum emittance of about 100 mm mrad for the specified conditions (extracted at 10 kV) in Figure 4.8. The ion temperature in ECRIS is in the order of a few $\text{eV} \times q$ [Me86, An88], and based on the above arguments, we could draw a theoretical conclusion that the maximum emittance should be about 200 mm mrad for ECR ion beams extracted at 10 kV, for an aperture radius of 4 mm and a magnetic field of 0.25 T.

4.2.3 Extraction Electrode Design

In ECRIS, the first electrode is generally designed by following Pierce's design theory [Pi54], which was originally developed for electron guns. It is based on the following assumptions: (1.) zero magnetic field; (2.) zero thermal energy; (3.) conservative electric field; (4.) electrons uniformly emitted from a planar cathode. Following Pierce, one solves the POISSON equation with the full space charge taken into consideration, which yields the following solutions for a rectilinear beam, with a parallel beam profile, in an accelerating gap.

Inside the beam:

$$V_{in} = Az^{4/3} \quad (4.28)$$

while outside the beam:

$$V_{\text{out}} = A (z^2 + y^2)^{2/3} \cos\left(\frac{4}{3} \tan^{-1} \frac{y}{z}\right) \quad (4.29)$$

with

$$A = \left[\frac{9J}{4\epsilon_0 (2e/m)^{1/2}} \right]^{2/3} \quad (4.30)$$

where z is the optic axis, J is the current density, e and m are the electron charge and mass. Eqs. (4.28) and (4.29) are subject to boundary conditions $V = 0$ at $z = 0$ and $dV/dz = 0$ at $z = 0$.

The condition $V_{\text{out}} = 0$ at $z = 0$ gives the shape of the first electrode, which requires the electrode has an angle of 67.5° with respect to the z axis. $V_{\text{out}} = V_{\text{ex}}$ at $z = D$ gives the shape of the second electrode. Such electrode shapes and the equipotential lines for a rectilinear beam is shown in Figure 4.9. Finally, at $z = D$ we have $V_{\text{in}} = V_{\text{ex}} = AD^{4/3}$, and rearrangement yields the limiting value of nonrelativistic current density flow

$$J_{\text{max}} = \frac{4\epsilon_0 (2e/m)^{1/2} V_{\text{ex}}^{3/2}}{9D^2} \quad (4.31)$$

which is the so called Child-Langmuir Law for the space charge limited emission [Ch11]. If the current available is less than this maximum current, then a converging beam profile will result in the transit of the gap. In the case of a cylindrical beam flow, where $\frac{\partial V}{\partial r} = 0$ within the beam in the extraction gap is required, solutions of the POISSON

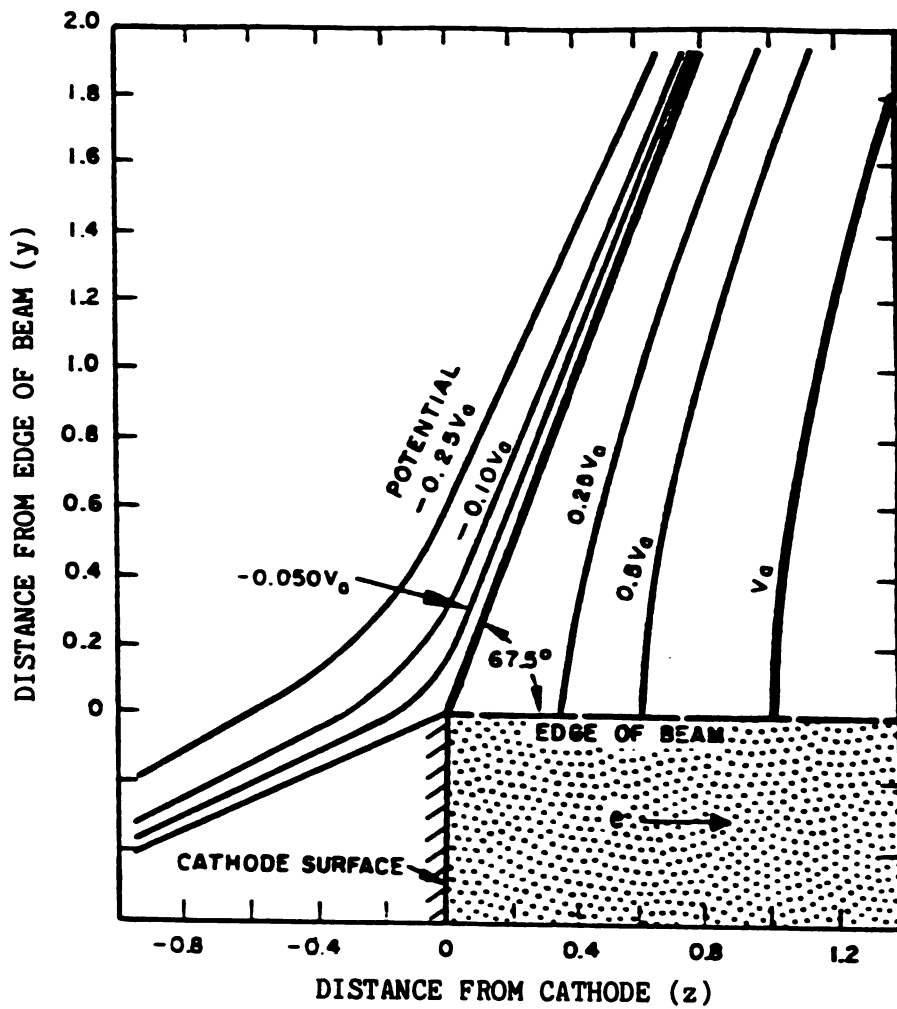


Figure 4.9. Plot of the electrode shapes (heavy lines) and the equipotential lines external to a planar space-charge-limited electron beam as determined from Eq. (4.29) [Pi54].

equation can only be numerically obtained, but the results are very similar to the case of a rectilinear beam. According to Pierce, the first electrode still makes an angle of 67.5° with respect to the optical axis, while the puller has a spherical face, as Figure 4.10 shows.

For positive ion beams, the above arguments hold except for a reversal of the extraction electric field direction, and changing e to Q and m to M . For a beam of multiple ion species, in which it is assumed that every ion species is uniformly distributed, the Pierce constant A is then of the form

$$A = \left[\frac{9}{4\epsilon_0 2^{1/2}} \sum \frac{J_i}{(Q_i/M_i)^{1/2}} \right]^{2/3} \quad (4.32)$$

where J_i is the contribution of the i -th ion species of charge Q_i and mass M_i . The space charge limit current density is then replaced by the following expression

$$\sum \frac{J_i}{(Q_i/M_i)^{1/2}} = \frac{4\epsilon_0 2^{1/2} V_{ex}^{3/2}}{9D^2} \quad (4.33)$$

This would be the equivalent Child-Langmuir Law for an ion beam of multiple ion species.

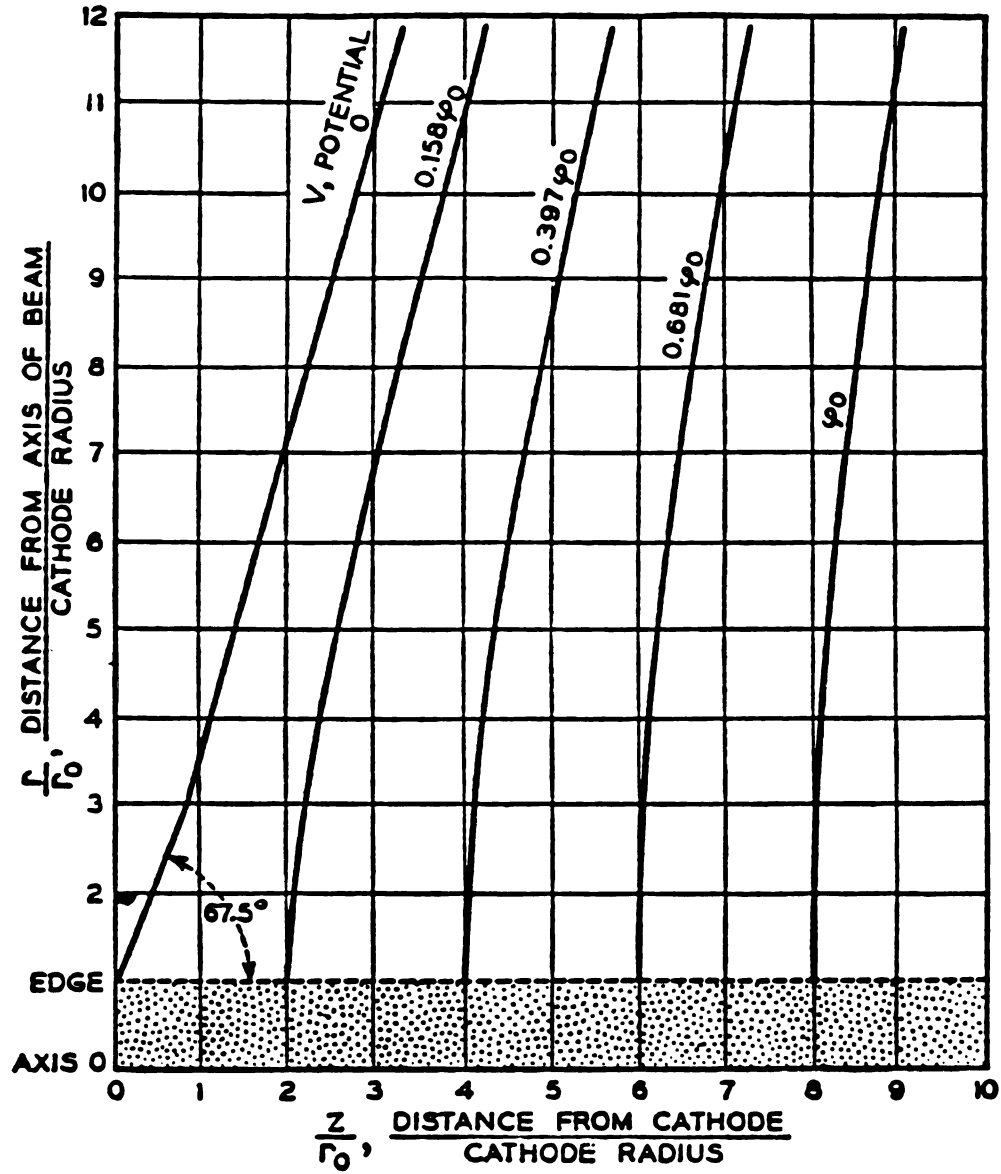


Figure 4.10. Electrodes for obtaining axially symmetrical electron flow of uniform diameter [Pi54].

4.3 BEAM_3D Predictions on the Extraction Electrode Design

The RTECR source has a three-piece electrode system, as shown in Figure 4.2. For historical reasons, the original puller electrode in the RTECR had a 45° angle, while the first electrode following the Pierce's theory is at a 67.5° angle with respect to the optic axis as shown in Figure 4.2A. A comparison of the electric field geometry between the 45° and Pierce spherical pullers is shown in Figure 4.11, in which the term "M2a" denotes the 45° puller. It is seen that, compared to the Pierce puller, the axial and radial electric fields of the 45° puller are weaker at the extraction aperture and very strong at the aperture of the puller. BEAM_3D calculations have suggested that such an extraction system with a 45° puller does not work properly when the extracted current is at or below the space charge limited current. It has less focussing strength at the beginning of the extraction, and too much at the end, resulting in a drum shape beam profile in the first gap as shown in Figure 4.12A. A distortion in the phase area after extraction results in a large initial emittance, as shown in Figure 4.13. BEAM_3D suggests that an exact Pierce spherical puller, shown in Figure 4.2B, is better than the 45° puller in ensuring a space charge limited current with a parallel beam profile in the extraction region, as shown in Figure 4.12B, and less phase area distortion after extraction, see Figure 4.13. Therefore a better matching of the downstream beamline should result since the beam brightness is inversely proportional to the square of the effective beam emittance.

Having demonstrated theoretically that a Pierce geometry is better (smaller initial emittance), the first of two consequences will

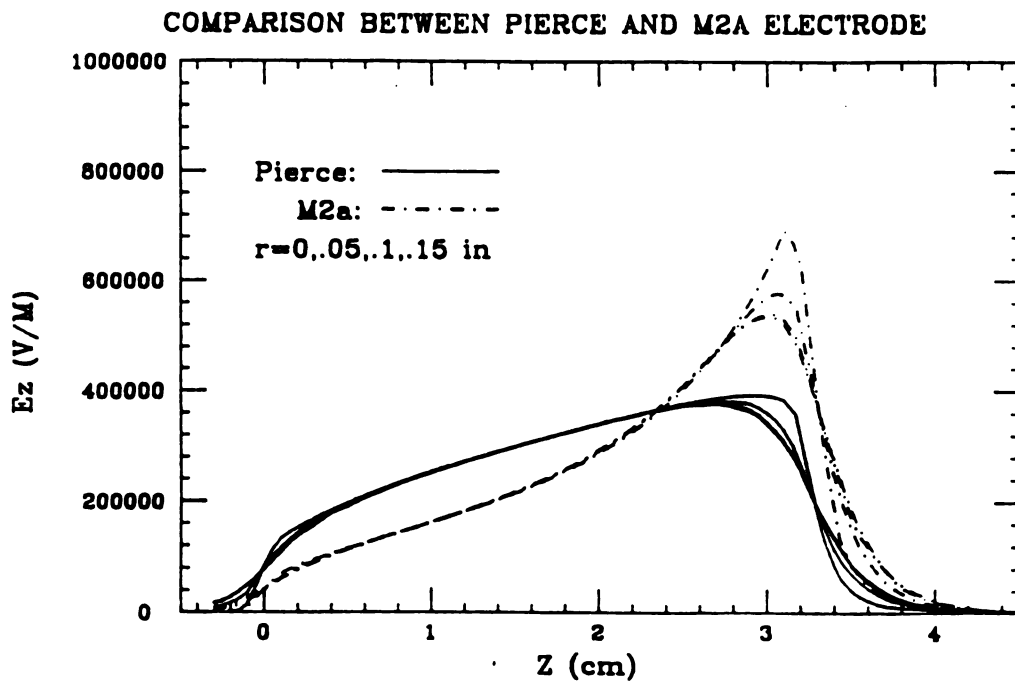
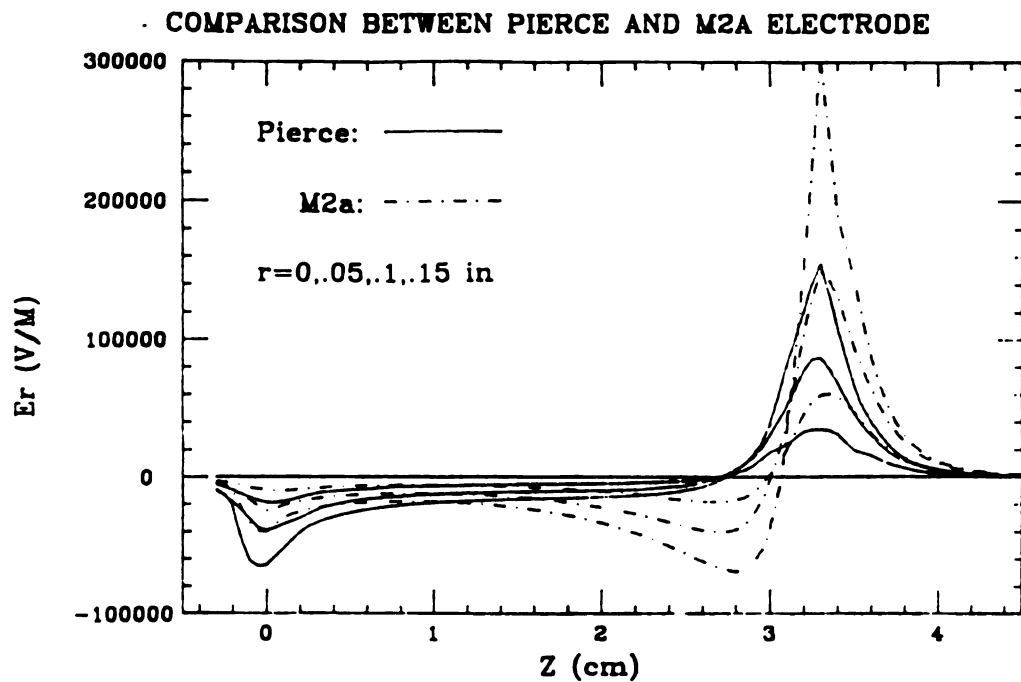


Figure 4.11. A comparison the axial and electric field strengths of 45° (denoted by "M2a") and a Pierce spherical pullers. In both cases the extraction gap is 3.3 cm and the first electrodes are the same.

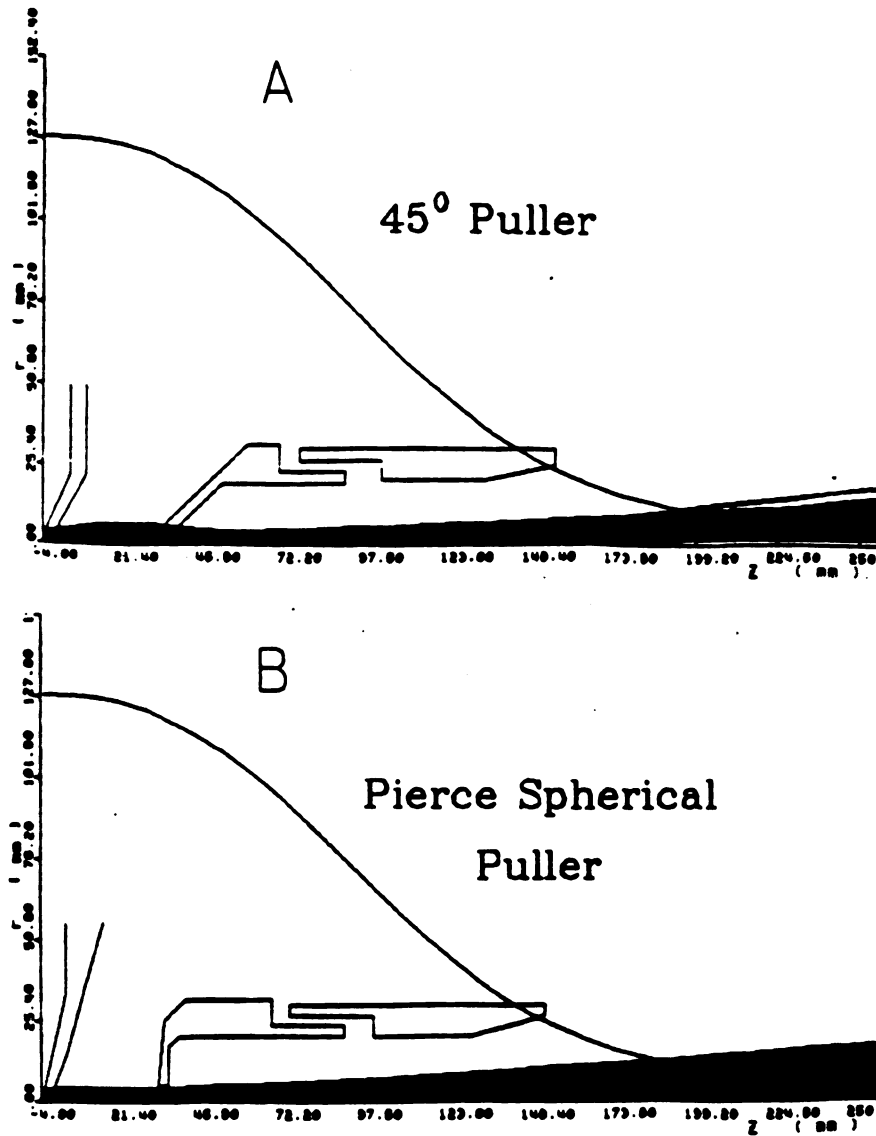
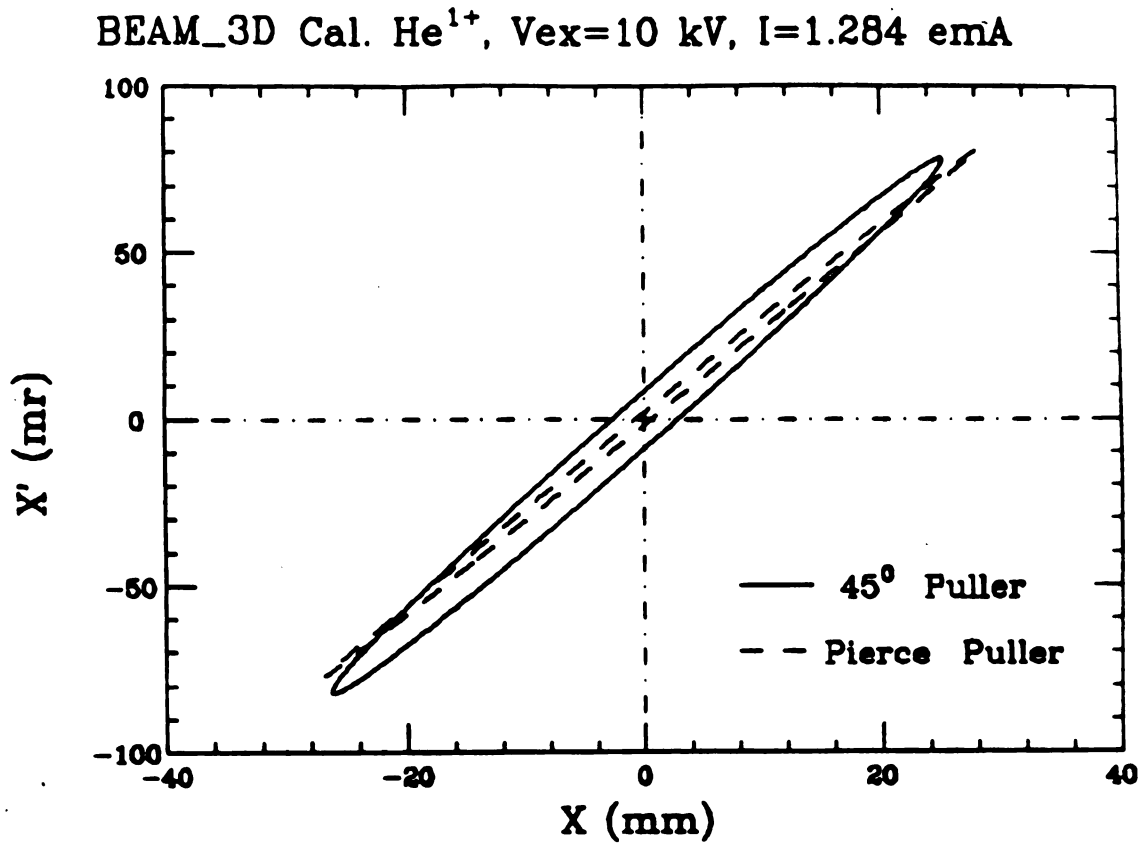


Figure 4.12. BEAM_3D calculated beam profiles at a space charge limited current for the extraction system with a 45° angle on the puller electrode face and a Pierce spherical puller. A drum shape in the first gap, and a focus in the puller electrode are seen for the 45° puller of Figure 4.2A.



$$\phi = 8 \text{ mm}, T_{t0} = 0, D = 3.3 \text{ cm}, Z = 41 \text{ cm}$$

Figure 4.13. A comparison of the effective emittance after extraction for the 45° and a Pierce spherical pullers in the RTECR, for a space charge limited He^{1+} beam of 1.3 emA at $D = 3.3$ cm, with $V_{\text{ex}} = 10$ kV. BEAM_3D predicts the effective emittance of the 45° puller is about three times that of the Pierce spherical puller.

be noted here (the other will be discussed in Chapter 5). It concerns the adjustment of the Pierce extraction geometry. Figure 4.14 shows the dependence of total helium 1+ current extracted from the RTECR, for 3 different main stage operating pressures [An88]. For these measurements, the source aperture was 8 mm, the extraction gap was 3.3 cm and the puller voltage was zero. The total extracted current is seen to follow the Child-Langmuir limit (labelled theory) up to a saturation voltage, and the saturation voltage is seen to increase with main stage pressure. Along the line labelled $D = 3.3$ cm, a parallel beam will be produced in transit of the first gap (as shown in Figure 4.12B). To the right of the theory line, a gap of 3.3 cm will result in excess focussing in first gap and therefore higher divergence after extraction. This high divergence will result in a large beam envelope inside the focussing solenoid, and the solenoid spherical aberration will become very severe (this will be discussed in more detail in Chapter 5), and therefore poor beam transport results.

4.4 Results

In matching ECRIS beams to accelerators, the source tune is set by the ion production requirements, and the extraction voltage is set by the injection rigidity. So for example, we might find it necessary to operate the source on the lower pressure current curve of Figure 4.14 at a net extraction voltage of 10 kV. In that case, to minimize the divergence after extraction, we must decrease the electric field strength in the first gap, by increasing the gap ($D = 5$ cm line) or reducing the voltage ($\Delta V_p = 5$ kV).

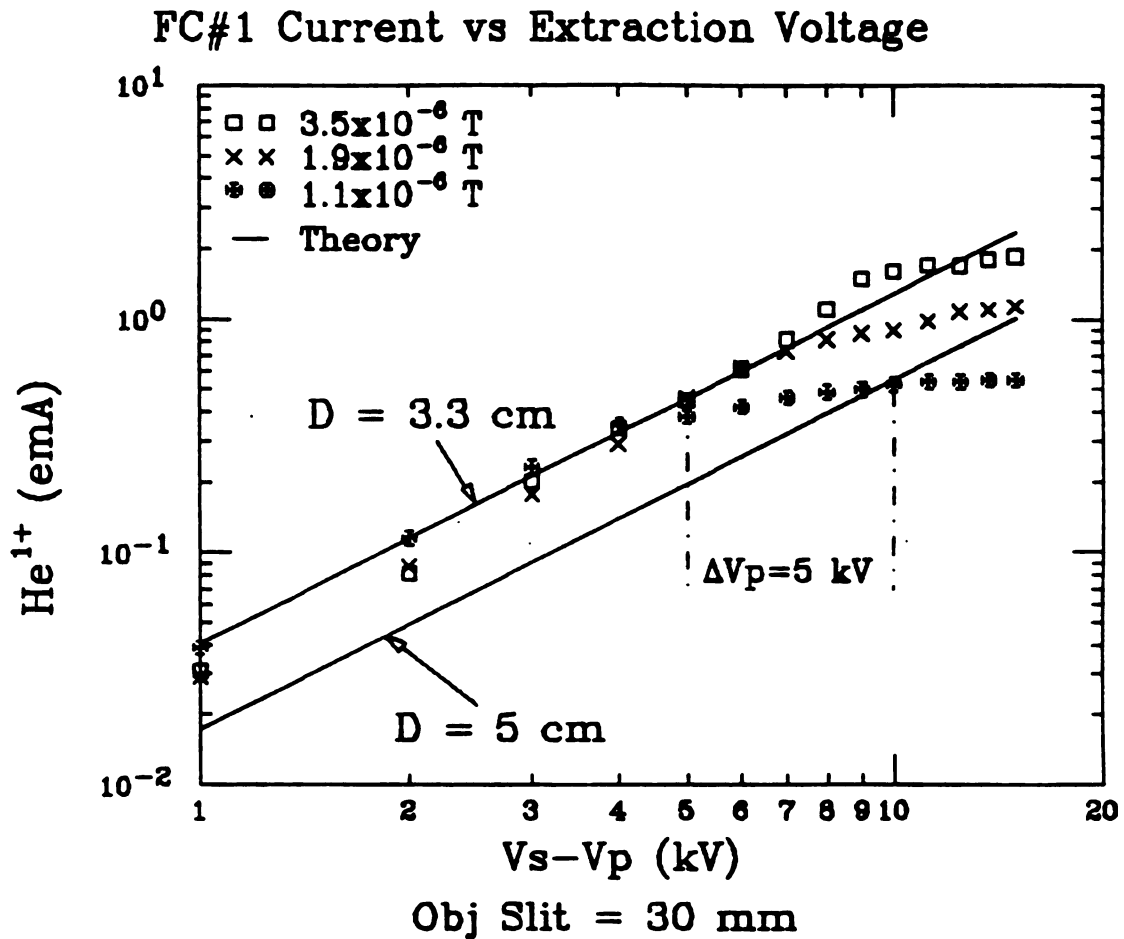
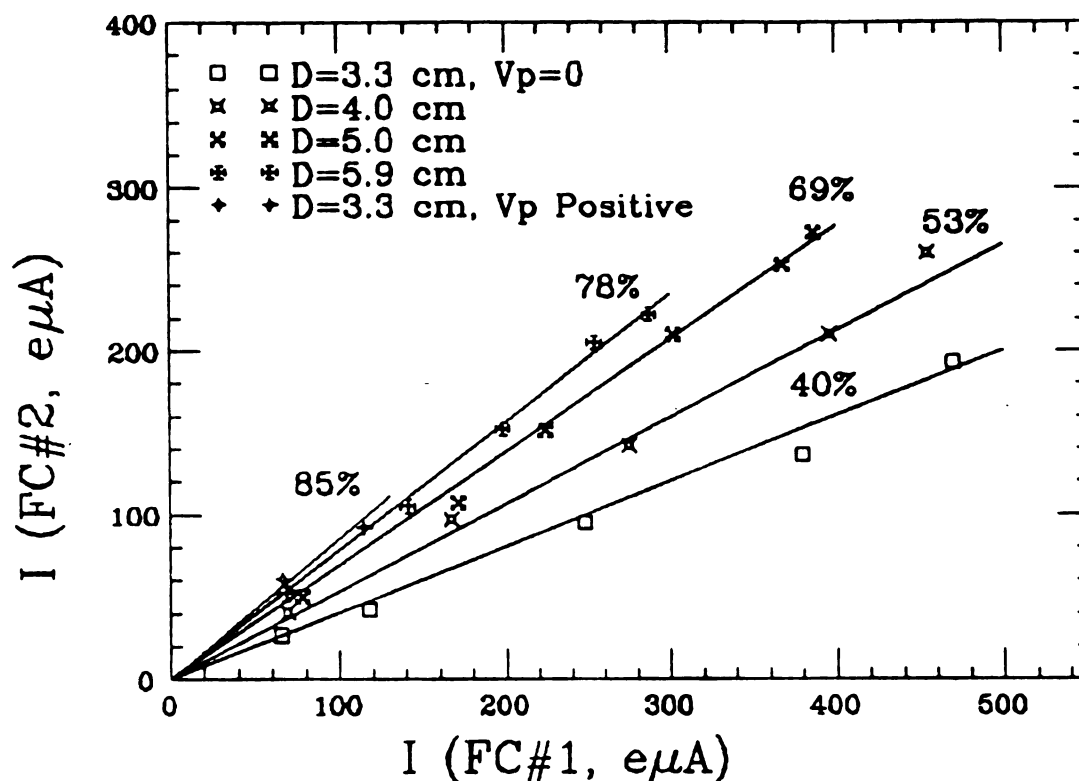


Figure 4.14. Using the He^{1+} technique, the total extracted current of the RTECR was measured directly at FC#1 as a function of extraction voltage, for 3 operating pressures. At low voltages, the extracted current is space charge limited, following the Child-Langmuir law (marked Theory). At higher voltages the extracted current is seen to saturate.

To do this properly, one should know when the extracted current is space charge limited. This can be achieved operationally by making the gap and puller voltage tuning parameters. For the RTECR injection into the cyclotrons at NSCL, we have in fact generally operated to the right of the $D = 3.3$ cm line. Since this was the maximum design gap, the least over-focussing would occur at $V_p = 0$ ($V_p > 0$ was not a possibility), which is exactly how the system did operate. Once we realized this limit, the first gap was modified to work over the range of 3 to 6 cm. This modified extraction system works better than the old one in better matching the following beamline and the 90° magnet, as an increase in transmission of the analysis magnet is observed. Shown in Figure 4.15, are the transmission measurements from FC#1 to FC#2 versus the extraction gap for a helium $1+$ beam of intensities ($I \leq 0.5$ emA) extracted at 10 kV with zero voltage on the puller (below space charge limited extraction), or a positive voltage on the puller ($D = 3.3$ cm, at space charge limited extraction). It can be clearly seen that, for this current range, space charge limited extraction gives the best transmission, which we learned theoretically also has the smallest divergence and emittance after extraction. When the total extracted current is below that for a space charge limited extraction, the larger extraction gap gives an extraction closer to the space charge limit thus has also smaller divergence after extraction, and better matching to the beamline therefore results.

Transmission Study on the 1st 90° Dipole



He¹⁺, Obj. Slit=15 mm, Ima. Slit=25 mm, Vex=10 kV

Obj. and Image slit Bias: -100 V

Figure 4.15. A transmission study on the analysis magnet for different extraction gaps and helium 1+ currents ≤ 0.5 emA. A beam extracted at the space charge limited gives the best transmission, with decreasing transmission as the beam intensity falls increasingly below the space charge limit.

Chapter 5

Space Charge Force and Pre-analysis Beam Transport

5.1 Space Charge Force

Typical extracted currents from ECRIS are in the range of 1~2 emA for extraction voltages of 5~30 kV, which in turn are set by the injection requirements of accelerators or research. The energies of ion beams extracted from ECRIS are then 5~30 keV $\times q$ -- ion motion is nonrelativistic. Low beam energy coupled with high beam intensity will result in beam growth, if the space charge is not compensated. The space charge force will exert a relevant influence on the ECRIS beam transmission, especially when this force is very strong.

For a beam with rotational symmetry, the space charge force does not have an angular component, thus it has no effect on the ion angular momentum. As indicated by Eqs. (4.3) and (4.4), the space charge force affects only the radial velocity, and hence the beam maximum divergence, as will be demonstrated in the following discussion.

As mentioned in Chapter 2, the space charge force for a rotationally symmetric beam of multiple ion species uniformly distributed is of the form

$$E_r = \frac{1}{2\pi\epsilon_0 r} \sum \frac{I_i}{v_{zi}} \quad (5.1)$$

In a drift region after extraction, an ion on the outmost surface of a beam consisting of multiple ion species, experiences a radial force of (in cylindrical coordinates),

$$\dot{p}_r = \frac{p_\theta^2}{Mr^3} + \frac{Q}{2\pi\epsilon_0 r} \int \frac{I_i}{v_{zi}} \quad (5.2)$$

where p_θ is the mechanical angular momentum, a constant of motion, and r is the radius of the beam. As indicated by Eq. (4.3), the first term originates from the initial canonical angular momentum after extraction from the source, while the second term is the radial space charge force in Eq. (5.1). Rearrangement of Eq. (5.2) yields

$$\ddot{r} = \frac{p_\theta^2}{M^2 r^3} + \frac{Q}{2\pi M \epsilon_0 r} \int \frac{I_i}{v_{zi}} \quad (5.3)$$

Integrating Eq. (5.3) once with respect to the time t gives the radial velocity v_r equation

$$v_r = \left[\frac{p_\theta^2}{M^2} \left(\frac{1}{r_m^2} - \frac{1}{r^2} \right) + \frac{Q}{\pi M \epsilon_0} \ln\left(\frac{r}{r_m}\right) \int \frac{I_i}{v_{zi}} \right]^{1/2} \quad (5.4)$$

where r_m is the radius of the beam where $v_r = 0$.

Recalling the angular velocity is $v_\theta = \frac{p_\theta}{Mr}$, one finds the maximum transverse divergence α_t by dividing $v_t = (v_r^2 + v_\theta^2)^{1/2}$ by the axial velocity v_z of the ion in question

$$\alpha_t = \frac{v_t}{v_z} = \left[\frac{p_\theta^2}{M^2 v_z^2 r_m^2} + \frac{Q}{\pi M \epsilon_0 v_z^2} \ln\left(\frac{r}{r_m}\right) \left[\frac{I_i}{v_{zi}} \right]^{1/2} \right]^{1/2} \quad (5.5)$$

Eq. (5.5) clearly indicates that particles on the beam surface will have a constant maximum transverse velocity, and a constant maximum divergence, if the space charge force is zero since P_θ after extraction is constant. This is precisely the condition that is assumed in beam transport calculations when one omits the space charge force. Otherwise α_t is a function of r , which we will show is a function of the axial drift distance z . Thus α_t will be a function of z , that is, the maximum divergence of the beam changes along the optic axis if the space charge is not fully compensated.

The beam profile is obtained by integrating Eq. (5.4) once more with respect to the time t

$$\int_{r_m}^r \left[\frac{p_\theta^2}{M^2} \left(\frac{1}{r_m^2} - \frac{1}{r^2} \right) + \frac{Q}{\pi M \epsilon_0} \ln\left(\frac{r}{r_m}\right) \left[\frac{I_i}{v_{zi}} \right]^{-1/2} \right] dr = t \quad (5.6)$$

here $t = \frac{\Delta z}{v_{zi}}$ is simply the time that it takes the i -th ions to travel from r_m to r , assuming $t = 0$ at $r = r_m$. There exists no analytical solution for the left side of Eq. (5.6), but numerical integration techniques can be used to give a reasonable result.

To get a feel for the nature of Eq. (5.6) we can formulate an approximate solution. Let $r = r_m + X$ and assume X is small (i.e. a short drift). Then we have

$$\begin{aligned}
& \frac{p_{\theta}^2}{M^2} \left(\frac{1}{r_m^2} - \frac{1}{r^2} \right) + \frac{Q}{\pi M \epsilon_0} \ln \left(\frac{r}{r_m} \right) \int \frac{I_i}{v_{zi}} \\
& \approx \left[\frac{2p_{\theta}^2}{M^2 r_m^3} + \frac{Q}{\pi M \epsilon_0 r_m} \int \frac{I_i}{v_{zi}} \right] x \quad (5.7)
\end{aligned}$$

and Eq. (5.6) becomes

$$t = \left[\frac{2p_{\theta}^2}{M^2 r_m^3} + \frac{Q}{\pi M \epsilon_0 r_m} \int \frac{I_i}{v_{zi}} \right]^{-1/2} \int_0^x dx' / x'^{1/2} \quad (5.8)$$

Performing the integration and re-arranging terms yields

$$r - r_m = \frac{1}{4} \left[\frac{2p_{\theta}^2}{M^2 r_m^3} + \frac{Q}{\pi M \epsilon_0 r_m} \int \frac{I_i}{v_{zi}} \right] \frac{z^2}{v_{zi}^2} \quad (5.9)$$

The beam envelope is seen to have a quadratic dependence on z , with two terms, one due to the initial momentum of the edge particle and the other arising from the space charge force.

For unneutralized ECRIS beams, we will now show that the second term dominates. We have solved equations (5.5) and (5.6) numerically for a helium 1+ beams of 10 keV energy and of various intensities after a waist, and plot these results in Figures 5.1 and 5.2. At zero intensity, Figure 5.1 shows that the maximum divergence is independent of the drift distance, and Figure 5.2 shows that a slow increase in the beam radius with the drift distance will be observed. As the intensity increases both the maximum divergence and beam radius sharply increase with the drift distance. An unneutralized 1.0 emA

$V_{ex}=10$ KV, $V_p=0$ KV, $R_m=4.$ mm, $R_a=4.$ mm, $B_z=.251$ T, He^{1+}

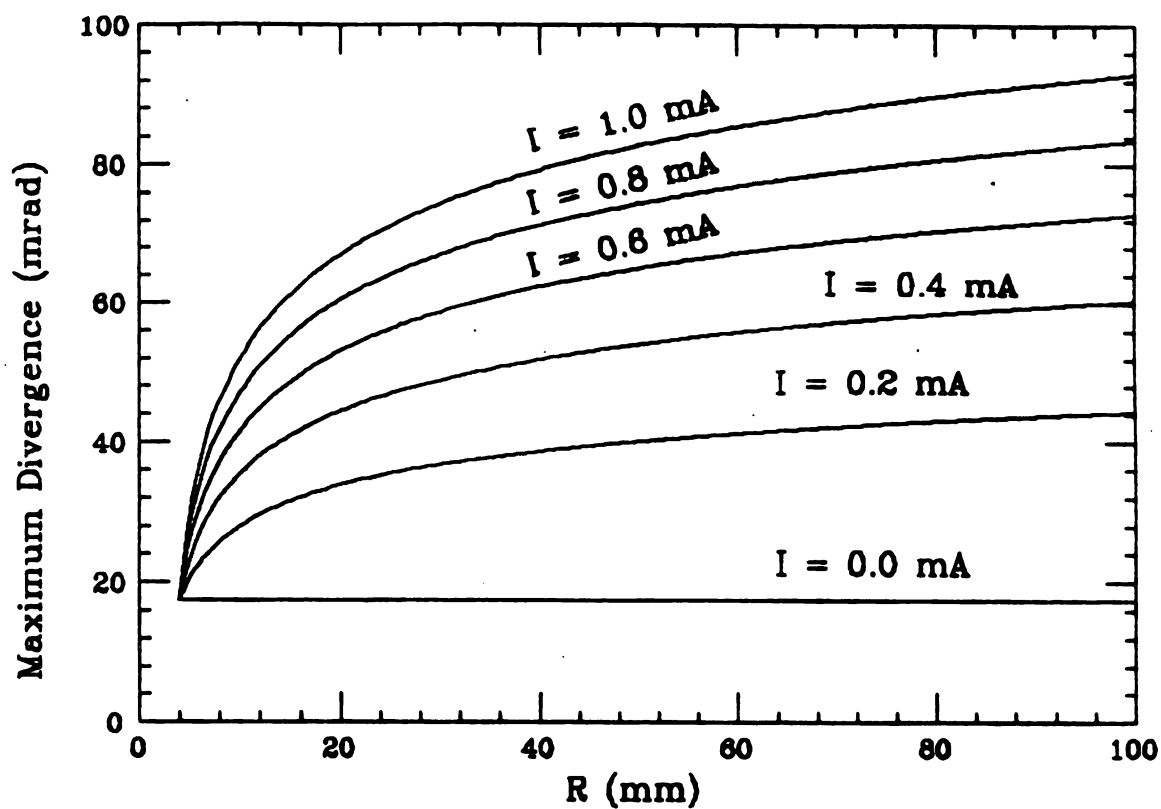


Figure 5.1. He^{1+} beam maximum divergence versus the beam edge radius, for different beam intensities, after a waist. The maximum divergence is a constant if the space charge is zero. But as can be seen, if the space charge force is taken into account, the beam maximum divergence will increase rapidly with the level of the space charge force.

$V_{ex}=10$ KV, $V_p=0$ KV, $R_m=4.$ mm, $R_a=4.$ mm, $B_z=.251$ T, He1+

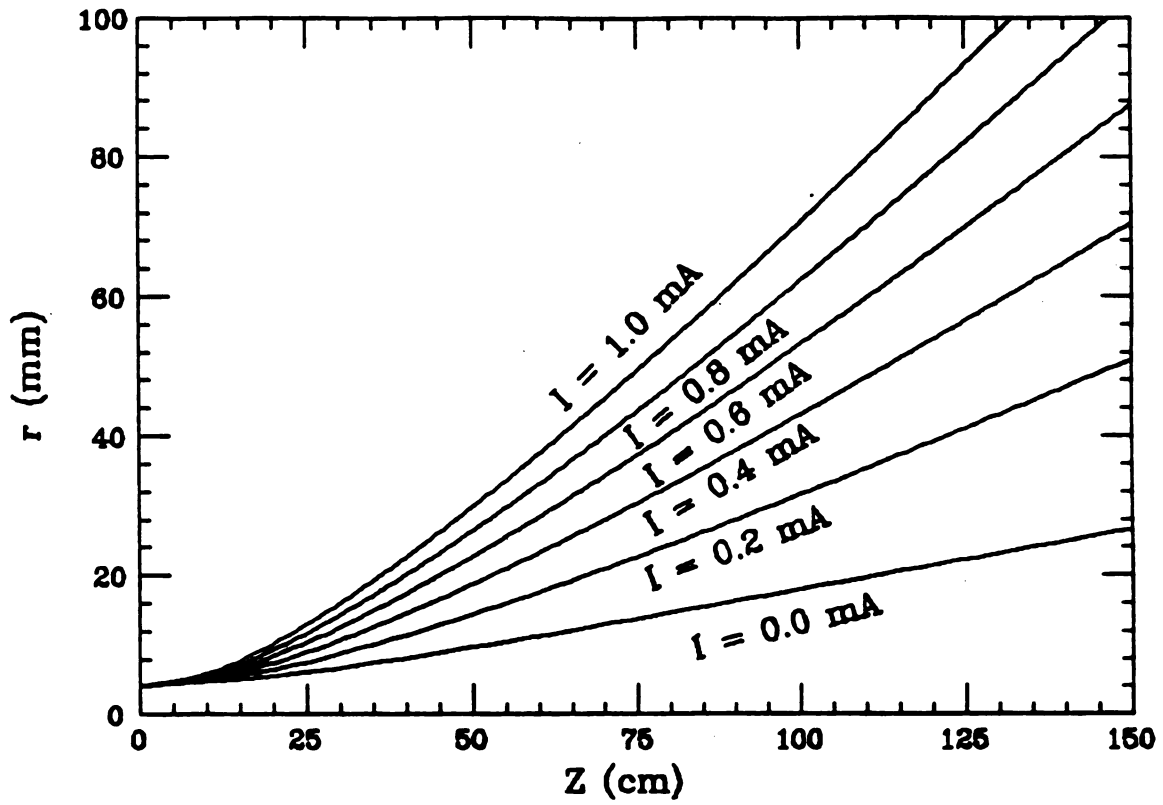


Figure 5.2. A comparison of the beam edge radius with axial drift distance for various levels of the space charge. The starting conditions are the same as in Figure 5.1. For high uncompensated space charge, the beam envelope rapidly increases with axial drift.

helium 1+ beam will have an envelope radius 4 times the zero space charge radius after a drift of only 1 M. That is an enormous effect. In the RTECR analysis system, the distance from the extraction electrode to the solenoid center, and the distance from FC#1 to the 90° magnet entrance are both of the order of 1 M.

In the case of no space charge force, the beam maximum divergence is a constant and so is $X_{int} = r_m$, that is

$$\epsilon(\text{no sp}) = X'_{\max} X_{int} = X'_{int} X_{\max} = \left| \frac{p_{\theta}}{p_z} \right| = \text{constant}. \quad (5.10)$$

In the case of nonzero space charge force, both the X'_{\max} and X_{int} are no longer constants, and noting that $X_{\max} = r$ and $X'_{int} = \left| \frac{v_{\theta} r}{v_z} \right| = \left| \frac{p_{\theta}}{p_z r} \right|$, the product of X_{\max} and X'_{int}

$$\epsilon(\text{sp}) = X'_{int} X_{\max} = X'_{\max} X_{int} = \left| \frac{p_{\theta}}{p_z} \right| = \epsilon(\text{no sp}) \quad (5.11)$$

is also a constant and equal to the emittance with no space charge force. That means the space charge force does not contribute to the beam emittance. A rigorous proof that the space charge force does not contribute to the beam emittance is given by L. Mills and A. M. Sessler for more general cases [Mi58]. Although the space charge force does not contribute to the beam emittance, compared to the case of no space charge force, it increases both the maximum beam divergence and the beam envelope along the beam optical axis, and this effect is illustrated in Figure 5.3 (the effective emittance can be

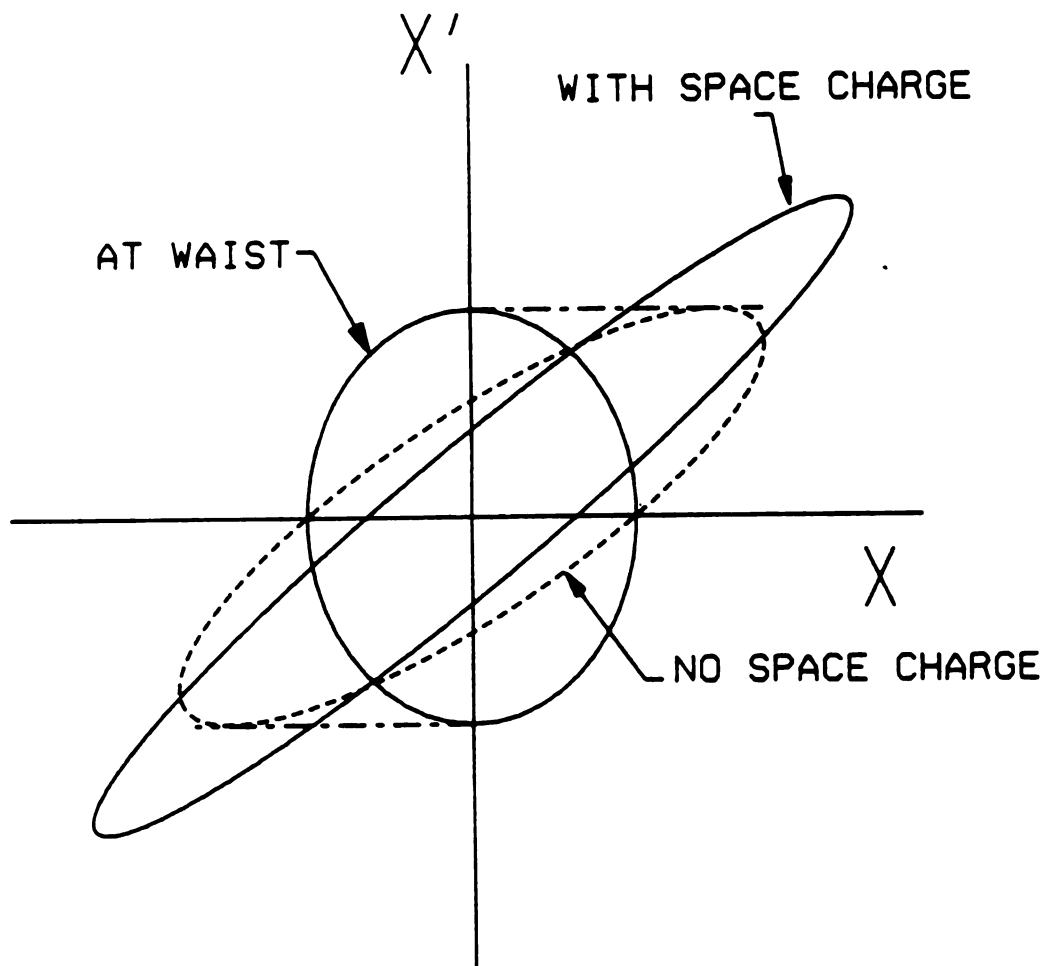


Figure 5.3. A schematic view of the evolution of the emittance envelope after a waist with and without space charge force. The emittance is the same for both cases, but with space charge the maximum divergence and beam size significantly increase.

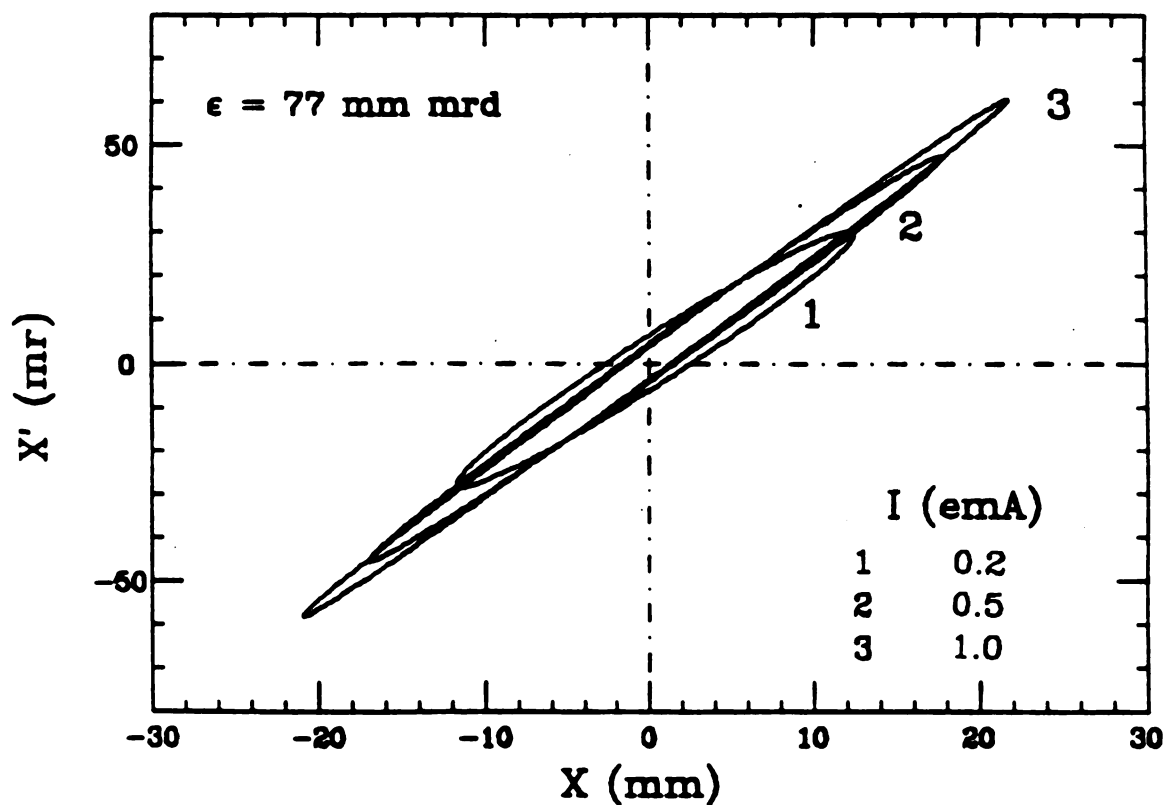
increased by the indirect effect of space charge causing aberration distortions).

We note here another important consequence for the emittance after extraction from a Pierce geometry for high, but still space charge limited currents. Even if a parallel beam is obtained in a Pierce - 1st extraction gap, the divergence after transit of the extraction electrodes will increase with increasing intensity. In Figure 5.4, BEAM_3D emittance calculations for helium 1+ beams are compared for these different intensities; in all 3 cases the first gap was $D = 5$ cm; V_{ex} (end plate) = 10 kV, and the voltage on the puller is varied to ensure a space charge limited current. The starting thermal energy is taken to be zero. In each case the emittance after extraction is 77 mm mrad, but the divergence increases with increasing intensity as a result of the radial space charge force. This is a pure space charge effect -- mitigated only if there is some degree of neutralization in the initial beam. The 1 emA case in Figure 5.4 is typical for the total extracted current from ECR sources including the RTECR, and we will show that a significant emittance growth may occur in the transit of the focussing solenoid from such high initial divergences.

5.2 Beam Transit of the Solenoid Magnet

As mentioned earlier, the RTECR beamline had been designed under the assumption of a nominal beam emittance (5 x 40 mm mrad), without taking the space charge force into consideration. But the space charge force is not negligible, at least before the analysis magnet, because we have found indirectly that the level of neutralization may

BEAM_3D Cal. He^{1+} , $V_{\text{ex}}=10$ kV, SCL Currents



$\phi = 8$ mm, $T_{t0} = 0$, $D = 5$ cm, $Z = 41$ cm

Figure 5.4. A comparison of the divergence versus beam intensity for space charge limited extraction using the BEAM_3D code. Even though a parallel beam profile at the first gap is ensured, the effect of space charge, which increases the divergence, is clearly seen.

be quite low, less than ten percent approximately, because BEAM_3D calculations without any neutralization agree quite well with measurements. Thus this space charge force increases the maximum beam divergence well beyond the nominal design beam divergence at the entrance of both the solenoid and the analysis magnets, resulting in an emittance growth due to the lens aberrations. The observed low transmission from FC#1 to FC#2, and the high divergence after analysis, are a consequence of this space charge force. The main point is -- since the divergence grows with drift distance due to this space charge force, the beam transport magnets are not in the right locations to correctly image the beam, that is, space charge alters the beam transport system.

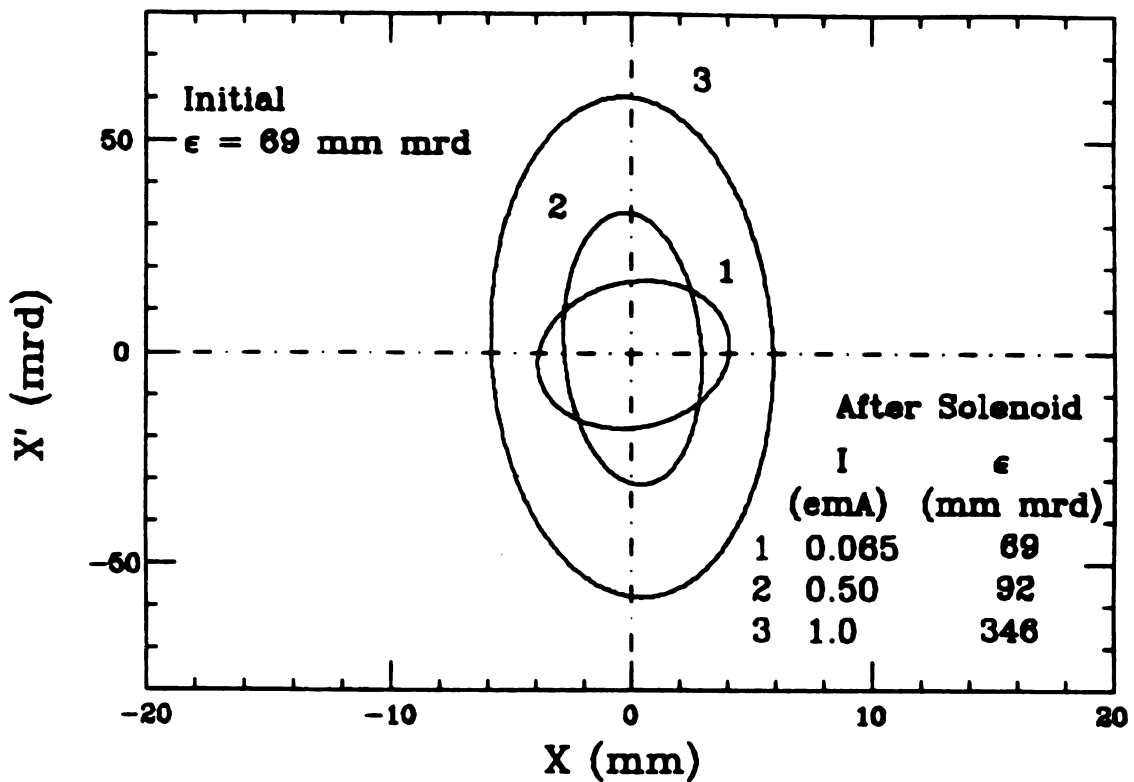
A beam crossing the solenoid with a large envelope will undergo an effective emittance growth due to the spherical aberration. This can occur for high intensity ECRIS beams because of low neutralization. Figure 5.5 shows emittances predicted by BEAM_3D, after crossing the solenoid for .065, 0.5 and 1.0 emA He¹⁺ extracted from the RTECR. In these calculations T_{10} is set to be zero, so the initial emittances of 69 mm mrad are determined by the other source conditions. In all three cases the puller voltage is chosen to achieve a space charge limited extraction in the first gap, and zero space charge neutralization is assumed. The emittances after crossing the solenoid, plotted at the position of FC#1, are seen to significantly increase with intensity. This is simply due to the increase in the beam envelope due to space charge (as shown in Figure 5.3) before the entrance of the solenoid.

The effective emittance growth due to the solenoid aberration, originating from a large beam envelope in the solenoid due to the space charge force, will also increase the beam envelope after the solenoid. BEAM_3D predicts that for a 65 μA He^{1+} extracted at 10 kV at the space charge limit, the solenoid should be excited with 81 A to focus the helium beam with a waist at the object of the analysis magnet (FC#1), and will have a beam envelope of 1.6" at the divergence box, and is experimentally seen as shown in Figure 5.6A. Figure 5.6B shows that a 550 μA He^{1+} beam, also extracted at 10 kV at the space charge limit, has doubled the beam size at the divergence box due to space charge agreeing fairly well with a BEAM_3D calculated width of 3".

The corresponding measured emittance at the divergence box for the 65 μA case is shown in Figure 5.7. As can be seen, the measured emittance of 69 mm mrad agrees with the calculated starting emittance. In the calculation, with $T_{10} = 0$, the emittance is determined by the magnetic field. Good agreement with measurement does suggest that the initial emittance of this 65 μA case is dominated by the magnetic field.

BEAM_3D predicts that if an extracted beam is far below the space charge limit in the extraction gap (voltage much greater than space charge limit voltage), the situation is much worse. It will result in very high divergence and large beam profile after extraction due to the excessive focussing strength in the extraction gap. Again such beam will have a very large beam profile at the divergence box due to severe solenoid aberrations and measurements support BEAM_3D's predictions. Shown in Figure 5.8 is a Kapton foil burn for a 65 μA

BEAM_3D Cal. He^{1+} , $V_{\text{ex}}=10$ kV, SCL Currents



$$\phi = 8 \text{ mm}, T_{t0} = 0, D = 3.3 \text{ cm}, Z = 190 \text{ cm}$$

Figure 5.5. The effective emittance of He^{1+} after crossing the focussing solenoid for various beam intensities. In each case the extraction is space charge limited, the beam energy is of 10 keV, and the emittance after extraction is 69 mm mrad. The 1.0 eA case shows very large emittance growth due to its large beam profile in the solenoid, thus the aberrations have become very severe.

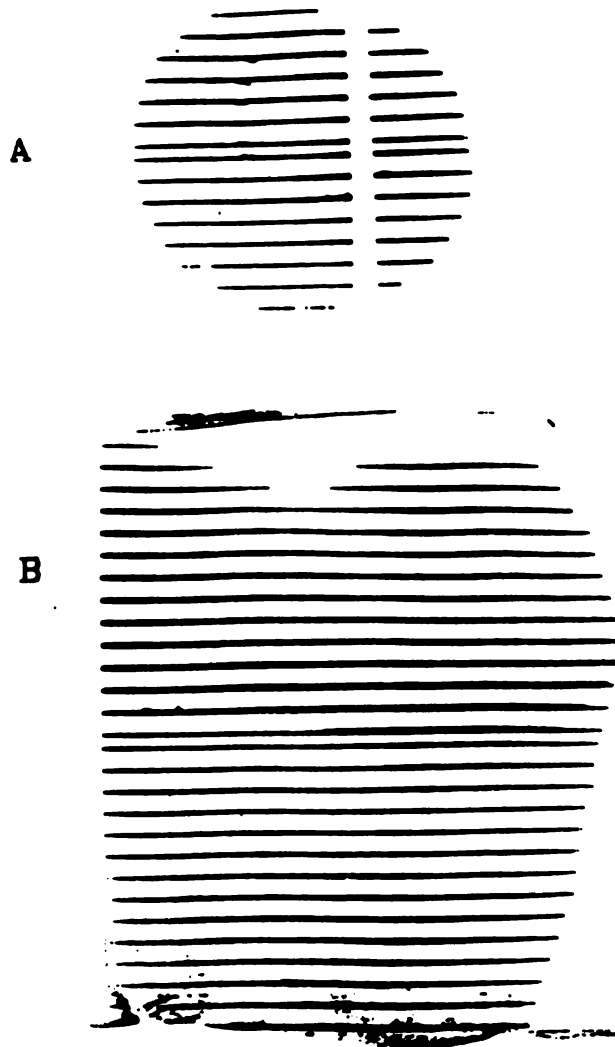
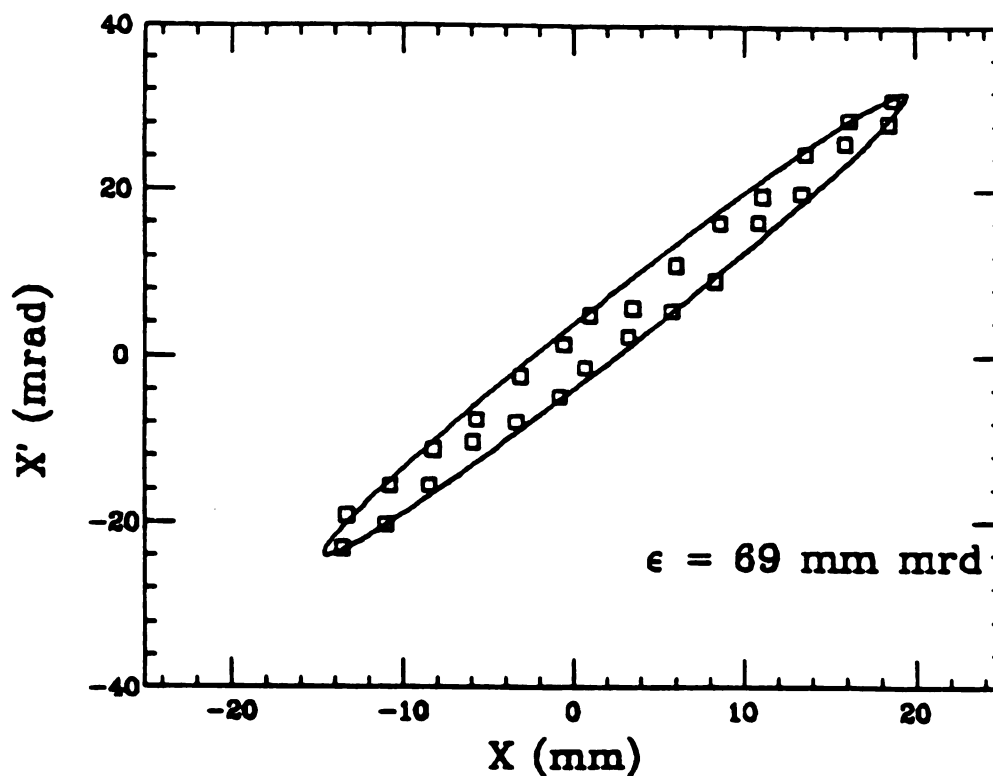


Figure 5.6. A and B are Kapton foil burns at the divergence box with He^{1+} beams of 65 and 550 μA respectively. The beam passes through a defining slit plate 8 cm upstream of the foil, giving horizontal marks on the foil. BEAM_3D predicts for 65 μA He^{1+} with space charge limited extraction ($V_{\text{ex}} = 10$ kV, $V_p = 8.5$ kV), beam profile at the divergence box will be 1.6" and that is experimentally seen. A 550 μA He^{1+} extracted at space charge limit fills the Kapton foil at the divergence box, also agreeing fairly well with a BEAM_3D calculated profile of 3".

He^{1+} , 65 e μ A at FC#1, Obj. 10 mm, L=7.87 cm



$V_{\text{ex}} = 10 \text{ kV}$, $V_{\text{p}} = 8.5 \text{ kV}$, $I_{\text{sol}} = 82 \text{ A}$

Figure 5.7. The measured emittance for the 65 e μ A He^{1+} beam in Figure 5.6A is $\epsilon = 69 \text{ mm mrad}$, which agrees very well with the BEAM_3D calculation (see Figure 5.5), in which the ion thermal energy was taken to be zero.

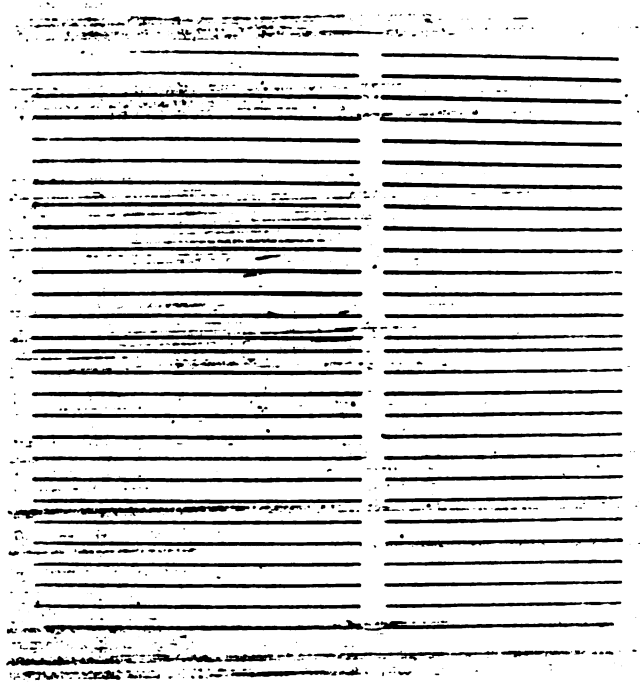
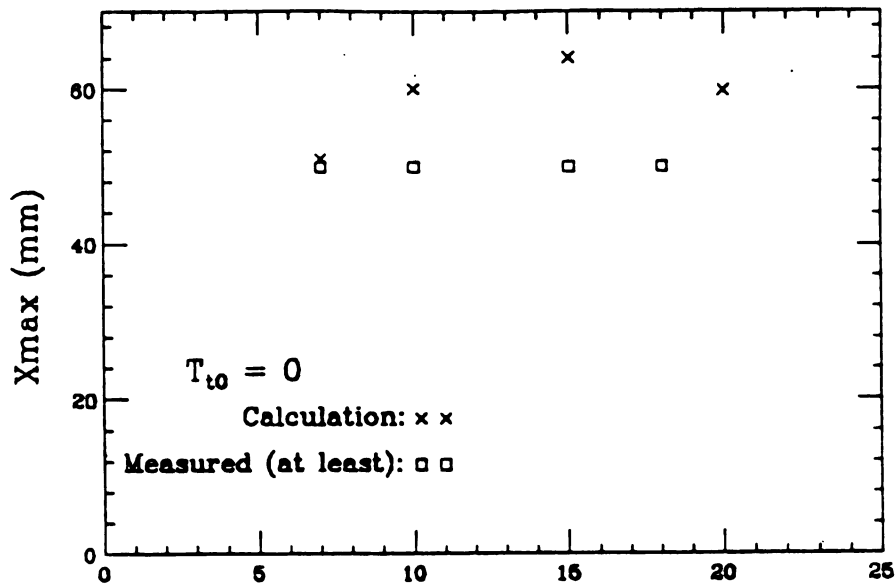


Figure 5.8. A 65 μA He^{1+} beam extracted ($V_{\text{ex}} = 10$ kV, $V_{\text{p}} = 0$) well below the space charge limited ($V_{\text{ex}} = 10$ kV, $V_{\text{p}} = 8.5$ kV) current results in high divergence and large beam profile. For this case, BEAM_3D predicts a diameter of 5.5" at the divergence box.

BEAM_3D Cal. He^{1+} , 200 e μ A. Z = 2565 mm



BEAM_3D Cal. He^{1+} , 200 e μ A. Z = 2565 mm

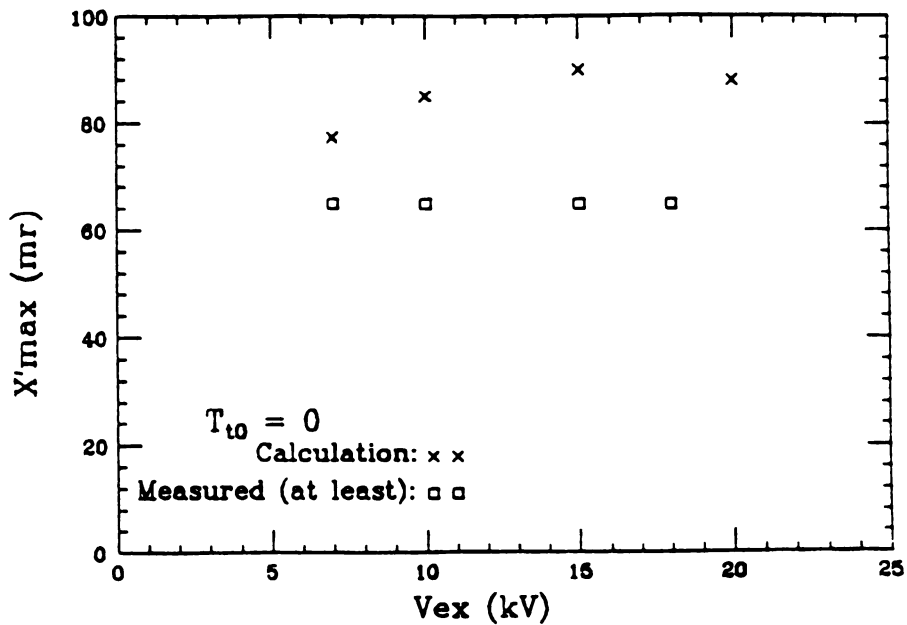


Figure 5.9. BEAM_3D predicts that a 200 e μ A He^{1+} extracted at 7, 10, 15 and 20 kV with an extraction gap of 3.3 cm will have very high divergence and large beam profile at the divergence box, because the extraction is far below the space charge limit. Measurements, limited by the measuring apparatus to a maximum divergence 65 mrad, show that the actual divergence is higher, in fair agreement with the calculations.

He¹⁺ beam extracted well below the space charge limited current. As can be seen, this 65 eμA He¹⁺ beam profile fills the whole measuring frame, and as BEAM_3D predicts, has a diameter larger than the 550 eμA space charge limited case. Figure 5.9 shows the BEAM_3D predictions and measurements (the measurements are limited by the apparatus) of the maximum divergences and beam profiles for a 200 eμA He¹⁺ beam extracted at 7, 10, 15 and 18 kV with a gap of 3.3 cm. All of these extraction conditions were well below the space charge limit extraction, and result in high divergence in the beamline due to over focussing in the first gap.

5.3 Transit of the Analysis Magnet

Because of the unneutralized space charge force, the divergence at the entrance of the analysis magnet can be significantly higher than that assumed in the beam transport design calculations. The transit of the analysis magnet may then result in substantial beam aberrations. We have graphic evidence of this effect for the other operating ECRIS at NSCL, the CPECR [An86b]. The analysis system for the CPECR differs from that for the RTECR, in that there is no focussing magnet -- the source extraction electrode is placed directly at the object of the 90° magnet (FC#1 in the RTECR system). During the first year of operation of the CPECR, primarily lithium beams were produced for injection into the k500 cyclotron. For lithium production the source is operated at high pressure on helium support gas with lithium vapor coming from an oven. The total extracted current is about 1 emA with about 50% helium 1+. After about 1 year of operation in this manner the source was moved to a different

beamline, and the image Faraday cup assembly (equivalent to FC#2 in Figure 1.2) happened to be removed as a part of this operation. We found a large triangular beam mark on the face of the 4 jaw collimator mounted just before this Faraday cup, as shown in Figure 5.10.

The bulk of our object side foil burns on the RTECR do not show triangular beams, for example as those shown in Figures 5.6 and 5.8, so this mark on the CPECR FC#2 assembly is more likely related to the transit of the analysis magnet than to beam effects at the source. Beam transport calculations at the design emittance (5×40 mm mrad) for this dipole design do not show evidence for triangular beams after transit of the analysis magnet [No87]. In addition, extensive magnet studies do not show magnetic field errors that might result in triangular beams [No89]. If however we consider the transit of the analysis magnet with an unneutralized 1.0 emA beam having the design starting emittance at the object point, we are able to generate the triangular beam marks observed. Figure 5.11 shows an intensity contour plot and transverse coordinate beam profiles at the image of our dipole magnet with a 1.0 emA He^+ beam having a starting emittance of 200 mm mrad. The intensity is uniformly distributed across the initial beam profile. This calculation was made with the GIOS beam transport code [Wo87]. The calculated profile has the same shape as the observed slit plate mark in Figure 5.10, and would be due to the second order aberrations that result from excessive divergence at the magnet entrance. The excessive divergence is due to the space charge growth. Furthermore, the y-profile in this calculation is strikingly like the scanner profile for an Ar^{10+} beam made after the RTECR analysis magnet that was shown in Figure 3.8.

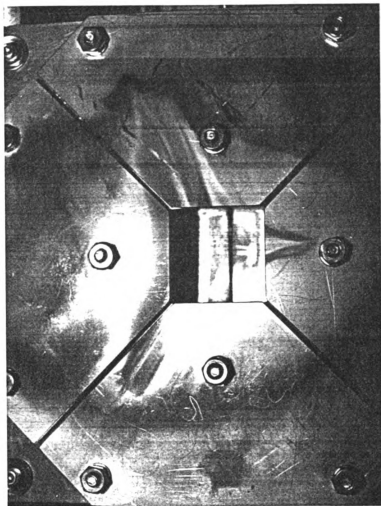
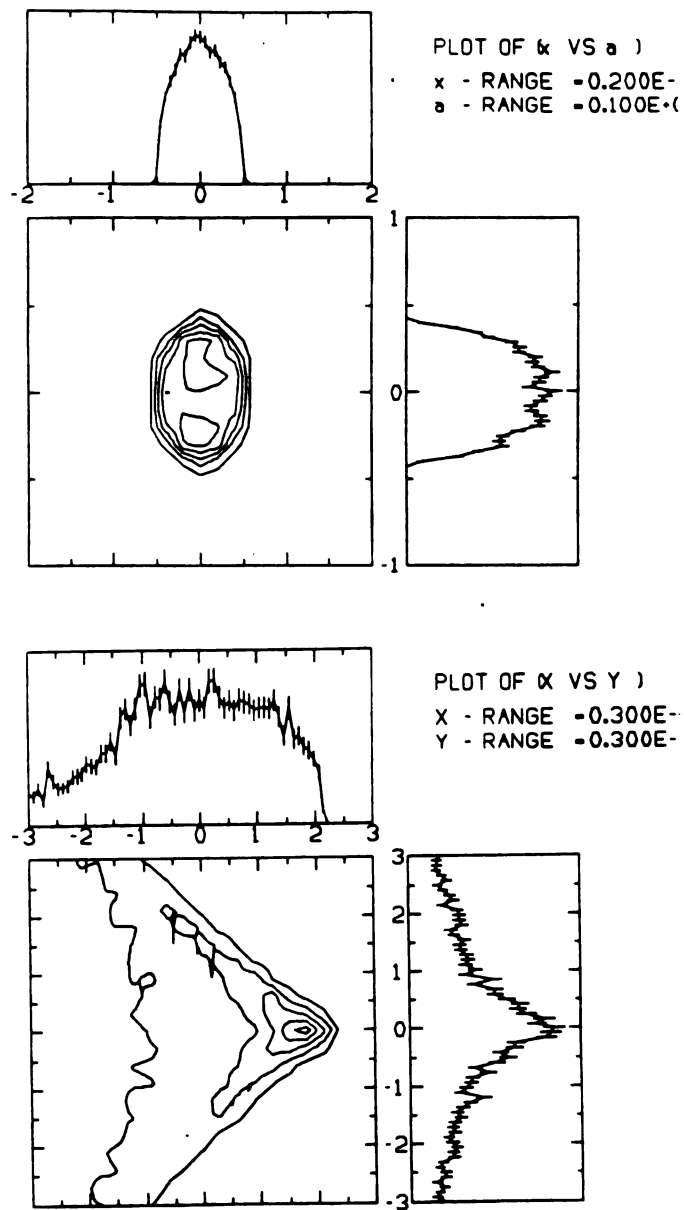


Figure 5.10. A triangular beam mark is seen on the face of the collimator of FC#2 assembly for the CPECR. The cause of this triangle shape is believed to be the space charge effect on the beam divergence before the magnet entrance, resulting in filling the magnet aperture and causing 2nd order aberrations.



90 DEGREE MAGNET ;

Figure 5.11. A GIOS beam transport calculation for the case in Figure 5.10. The transit of the analysis magnet with an unneutralized 1.0 emA helium 1+ beam of starting emittance 200 mm mrad will result in a triangular shaped beam after analysis.

5.4 Matching the 90° Analysis Dipole under the Effect of Space Charge

As mentioned above, the space charge force alters the effect of the beam transport system. So even if the beam is extracted at the space charge limit and properly focussed by the solenoid, with little emittance growth crossing the solenoid, the space charge force still can increase the beam divergence and beam envelope beyond the analysis magnet design limit, and a poor transmission of the analysis magnet will result. The lens will treat the beam, regardless of the prior history of the beam, if it has the right divergence and beam profile at the dipole entrance, as if it comes from the design object location, and image the beam at the design image point. If the space force is zero after the dipole entrance, it will not affect the beam imaging process. If the space charge force after the dipole entrance is not negligible, then this force will still affect the beam transport after the transit of the dipole, and the beam may not be imaged at desired location with the right size. In addition, an emittance growth may occur in the dipole transit because of aberrations.

Based on the above arguments, one may improve the transmission of the 90° dipole by deceiving the magnet. The deception is to move the beam waist closer to the magnet entrance than in the design, as schematically illustrated in Figure 5.12. Because of the shorter drift distance to the dipole when the waist is moved closer, the increase in the beam divergence and the beam envelope due to the effect of space charge will be less than if the beam waist was at the design object. If this results in beam characteristics that are closer to matching the design optics at the dipole entrance, then the

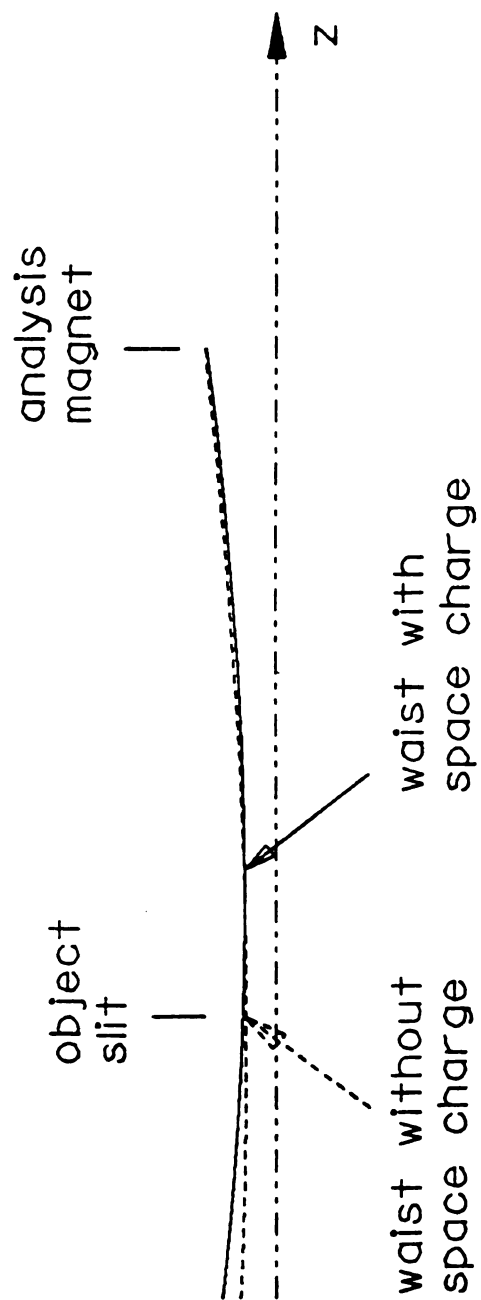


Figure 5.12. A schematic illustration of better matching of the 90° dipole for beams with space charge compared to the case of no space charge.

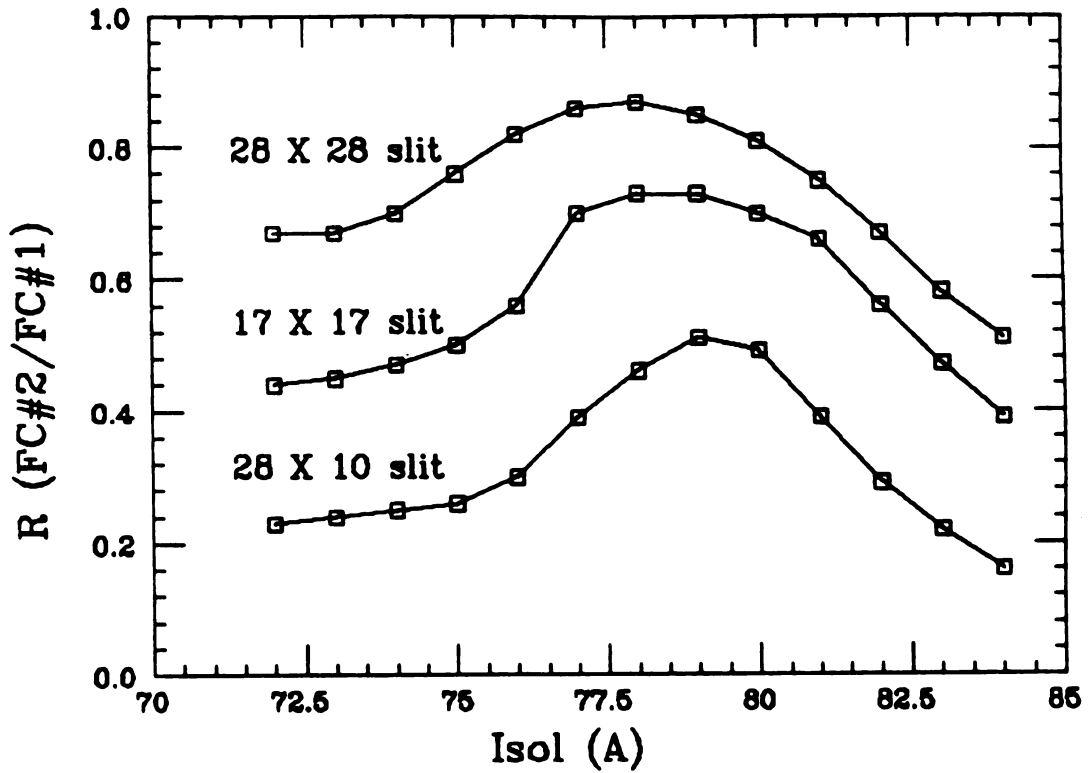
ions will be imaged closer to the design image location. We tried this technique, it works, and further confirms the transport limiting effects of space charge on the drifting beam. As shown in Figure 5.13, a 330 eμA He¹⁺ was extracted from the RTECR at the space charge limit, has a waist at the dipole magnet object when the focussing solenoid was excited with 81 Amps, and the maximum transmission for this setting is about 74%. If the solenoid excitation decreases to 78 Amps, the beam waist moves about 10 cm closer to the magnet entrance, a maximum transmission of about 87% is obtained. BEAM_3D calculations show that the solenoid spherical aberration is minimum for this beam after the transit of the focussing solenoid either for the solenoid excitation of 81 or 78 Amps, but the second case (78 Amps) gives a beam with much closer divergence and beam profile to the optics design, as shown in Table 5.1. Therefore at 81 Amps, the beam is both bigger and has higher divergence -- both are bad, and the transmission decreases as a result. Thus the dipole magnet matching with a closer beam waist is simply due to the beam space charge.

Table 5.1

Beam envelope at the 90° dipole entrance			
	Design at	BEAM_3D (He ¹⁺ 330 eμA)	
	90° entrance	Solenoid: 78 (A)	81 (A)
X _{max} (mm)	40	37	44
X' _{max} (mrad)	40	43	52

Note: A beam of 5 x 40 mm mrad is assumed at the object in the optics design. The drift distance is 1 meter to the 90° entrance.

He^{1+} , 330 e μA (FC#1), $V_{\text{ex}} = 10 \text{ kV}$, $V_p = 2.6 \text{ kV}$



$\phi_{\text{ex}} = 8 \text{ mm}$, $\phi_{\text{pul}} = 12 \text{ mm}$, $D = 5 \text{ cm}$

Figure 5.13. A 330 e μA He^{1+} is extracted with space charge limit and transported through the 90° dipole, this beam has a waist at the dipole object when the focussing solenoid is excited with 81 A. However the optimized transmission occurs at $I(\text{sole}) = 78 \text{ A}$, for which the beam waist is about 10 cm closer to the dipole.

Chapter 6

Summary and Conclusions

6.1 Extrapolation to Multiply-Charged Ion Beams

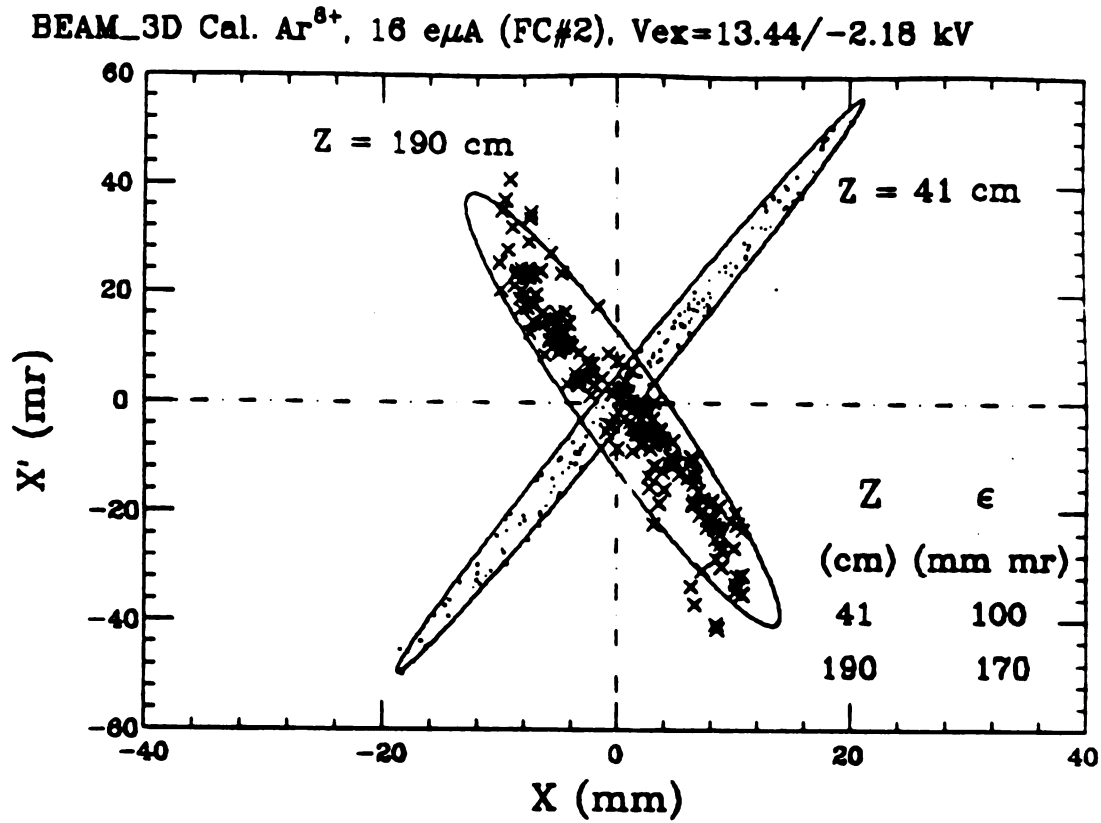
The original motivation for the development of BEAM_3D, and the beam measurements on the RTECR, was to study the emittance and beam transport matching of multiply-charged ions. This has led to the He^{1+} technique, simplifying both the calculations and the experimental studies. We have found indirect evidence for low neutralization of the initial beams, with several important consequences. It is necessary for the extraction to be space charge limited in the first gap, leading to the use of a complete spherical Pierce lens system, to minimize the initial divergence for any total extracted current. The space charge force is proportional to the square root of M/Q , which means the space charge force from 100 μA Ar^{1+} is equivalent to 316 μA He^{1+} at the same extraction voltage. Thus for heavier ion beam transport, the space charge force before the analysis, if not neutralized, will become much stronger than for a helium ion beam at the same extraction voltage and with about the same total extracted current. Although the space charge force does not increase the beam phase area, there may be lens aberrations due to substantially larger than design divergence at the magnet entrances. The high divergence tails and triangular shapes of ECRIS beams after transit of the analysis magnet are likely due to this effect.

The RTECR tunes for multiply-charged ions require much higher microwave power than for the He^{1+} beams, and gas mixing, and we have

measured thermal energies of about $6.5 \text{ eV} \times q$ for higher charged argon ions [An88]. As a consequence the starting conditions are likely to be some what different for multiply-charged ions than for the He^{1+} studies reported here. Preliminary BEAM_3D calculations for an Ar^{8+} beam extracted from the RTECR have been made, using $T_{\perp 0} \leq 5 \text{ eV} \times q$, and an actual charge state distribution of intensities among argon ions and oxygen support gas ions. These calculations showed that the Ar^{8+} ions are sensitive to the full unneutralized beam current before the solenoid entrance. A spherical aberration occurs in the solenoid crossing, increasing the emittance about a factor of two, as shown in Figure 6.1. The solenoid does some pre-analysis, but the lost ions are mostly of higher charge than $8+$ and do not constitute a significant percentage of the total extracted current. Therefore for such Ar^{8+} beams, we have then essentially the same problem as for the He^{1+} beams -- the divergence growth before lenses would be expected to be a critical limiting phenomenon. We have already seen in Figure 3.7 that high divergence tails are observed on highly charge argon ions measured after the analysis magnet, and there is an expectation that this will prove to be due to aberrations as a consequence of high divergence at the analysis magnet entrance, when further measurements are made.

6.2 Summary and Conclusions

In this thesis, some aspects of the RTECR ion beams have been studied both theoretically and experimentally. The new 3 dimensional code BEAM_3D, with a straightforward space charge model for beams of multiple ion species, has proved to be a successful analysis tool at



$\phi=8/12$ mm, $T_{i0}<5$ qeV, $D=5$ cm, $I(\text{sol})=94.3$ A

Figure 6.1. BEAM_3D code predicts that after crossing the focussing solenoid the effective emittance of Ar^{8+} (S shaped, due to the solenoid spherical aberrations) is doubled compared to its effective emittance before the solenoid. The CSD and focussing solenoid excitation are based on actual operating values.

least for the helium beams. A better extraction geometry to ensure a parallel beam with minimum divergence at the extraction gap has been introduced. The aberration of the focussing magnet lens due to a large beam envelope has been demonstrated, and subsequently a better transmission through the analysis magnet resulted from the realization that the space charge force was driving the focussing lens aberration.

The good agreement between BEAM_3D calculations and equivalent measurements suggests additionally that the plasma boundary and starting thermal energies do not play a significant role in determining the emittances when the source is tuned for these He^{1+} beams.

Based on the studies presented above, it seems not too unreasonable that an emittance upper limit of 200 mm mrad is achievable, if no aberration occurs during source extraction, for an aperture of 8 mm, an extraction voltage of 10 kV, and a magnetic field of 0.25 T, since there is no evidence that the ion temperature is higher than $10 \text{ eV} \times q$. For cool ion beams, the transverse emittance is simply dominated by the magnetic field which converts a small amount of momentum into the angular direction. While if the ions are warm, at a few eV per charge state, both the ion temperature and magnetic field are comparable in contributing to the beam emittance.

Space charge neutralization is very low in the RTECR beam line and therefore the space charge dominates the pre-analysis beam transport. The RTECR beamline is capable of transmitting a beam of $5 \times 40 \text{ mm mrad}$ emittance, but space charge alters the beam transport by increasing the beam divergence, so the main task is to compensate the space charge force to avoid lens aberrations.

Shortening the beam drift distance is one of the means to compensate for this space charge effect. Since the beam envelope is quadratically proportional to the drift distance, reducing half of the drift distance can reduce a factor of 4 of the beam envelope, and the aberration will become very small. Other alternatives would be to (1). generate a parallel electron beam within the ion beam to fully neutralize the space charge [Kr87], and one could then return to the designed beam transport system based on zero intensity transport calculations, or (2). assume a maximum space charge in the design of the beamline, and weaker beams would be properly transported by retuning the beamline.

All of these techniques can be subjects for future study on ECRIS ion beam characteristics to fully understand this young technology for future development of ECRIS.

Appendix

Introduction to ECRIS

An ECRIS is a confined plasma device from which it is possible to extract useful beams of highly-charged ions. Microwaves are launched into the plasma, resonantly accelerating confined electrons. These hot electrons ionize atoms in a process loosely described as electron impact ionization. Ions lost from the magnetic confinement zone fall into the extraction zone where beams are formed. The key components of this kind of positive ion source and the main operation characteristics will now be briefly discussed.

A.1 'Unit' ECR Cell

All ECRIS have at least one unit ECR cell, which will now be defined. A unit ECR cell consists of a vacuum vessel, a minimum-B magnetic bottle [Ni83], a microwave generator and an extraction system, as illustrated schematically in Figure A.1. The vacuum vessel is maintained at low pressure ($\sim 10^{-6}$ to 10^{-7} T), and serves as a microwave resonance cavity. The minimum-B field provides the plasma confinement and nested closed magnetic surfaces for resonant electron heating. This minimum-B field is formed by superposition of a pair of solenoid coils and a multipole magnet. The solenoid coils (room temperature or superconducting coils) produce a tandem magnetic mirror field, as shown for the NSCL CPECR [An86b] in Figure A.2. Tandem mirrors would provide the well known axial confinement for a collisionless plasma, but do not contribute to good radial confinement

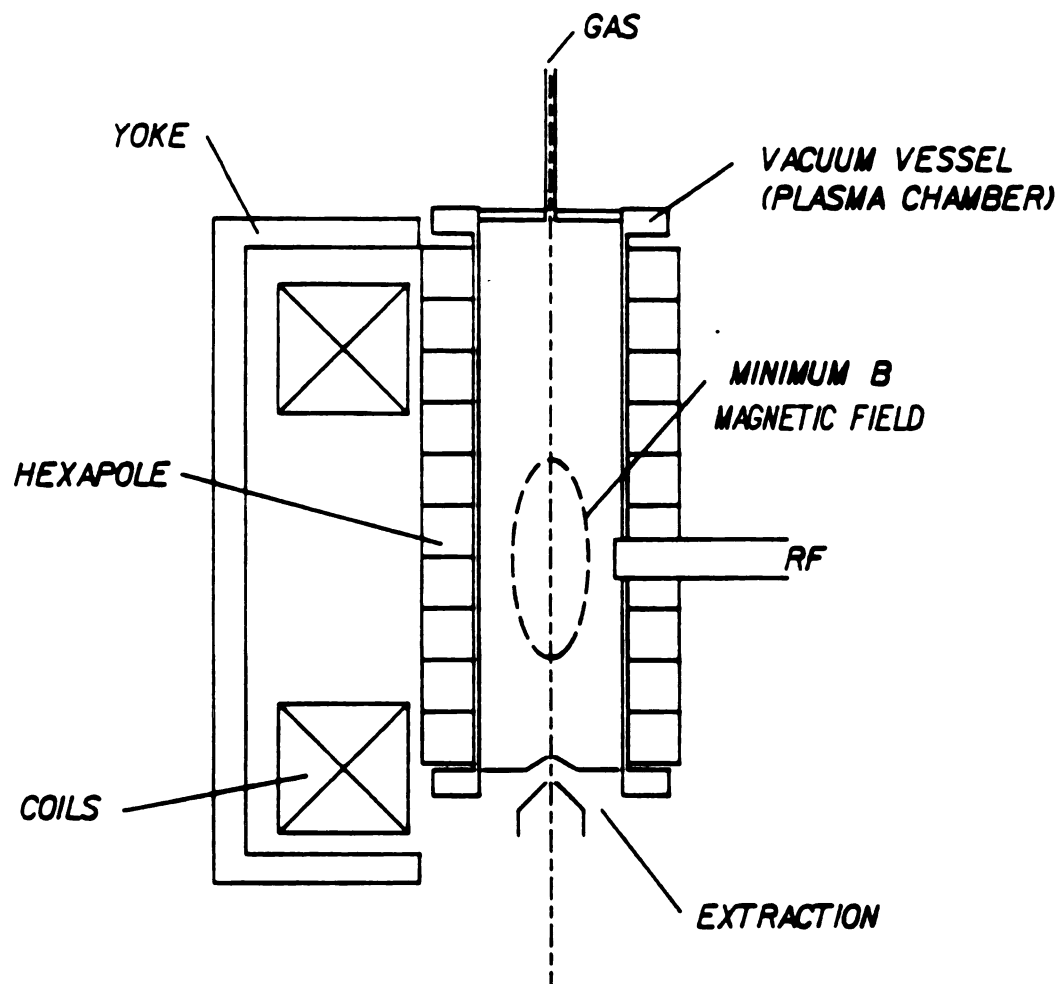


Figure A.1. A 'Unit' ECR Cell consists of a vacuum vessel, microwave generator, a minimum-B field and an extraction system.

CP--ECR AXIAL FIELD PROFILE

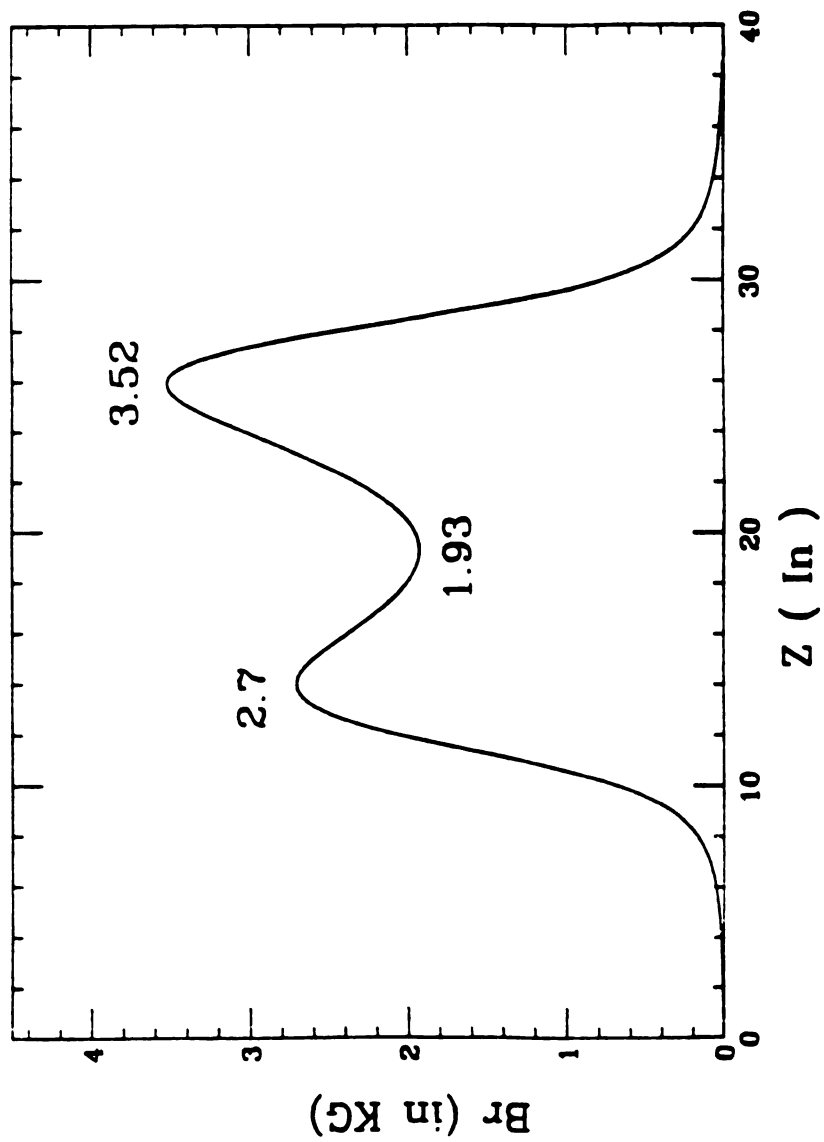


Figure A.2. A typical axial magnetic field profile produced by a set of solenoid coils for a single stage ECRIS.

due to ion - ion collisions and bad field curvature in between the mirror coils. The addition of a multipole magnet, which produces a magnetic field that increases with radius (quadrupole or higher multipole), provides improved radial confinement. For historical reasons, most ECRIS have used a hexapole magnet for this purpose. In ECRIS, most hexapole magnets are made of Rare Earth Cobalt permanent magnets (for example, SmCo_5 or $\text{Sm}_2\text{Co}_{17}$) because equivalent strength coils would have very high power consumption, we choose permanent magnets at the price of a loss of field adjustability. As can be seen in Figure A.3, the field strength of a typical ECRIS hexapole magnet varies approximately with the square of the radius over most of the magnet bore [An83]. The superposition of a tandem mirror (solenoid field) with a hexapole field is then one way to produce a minimum-B field. In such a superposition, the magnetic field will increase in all directions away from the center. It has been established experimentally that a minimum-B field provides better plasma confinement compared to the case of only a tandem mirror field [Io62], the resulting minimum-B field topology produce by a set of mirror solenoid coils and a hexapole magnet is schematically shown in Figure A.4 [An87b].

The longer ion and electron confinement times in a minimum-B field has significant consequences for high charge state ion production. First, the step-by-step ionization dominates the ionization process [Ge85], so the longer the ions stay in the plasma, the more probable higher charge states become. Second, electrons will have higher energy in the plasma if their confinement time increases.

6 Pole 6 Ps, Brm=8.7 KG, R=2.375 (Z=0)

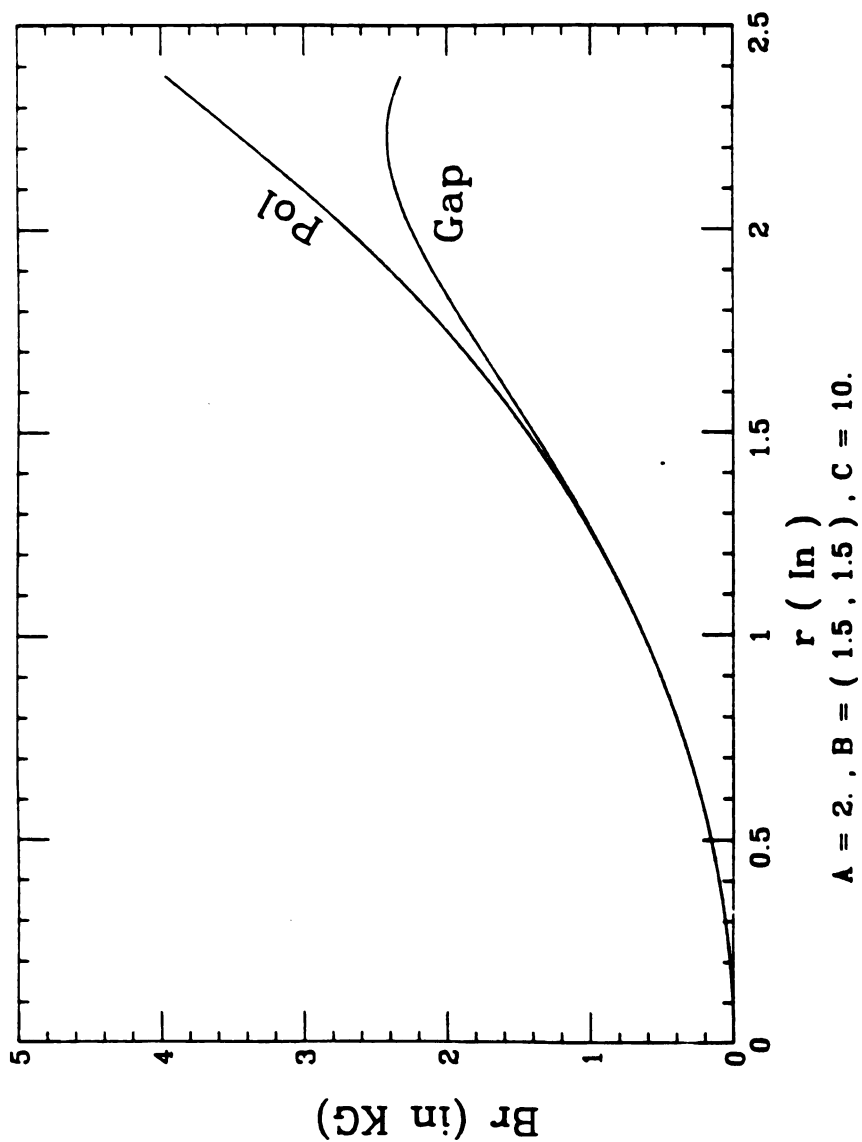


Figure A.3. This figure shows the strength of a hexapole as a function of radius along one of the poles and in a gap.

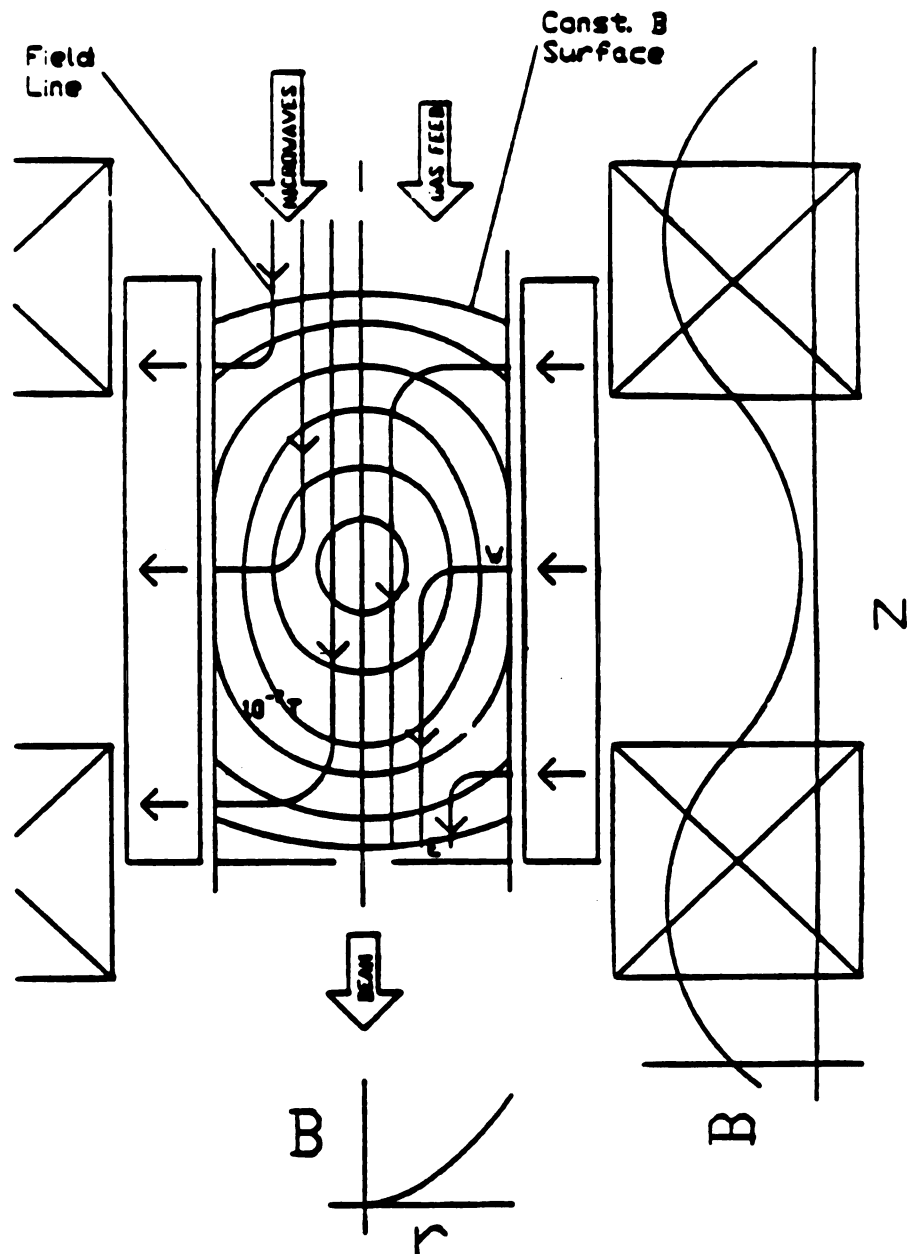


Figure A.4. A "minimum-B field" topology as a result of the superposition of a hexapole and a set of solenoid fields.

Charged particles moving at a magnetic field will experience a Lorentz force

$$\vec{F} = Q \vec{v} \times \vec{B} \quad (\text{A.1})$$

where Q is the charge that the particle carries, \vec{v} is the particle velocity and \vec{B} is the local magnetic field. For historical reasons, we call the frequency of such particle rotation the "cyclotron frequency", which is related to the local magnetic strength B , the charge Q and the mass M of the charged particle by the following expression

$$\omega = \frac{QB}{M} \quad (\text{A.2})$$

If the charged particle is an electron, the above cyclotron frequency is called the "electron cyclotron frequency".

$$\omega_{ec} = \frac{eB}{m_e} \quad (\text{A.3})$$

where e and m_e are the charge and mass of the electron respectively. When a plane wave of frequency ω is launched into a plasma having electrons confined by a magnetic field, acceleration is possible where $\omega \approx \omega_{ec}$. Energy can then be transferred into the electrons from the incoming electromagnetic wave. This energy transfer process is called "Electron Cyclotron Resonance Heating". As a consequence of the heating, the energetic electrons then can bombard the atoms and ions

to a certain degree of ionization. In ECRIS the electron energy gained by ECRH heating can be up to hundreds keV, but the peak of the distribution is at tens of keV [Be84], which improves the probability for ionizing a variety of atoms and ions as can be seen from the ionization potentials, taken from Carlson et al [Ca70], of various atoms and ions shown in Figure A.5.

Some ECRIS make use of two ECR cells, for example, the RTECR is a two stage room temperature ECRIS [An86a]. In two stage ECRIS, the first stage produces a predominantly 1+ dense plasma which diffuses into the second stage (main ionization stage). The advantage of two stage operation is the coupling of two stages greatly enhances the high charge state ion production, because the main stage operating pressure is substantially reduced while maintaining a high plasma density. Comparison of one stage versus two stage operation for nitrogen ion production in the RTECR is shown in Figure A.6.

A.2 ECR Operating Characteristics

Here we briefly summarize important operating characteristics of DC mode ECRIS. The reader is referred to the literature, especially [Ge79, Jo84], for additional information on this subject.

1. ECRIS reach charge equilibrium.

In equilibrium, net charge gain in the ECRIS plasma should be zero. Thus we require that,

$$\Phi_e = \sum_{q=1} q(\Phi_q^1 + \Phi_q^2 + \dots) \quad (\text{A.4})$$

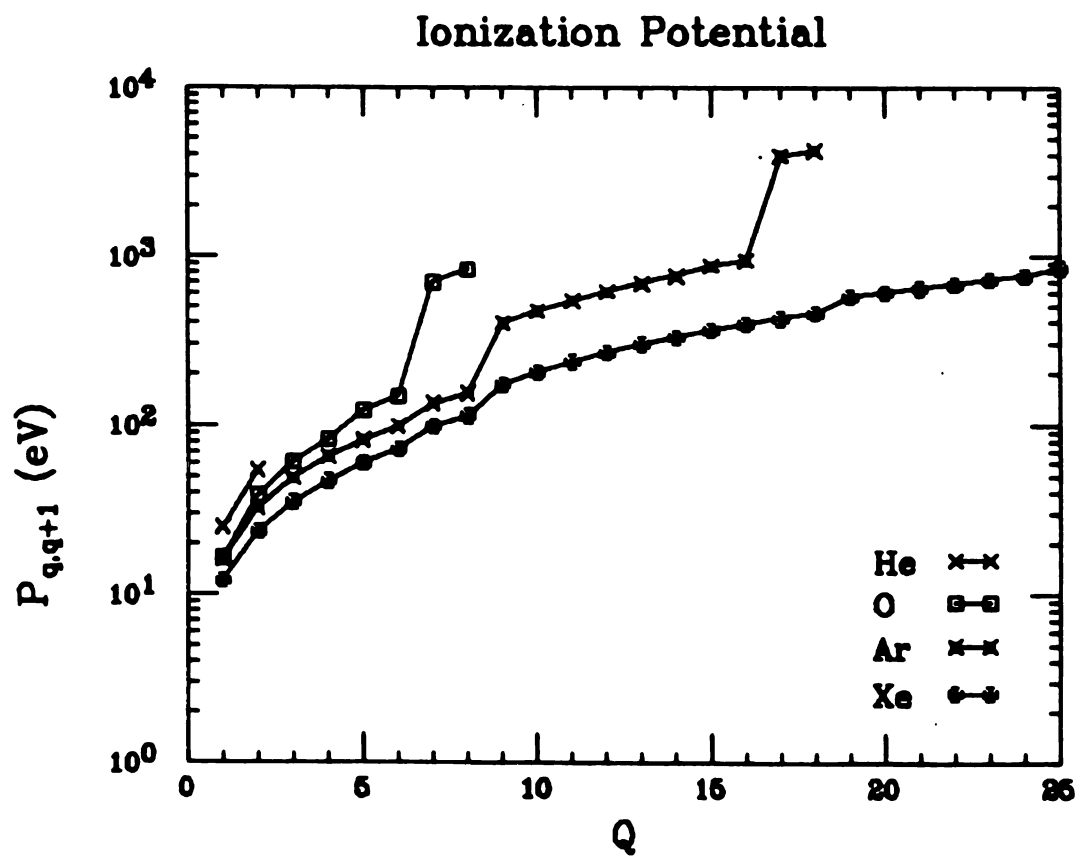


Figure A.5. Single ionization potentials of some atoms and ions.

STRONG 2 STAGE OPERATION VS. 2ND ONLY

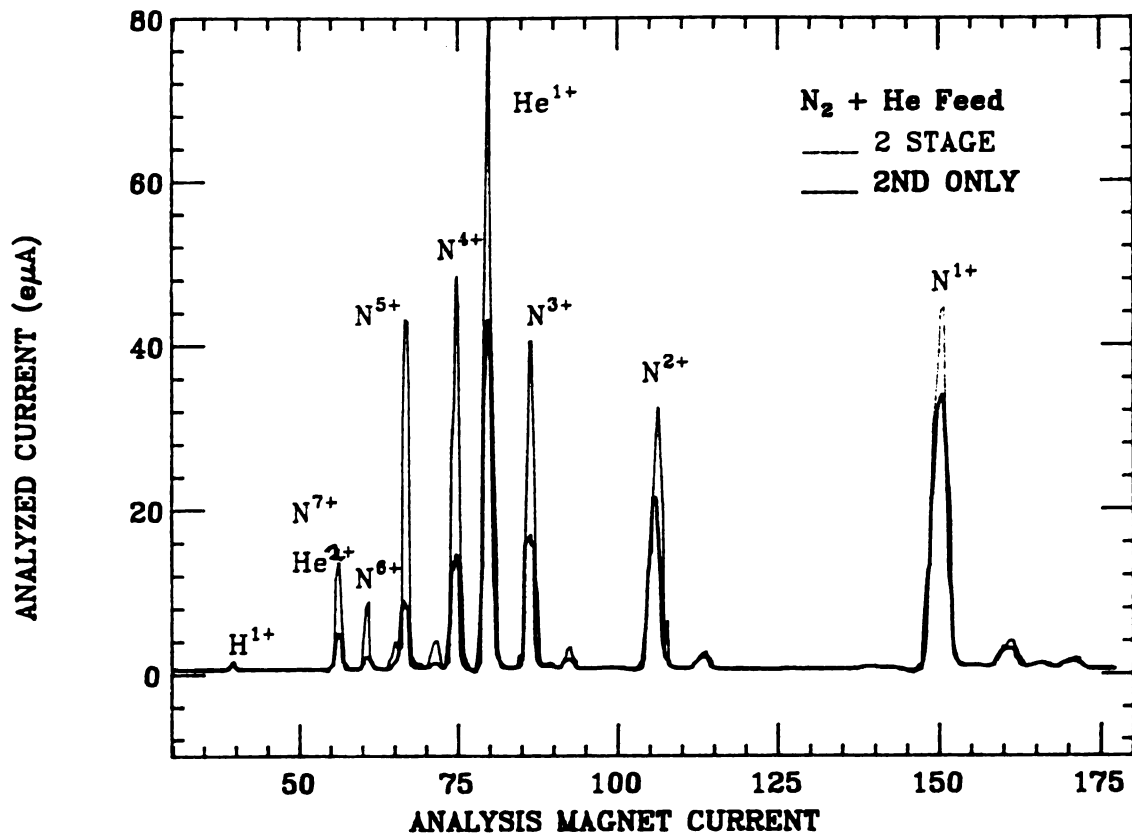


Figure A.6. Performance comparison between 2-stage and second stage only RTECR operation for the production of nitrogen ions. Helium is used as a support gas. Each next higher charge state shows a large percentage increase in current with the first stage on.

where ϕ_e is the electron flux density, ϕ_q^i stands for the flux density of ions with q electrons removed, and there may be as many as i of ions of different elements with the same charge state q in the plasma.

Since the net gain of electrons and ions in the plasma should be zero, we must also have

$$\frac{dN_e}{dt} = \frac{dN_{iq}}{dt} = 0 \quad (\text{A.5})$$

where N_e is the electron density and N_{iq} is the ion density of charge state q .

2. The probability of producing multiply-charged ions in a single electron impact collision falls off rapidly with increasing ion charge Q .

The production of highly-charged ions in ECRIS is dominated by step-by-step ionizations [Ge85]. The single step ionization rate, for an ion going from state q to $q+1$, is a function of the electron energy E and is given by

$$R_{\text{ion } q \rightarrow q+1}(E) = \sigma_{\text{ion } q \rightarrow q+1}(E) \cdot v_e(E) \cdot N_e(E) \quad (\text{A.6})$$

where $\sigma_{\text{ion } q \rightarrow q+1}$ is the electron impact single ionization cross section which falls off rapidly with increasing charge state q for a given electron temperature [Mu80], v_e is the electron velocity and N_e is the electron density. The ionizing electrons in an ECRIS are not monoenergetic, but have an energy distribution. An integration must

be performed on all possible energies to calculate the ionization rate R [Jo84]. The exact form of the electron distribution in ECRIS is not yet clearly known. For simplicity, a Maxwell distribution is generally used in order to estimate the ionization rate. Shown in Figure A.7 are calculations of ionization rate coefficients $S = \langle R_{\text{ion } q \rightarrow q+1} / N_e \rangle$ for stepwise ionization of argon atoms and ions, using electron-impact cross section due to Müller et al [Mu80], and the atomic subshell binding energies from Carlson et al [Ca70].

3. Charge exchange between ions and neutrals occurs in plasma and this is an important limiting process.

Single charge capture from neutrals dominates the charge exchange process. The cross section for single charge capture, proposed by Müller and Salzborn [Mu77], is

$$\sigma_{\text{exch } q \rightarrow q-1} = 1.43 \cdot 10^{-12} \cdot q^{1.17} \cdot P_{0+1}^{-2.76} \text{ cm}^2 \quad (\text{A.7})$$

where P , in eV, is the first ionization potential of the atom. Müller and Salzborn also give formulae $\sigma_{\text{exch } q \rightarrow q-2}$ through $\sigma_{\text{exch } q \rightarrow q-4}$. However, as q increases, the double and higher order charge exchange processes can be ignored when compared to the single charge exchange process. Typically, these single charge capture cross sections are three to four orders of magnitude larger than ionization cross sections. The corresponding rate of single charge capture between ions and neutrals is

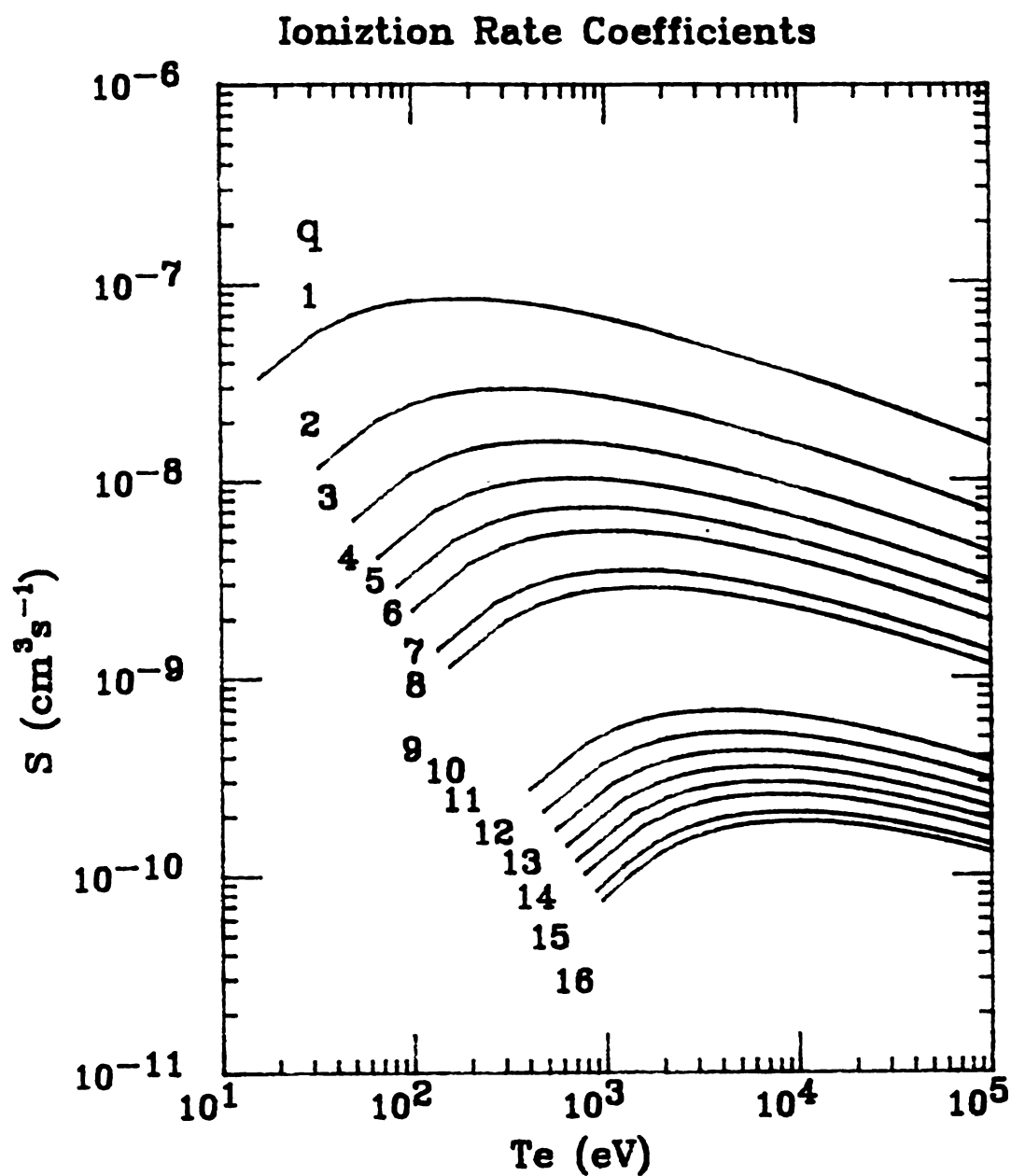


Figure A.7. Ionization rate coefficients S for single ionization of argon atoms and ions from the ground state by electron-impact in plasma (Maxwellian distribution, no collision limit).

$$R_{\text{exch } q \rightarrow q-1} = \sigma_{\text{exch } q \rightarrow q-1} \cdot v_{\text{in}} \cdot N_0 \quad (\text{A.8})$$

where v_{in} is the relative velocity between ions and neutrals and N_0 is the neutral density. The ions in ECRIS plasma are rather cold compared to the electrons, at most a few tens to a hundred eV for ions of charge state $q \leq 20$ [Ko86, Me86, An88], and the ion velocities are much slower than the electrons. Thus there is a competition between ionization and charge exchange in ECRIS plasma. Since we do not have much control over the charge exchange cross sections and the relative velocity v_{in} , the most effective way to reduce such charge exchange is to reduce the neutral density N_0 , and ECRIS generally do operate at low pressure, to ensure the best performance of the source. Typical operation pressures in the ECRIS ionization (main) stage is $10^{-6} \sim 10^{-7}$ T, for two stage ECRIS, the operation pressure in the first stage is $10^{-3} \sim 10^{-4}$ T.

4. The electron density is limited.

The maximum electron density in plasma is tied to the microwave frequency by the following relation

$$N_{\text{ec}} = 1.24 \times 10^{-8} f^2 \quad (\text{A.9})$$

which is a consequence of a limit for electromagnetic wave injection for a given plasma density. Here N_{ec} is the critical electron density and f is the microwave frequency. According to Eq. (A.6), increasing the electron density will increase the ionization rate, therefore to

improve the high charge state ion production we should raise the density, but Eq. (A.9) sets an upper limit on how high we can raise electron density in ECRIS plasma for a given microwave frequency f . Thus one wants to increase the electron density further in ECRIS, the microwave frequency and the magnetic field should be increased accordingly.

5. Low gas consumption.

The source of plasma in an ECRIS is neutral gas. The gas consumption is in the order of one standard cc/hr, due to the low operating pressure and good ionization efficiency. For example, the gas consumption of the RTECR has been measured to be ≤ 1 standard cc/hr [An87a]. A 1 standard cc/hr consumption of helium is equivalent to $\sim 7.5 \times 10^{15}$ particle/sec, while the total extraction current from the RTECR (mainly He^{1+} beam) is 0.5 emA, or 3×10^{15} particle/sec. The ionization efficiency is then $\text{IE} \approx N_1/N_0 = 40\%$. Metallic ions can be produced by the use of an oven that makes metal vapor, as shown for the NSCL CPECR in Figure A.8, or by direct feed of the material into the main stage plasma [Sa87].

6. A mixture of a lighter gas as support gas usually boosts the yields of the intermediate and high charge state ions of a heavy gas.

Figure A.9 shows a comparison of pure Argon feed to the effect of mixture of Argon with lighter gases obtained from the RTECR, and similar results were also been observed in other ECRIS [Br84, Ly84]. This effect has been observed in most ECRIS, readers are referred to the literature of ECRIS for the details. The effect of gas mixing

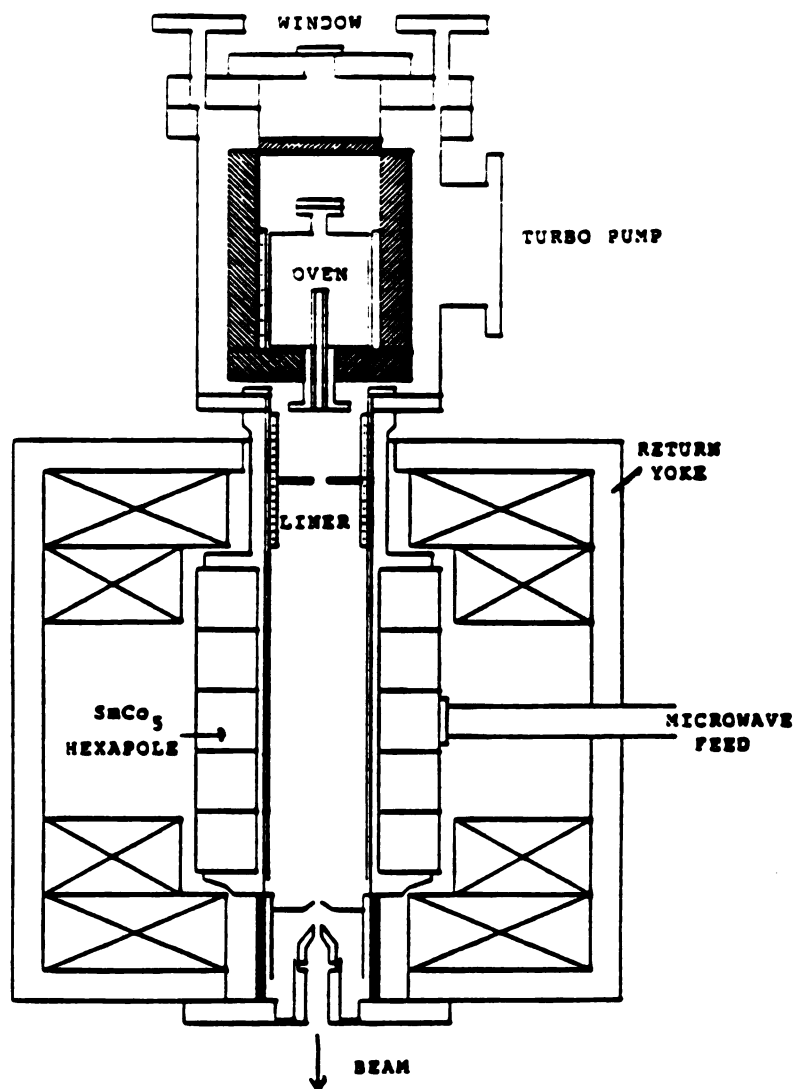


Figure A.8. A high temperature oven for producing metal vapor is equipped with the CPECR Ion Source at NSCL/MSU.

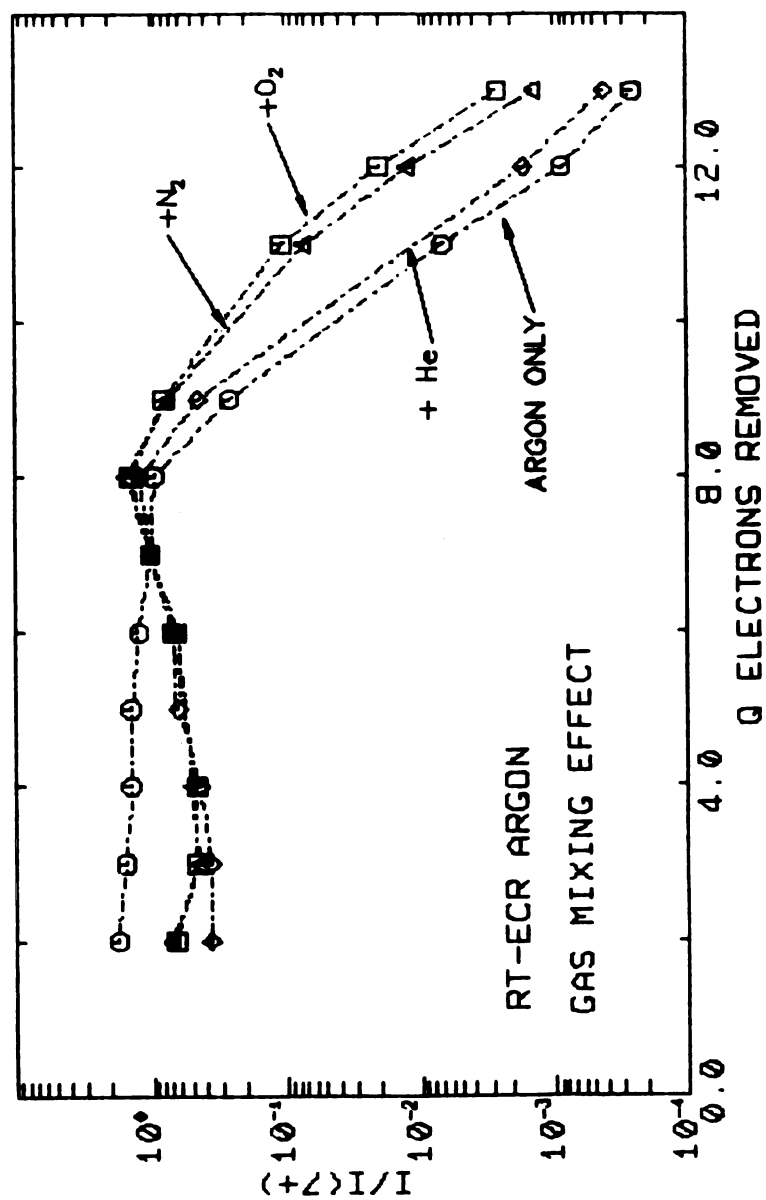


Figure A.9. The direct dependence of gas mixing effects on mass is seen in the mixing of lighter gases with argon.

could be explained by an ion cooling model proposed by Antaya --energy transfer from the heavy ion species to the light ones [An88]. Such thermalization results in longer confinement time of the heavy ion species. A preliminary energy spread measurement of argon versus argon mixed with oxygen as coolant on the RTECR, strongly supports the above explanation for the gas mixing [An88].

LIST OF REFERENCES

- An83 T.A. Antaya, J. Moskalik and D. Lawton, NSCL Annual Report 1983-84, p. 267.
- An86a T.A. Antaya, Z.Q. Xie, Proc. 7th Workshop on ECR Ion Sources, ..
Jülich, W. Germany, 1986, p. 72.
- An86b T.A. Antaya, Z.Q. Xie and D.P. Sanderson, NSCL 1986 Annual Report, p. 174.
- An87a T.A. Antaya, L. Gneiting, W. Nurnberger, D.P. Sanderson and Z.Q. Xie, Proc. of Int. Conf. on ECR Ion Sources and their Appl., East Lansing, NSCL Report #MSUCP-47, 1987, p. 86.
- An87b T.A. Antaya, H.G. Blosser, J.M. Moskalik, J.A. Nolen and A.F. Zeller, Proc. of Int. Conf. on ECR Ion Sources and their Appl., East Lansing, NSCL Report #MSUCP-47, 1987, p. 312.
- An88 T.A. Antaya, Proc. Int. Workshop on ECR Ion Sources, Grenoble, France, 1988.
- An89 T.A. Antaya, private discussion.
- Ba86 E. Baron, L. Bex and M.P. Bourgarel, Proc. 7th Workshop on ECR Ion Sources, ..
Jülich, W. Germany, May 1986, p. 25.
- Be67 M.Y. Bernard, Focusing of Charged Particles, Academic Press INC. (edited by A. Septier), New York, NY, 1967, Vol. I, p. 34.
- Be84 V. Bechtold, L. Friedrich and F. Schulz, Proc. of Tenth Int. Conf. on Cyc. and their Appl. East Lansing, 1984, p. 118.
- B172 S. Bliman, R. Geller, W. Hess, B. Jacquot, IEEE Trans. NS-19, No. 2, 1972, p. 200.

- Br67 George R. Brewer, Focusing of Charged Particles (edited by A. Septier), Academic Press Inc., 1967, p. 74.
- Br84 W. Brautigam, H. Beuscher, H.G. Mathews, J. Reich, P. Wucherer, Proc. 10th Int. Conf. on Cyclotrons, IEEE 84CH1996-3, 1984, p. 122.
- Ca70 T.A. Carlson, C.W. Nestor Jr., N. Wasserman and J.D. McDowell, Atomic Data 2, 1970, p. 63.
- Ch11 C.D. Child, Phys. Rev. 32, 1911, p. 492.
- Cl83 D.J. Clark, J.G. Kalnins and C.M. Lyneis, IEEE Trans. Nucl. Sci. NS-30, 1983, p. 2719.
- Cl87 D.J. Clark, Proc. Int. Conf. on ECR Ion Sources and their Appl., E. Lansing, Nov 1987, p. 433.
- De83 O.C. Dermois, Particle Accelerators, Vol. 14, 1983, p. 63.
- Dr83 A.G. Drentje, Physica Scripta, T3, (1983) 45.
- Dr85 A.G. Drentje, Proc. 6th Int. Workshop on ECR Ion Sources, Berkeley, 1985, p. 73.
- Ge70 R. Geller, Appl. Phys. Lett. 16, No 10, 1970, p. 401.
- Ge79 R. Geller, IEEE Trans. Nucl. Scien. NS-26, No. 2, 1979, p. 2120.
- Ge85 R. Geller et al, Proc. 6th Int. Workshop on ECR Ion Sources, Berkeley, 1985, p. 1.
- Ha87 H.L. Hagedoorn et al, Proc. of Int. Conf. on ECR Ion Sources and their Appl., East Lansing, NSCL Report #MSUCP-47, 1987, p. 389.
- He79 William B. Herrmansfelt, ELECTRON TRAJECTORY PROGRAM, 1979.
- Ho79 R.F. Holsinger, New England Nuclear, 1979.
- Io62 Yu.V. Gott, M.S. Ioffe, V.G. Telkovskii, Nucl. Fusion, 1962 Suppl., part 3, p. 1045.

- Jo83 Y. Jongen and G. Ryckewaert, IEEE Trans. Nucl. Sci. NS-30, 1983, p. 2685.
- Jo84 Y. Jongen, Proc. 10th Int. Conf. on Cyclotrons and their Appl., IEEE 84CH1996-3, 1984, p. 322.
- Kö86 H. Köhler, M. Frank, B.A. Huber and K. Wieseemann, Proc. 7th Workshop on ECR Ion Sources, Jülich, W. Germany, 1986, p. 215.
- Kr86 W. Krauss-Vogt, Proc. 7th Workshop on ECR Ion Sources, Jülich, W. Germany, 1986, p. 274.
- Kr87 G.A. Krafft, Ph.D. Thesis, Accelerator & Fusion Research Division, LBL, Univ. of Berkeley, 1987.
- Ly84 C.M. Lyneis, private communication.
- Ma83a H.-G. Mathews, H. Beuscher, W. Krauss-Vogt, Proc. Int. Ion Engineering Congress - ISIAT'83 & IPAT'83, Kyoto, Japan, 1983.
- Ma83b H.-G. Mathews, H. Beuscher, W. Krauss-Vogt, IKP Ann. Report 83, p. 125.
- Ma86a M. Mack, J. Haveman, R. Hoekstra and A.G. Drentje, Proc. 7th Workshop on ECR Ion Sources, Jülich, W. Germany, 1986, p. 152.
- Ma86b G. Mank, M. Liehr and E. Salzborn, Proc. 7th Workshop on ECR Ion Sources, Jülich, W. Germany, 1986, p. 103.
- Me86 F.W. Meyer, Proc. 7th Workshop on ECR Ion Sources, Jülich, W. Germany, (1986) 11.
- Mi58 R. L. Mills and A. M. Sessler, MURA Rept. No. 433, Midwestern Universities Research Association, Stoughton, Wisconsin, 1958.
- Mü77 A. Müller and E. Salzborn, Phys. Lett. 62A, No 6, 1977, p. 391.
- Mü80 A. Müller et al, Atom. Molec. Phys., 13, 1980, p. 1877.
- Ni83 D.R. Nicholson, Introduction to Plasma Theory, John Wiley & Sons, 1983, p. 206.

- No87 J.A. Nolen, S. Tanaka, A. Zeller and N. Bhattacharya, Proc. Int. Conf. on ECR Ion Sources, NSCL Report #MSUCP-47, E. Lansing, Nov 1987, p. 454.
- No89 J.A. Nolen, private communication.
- Pa87 R.C. Pardo and P.J. Billquist, Proc. of Int. Conf. on ECR Ion Sources and Their Appl., East Lansing, NSCL Report #MSUCP-47, 1987, p. 279.
- Pi54 J. R. Pierce, Theory and Design of Electron Beams, D. VAN NOSTRAND INC., 1954, p. 173.
- Po70 H. Postma, Phys. Lett. 31A, No. 4, Feb 1970, p. 196.
- Ro66 Michael J. Romanelli, Mathematical Methods for Digital Computers (edited by A. Ralston and H.S. Wilf), John Wiley & Sons, Inc., 1966, p. 110.
- Sa87 D.P. Sanderson, T.A. Antaya and Z.Q. Xie, Proc. of Int. Conf. on ECR Ion Sources and Their Appl., East Lansing, NSCL Report #MSUCP-47, 1987, p. 300.
- Se67 A. Septier, Focusing of Charged Particles, Academic Press INC. New York, NY, 1967, Vol. II, p. 151.
- Sp85 P. Spadtke, KOBRA3 - THREE DIMENSIONAL RAYTRACING INCLUDING SPACE-CHARGE EFFECTS, IEEE Trans. Nucl. Sci. NS32, 1985, p. 2465.
- Tu80 N.Chan Tung, S. Dousson, R. Geller, B. Jacquot and M. Lieuvain, Nucl. Instr & Meth, 174 (1980), 151.
- We82 H.I. West, Jr., Calculation of Ion Charge-State Distribution in ECR Ion Source, UCRL-53391, LLNL, 1982.
- Wo72 A. van der Woude, IEEE Trans. NS-19, No. 2, 1972, p. 187.
- Wo86 B.H. Wolf, K. Leible, P. Spadtke, N. Angert, J. Klabunde and

B. Langenbeck, Proc. 7th Workshop on ECR Ion Sources, Jülich, W. Germany, 1986, p. 103.

Wo87 H. Wollnik et al, Nucl. Instrum. and Meth. A258, 1987, p. 402.

Xi86 Z.Q. Xie and T.A. Antaya, NSCL 1986 Annual Report, p. 166.

Xi87 Z.Q. Xie and T.A. Antaya, Proc. Int. Conf. on ECR Ion sources, NSCL Report #MSUCP-47, E. Lansing, 1987, p. 420.

Ze85 A.F. Zeller, J.A. Nolen Jr. and L.H. Harwood, NSCL 1985 Annual Report, p. 165.